



January 2019

# Small-Scale Characterization Of Additively Manufactured And Heat Treated AlSi10Mg

Farwan A. Alghamdi

Follow this and additional works at: <https://commons.und.edu/theses>

---

## Recommended Citation

Alghamdi, Farwan A., "Small-Scale Characterization Of Additively Manufactured And Heat Treated AlSi10Mg" (2019). *Theses and Dissertations*. 2441.

<https://commons.und.edu/theses/2441>

This Thesis is brought to you for free and open access by the Theses, Dissertations, and Senior Projects at UND Scholarly Commons. It has been accepted for inclusion in Theses and Dissertations by an authorized administrator of UND Scholarly Commons. For more information, please contact [zeinebyousif@library.und.edu](mailto:zeinebyousif@library.und.edu).

**Small-scale Characterization of Additively Manufactured and Heat Treated  
AlSi10Mg**

by

Farwan Alghamdi  
Bachelor of Science, University of North Dakota, 2017

A Thesis  
Submitted to the Graduate Faculty

of the

University of North Dakota

in partial fulfillment of the requirements

for the degree of

Master of Science

Grand Forks, North Dakota

May  
2019

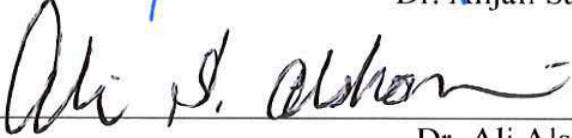


This thesis, submitted by Farwan Alghamdi in partial fulfillment of the requirements for the Degree of Master of Mechanical Engineering from the University of North Dakota, has been read by the Faculty Advisory Committee under whom the work has been done and is hereby approved.

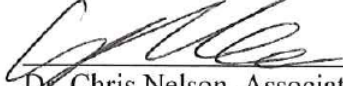
  
\_\_\_\_\_  
Dr. Meysam Haghshenas

  
\_\_\_\_\_  
Dr. Forrest Ames

  
\_\_\_\_\_  
Dr. Anjali Sandip

  
\_\_\_\_\_  
Dr. Ali Alshami

This thesis (or dissertation) is being submitted by the appointed advisory committee as having met all of the requirements of the School of Graduate Studies at the University of North Dakota and is hereby approved.

  
\_\_\_\_\_  
Dr. Chris Nelson, Associate Dean  
Dean of the School of Graduate Studies

  
\_\_\_\_\_  
Date:

## PERMISSION

Title            Small-scale Characterization of Additively Manufactured and Heat Treated  
                  AlSi10Mg  
Department    Mechanical Engineering  
Degree         Master of Science

In presenting this thesis in partial fulfillment of the requirements for a graduate degree from the University of North Dakota, I agree that the library of this University shall make it freely available for inspection. I further agree that permission for extensive copying for scholarly purposes may be granted by the professor who supervised my thesis work or, in her (or his) absence, by the Chairperson of the department or the Dean of the School of Graduate Studies. It is understood that any copying or publication or other use of this thesis or part thereof for financial gain shall not be allowed without my written permission. It is also understood that due recognition shall be given to me and to the University of North Dakota in any scholarly use which may be made of any material in my thesis.

Farwan Alghamdi  
4/25/2019

## **ACKNOWLEDGEMENT**

I wish to express my sincere gratitude to:

Dr. Meysam Haghshenas, my Advisor, for his enormous support, continual encouragement and valuable advice throughout my master's research work and his unwavering patience and motivation.

The members of my advisory committee, Dr. Forrest Ames, Dr. Anjali Sandip and Dr. Ali Alshami for their valuable time, and support towards accomplishing this thesis at the University of North Dakota.

ND EPSCoR and the Department of Mechanical Engineering at UND for providing me financial support during my entire degree period.

I thank all members of my research group, Muztahid, Rezwana and Sara, for their assistance, teamwork and insightful discussions.

Finally, I thank my parents, Adnan and Hala, without their sacrifices I wouldn't have been able to get to this stage in my life, and my siblings, Ghadi, Waad, Shahad and Feras for all their love, prayers and support through the years, I thank Amanda and all of my friends for their endless love, faith and support for me. All my achievements become possible because of them.

## **Abstract**

Selective Laser Melting (SLM) additive manufacturing of aluminum alloys is a layer-wise manufacturing method which can provide lightweight and complex-in-shape automotive, aerospace and medical components with enhanced mechanical properties. In the SLM, the mechanical properties will differentiate depending on the cooling rate as the deposition of material gradation distance from the build plate as well as the deposition direction, in which it has an effect on the microstructure.

The aim of this project is to assess the correlation between microstructure and small-scale characteristics of an additive manufactured AlSi10Mg alloy in the as-printed and heat treated conditions. Post heat treatment cycle were conducted at the elevated temperature of 520 °C solutionizing and then followed by four different cooling rates: water quenching (WQ), air cooling (AC), furnace cooling (FC) and artificial ageing (soaking at 170 °C for 4 hours). The post heat treatment is utilized to homogenize the microstructure and dissolve the formation of anisotropy in the microstructure thus improve the ductility and strengthening the alloy.

Along with the microstructural assessments through optical and scanning electron microcopies, small scale characterizations were performed utilizing a nanoindentation testing approach, a non-destructive, robust, and reliable testing technique.

The Findings show a transformation in the microstructure from cellular grains in the as-printed materials, with needle like silicon fiber colonies, to fragmented coarsened eutectic silicon particles upon the heat treatment. Moreover, coarsened and spheroidized silicon particles, with different sizes, were observed upon various heat treatment cycles. Unlike cast AlSi10Mg alloys, upon heat treatment in the SLM AlSi10Mg alloy, the hardness is decreased which is mainly caused by silicon spheroidization phenomena. Whereas due to the fine microstructure resulted from dual impact of rapid melting and directional cooling caused by repeated cycles of heating, the as-print sample exhibited the highest hardness value. In this project, a comparison of the various SLM AlSi10Mg samples was conducted to understand the correlations between the mechanical properties and produced microstructure and to fully understand spheroidization phenomena.

## Table of Contents

<b><i>ACKNOWLEDGEMENT</i></b>	<b>5</b>
<b><i>Abstract</i></b>	<b>6</b>
<b><i>List of Figures</i></b>	<b>9</b>
<b><i>List of Tables</i></b>	<b>12</b>
<b>1. <i>Introduction</i></b>	<b>13</b>
<b>1.1 Objective</b>	<b>14</b>
<b>1.2 References</b>	<b>17</b>
<b>2. <i>Literature review</i></b>	<b>18</b>
<b>2.1. Additive Manufacturing</b>	<b>18</b>
<b>2.2. Metal Additive Manufacturing (MAM)</b>	<b>19</b>
<b>2.2.1. Powder Bed Fusion (PBF)</b>	<b>19</b>
<b>2.3. AlSi10Mg alloy</b>	<b>24</b>
<b>2.3.1. The Microstructure of conventional cast AlSi10Mg and AM AlSi10Mg alloy</b>	<b>29</b>
<b>2.4. Mechanical properties of AM-SLM AlSi10Mg alloy and conventional cast alloy</b>	<b>32</b>
<b>2.5 Heat treatment of aluminum alloys</b>	<b>40</b>
<b>2.7 Overview</b>	<b>54</b>
<b>2.8 Reference</b>	<b>56</b>
<b>3. <i>Experimental Procedure</i></b>	<b>60</b>
<b>3.1. Part fabrication</b>	<b>60</b>
<b>3.2. Cutting</b>	<b>61</b>
<b>3.3. Heat treatment</b>	<b>62</b>
<b>3.5. Mounting</b>	<b>63</b>
<b>3.6. Polishing</b>	<b>64</b>
<b>3.7. Etching</b>	<b>64</b>
<b>3.8. Optical Microscopy</b>	<b>65</b>
<b>3.9. Scanning Electron Microscopy (SEM)</b>	<b>65</b>
<b>3.10. Nanoindentation</b>	<b>66</b>
<b>3.11 References</b>	<b>69</b>
<b><i>Chapter 4: Results and Discussion</i></b>	<b>70</b>
<b>4.1 Microstructural analysis</b>	<b>71</b>
<b>4.2. Mechanical properties</b>	<b>84</b>
<b>4.3. As-built vs artificially aged</b>	<b>90</b>



<b>4.4 References</b>	<b>99</b>
<b>5. <i>Conclusion</i></b>	<b>101</b>
<b>6. <i>Future Work</i></b>	<b>103</b>

## List of Figures

FIGURE 2.1 THE PROCESS OF POWDER BED FUSION [6]	20
FIGURE 2.2 PROCESSING WINDOW FOR STAINLESS STEEL-CU SINTERED BY A) CO <sub>2</sub> AND B) ND: YAG LASER [7]	21
FIGURE 2.3 SCHEMATIC REPRESENTATION OF THE SLM PROCESS [9].	22
FIGURE 2.4 FIELD EMISSION SCANNING ELECTRON MICROSCOPY (FESEM) IMAGE OF THE POWDER OF GAS ATOMIZED ALUMINUM [9].	24
FIGURE 2.5 AL-SI PHASE DIAGRAM [13]. THE GREEN DASHED LINE SHOWS THE POSITION OF THE ALSI10MG ALLOY.	26
FIGURE 2.6 ALSI10MG ALLOY POWDER UNDER SEM MICROGRAPHS A) SAMPLE OF POWDER B) GRAIN SIZE CLOSE-UP [14]	28
FIGURE 2.7 OPTICAL MICROGRAPHS OF ALSI10MG ALUMINUM ALLOY AFTER LASER PROCESSING A) FORMATION OF SINGLE-TRACK B) MICROSTRUCTURE OF MELTED MIDDLE ZONE [14].	29
FIGURE 2.8 SEM MICROGRAPHS OF ALSI10MG ON AL6082 SUBSTRATE AFTER SELECTIVE LASER MELTING PROCESS A) MICROSTRUCTURE OF UPPER SURFACE FORMATION OF SINGLE TRACK, B) BOTTOM AREA'S MICROSTRUCTURE [14].	29
FIGURE 2.9 FINE EUTECTIC MICROSTRUCTURE IN THE SLM ALSI10MG ALLOY [17].	30
FIGURE 2.10 LEFT) THE ALSI10MG MICROSTRUCTURE IN AS-BUILD SLM FORM; RIGHT) POROSITY IN THE SLM SAMPLE [18].	31
FIGURE 2.11 A) CAST ALSI10MG ALLOY MICROSTRUCTURE-ETCHED; B) CAST ALSI10MG ALLOY AFTER T6 HEAT TREATMENT; C) SLM ALSI10MG ALLOY AFTER T6 HEAT TREATMENT [18]	32
FIGURE 2.12 SINGLE TRACK ALSI10MG [19].	35
FIGURE 2.13 DIFFUSION PROCESS SHOWING A) MELT POOL B) SOLIDIFIED TRACK [21].	35
FIGURE 2.14 ALSI10MG MICROSTRUCTURE A) KEYHOLE MELTING POOL SHAPE B) FINE GRAIN AT MELT POOL AND COARSE AT MELT POOL BOUNDARY [21].	36
FIGURE 2.15 COMPRESSION OF DIFFERENT MELTING POOL MODE THAT RESULT IN DIFFERENT RATE OF HEAT AFFECTED ZONE [21].	36
FIGURE 2.16 CHEMICAL COMPOSITION OF THE ALSI10MG [24].	37
FIGURE 2.17 THE ALSI10MG MICROSTRUCTURE IN AM [30].	38
FIGURE 2.18 ALSI10MG CUBIC SCHEMATIC [34].	39
FIGURE 2.19 STRESS AND STRAIN CURVE OF ALSI10MG [30].	40
FIGURE 2.20 THE PROCESS SCHEMATIC FOR THE TWO-STAGE T6 PROCESS [18].	41
FIGURE 2.21 PARTICLES AND DENSITY VALUES COMPARISON ALONG DIFFERENT HEAT TREATMENT DURATION [38].	43
FIGURE 2.22 VICKERS HARDNESS RESULTS FOR THE AS-BUILT AND HEAT TREATED ALSI10MG [38].	44
FIGURE 2.23 ALSI10MG BRINELL HARDNESS RESULTS [51].	47

FIGURE 2.24 DENSITY OF ALSI10MG WITH VARIOUS HATCH SPACING [35].	49
FIGURE 2.25 SCHEMATIC OF SLM SHOWS THE HATCH SPACING.	50
FIGURE 2.26 TOPOGRAPHY OF ALSI10MG SAMPLES A) 50 MM HATCH SPACING B) 100 MM HATCH SPACING WITH NOTICEABLE SPACING BETWEEN LAYERS [35].	50
FIGURE 2.27 PRESENCE OF PORES WITH VARIOUS SCAN SPEED (A) 250, (B) 500, (C) 750, AND (D) 1000 MM/S [35].	51
FIGURE 2.28 EXAMPLES OF VARIOUS SCAN STRATEGIES A) X-DIRECTION B) Y-DIRECTION C) ALTERNATING [56].	52
FIGURE 2.29 THE PRESENCE OF POROSITY IN THE ALSI10MG MICROSTRUCTURE AT VARIOUS SCAN SPEED WITH DIFFERENT SCAN STRATEGY [35].	53
FIGURE 2.30 THE PERCENTAGE OF POROSITY WITH RESPECT TO ENERGY DENSITY AT SCAN SPEED OF 500 MM/S AND HATCH SPACING OF (50 AND 100) MM [35]	54
FIGURE 3.1 SELECTIVE LASER MELTING MACHINE (SLM200) [1].	60
FIGURE 3.2 SCHEMATIC OF ALSI10MG SAMPLE [2].	61
FIGURE 3.3 BUEHLER- ISOMET CUTTING MACHINE [3].	62
FIGURE 3.4 HEAT TREATMENT CYCLE DIAGRAM: BLACK LINE REPRESENTS ARTIFICIAL AGEING, GREEN REPRESENT AIR COOLING AND RED REPRESENT FURNACE COOLING.	63
FIGURE 3.5 A MOUNTED ALSI10MG SAMPLE (LEFT), SIMPLIMET 1000 MACHINE (RIGHT) [4].	63
FIGURE 3.6 STRUERS- KNUTH ROTOR POLISHER [5]	64
FIGURE 3.7 OPTICAL MICROSCOPIC (LEFT) AND SEM (RIGHT) TO CAPTURE THE MICROSTRUCTURE OF THE ALLOY [6].	65
FIGURE 3.8 HYSTERON TRIBOINDENTER TI 750 [8].	66
FIGURE 3.9 BERKOVICH INDENTER TIP [9].	67
FIGURE 3.10 SCHEMATIC OF BERKOVICH INDENT APPLY F LOAD ON SAMPLE WITH H DISPLACEMENT (LEFT) LOADING AND UNLOADING CYCLE (RIGHT).	67
FIGURE 4.1 A) OPTICAL MICROCOPY IMAGES OF AS-BUILT ALSI10MG AND B) SHOWS HALF CIRCULAR SHAPE GRAIN AT DIFFERENT MAGNIFICATION C) A CLOSE LOOK AT THE GRAIN WHERE “1” IS MELT POOL AND “2” MELT POOL BOUNDARY	71
FIGURE 4.2 SEM IMAGES OF AS-BUILT SAMPLE A) CELLULAR LIKE SHAPE MICROSTRUCTURE WITH AL AS MATRIX, B) A HIGHER MAGNIFICATION SHOWS SI IN DIFFERENT ORIENTATION “1” ELONGATED AND “2” EQUIAXED, C) SHOWS ELONGATED SI AT MELT POOL BOUNDARY “MPB” AND EQUIAXED IN MELT POOL “MP”.	72
FIGURE 4.3 SIDE BY SIDE OM COMPARISON OF A) AS-BUILT, B) ARTIFICIALLY AGED, C) WQ, D) AC, E) FC SAMPLES.	74
FIGURE 4.4 SEM MICROGRAPHS THE ALSI10MG WHEN A) ARTIFICIALLY AGED, B) WQ, C) AC, D) FC.	76

FIGURE 4.5 AL-SI PHASE DIAGRAM SHOWS THE REGION OF ELEVATED TEMPERATURE OF HEAT TREATMENT SOLUTION THAT IS BELOW EUTECTIC TEMPERATURE AROUND 10% OF SI [8]	78
FIGURE 4.6 THE SCHEMATIC REPRESENTATION OF VOLUME AND INTERFACE DIFFUSION RESULTING IN THE SI FRAGMENTATION AND SPHEROIDIZATION [9, 10]	80
FIGURE 4.7 THE SEM MICROGRAPHS OF A) AS-BUILT ALSI10MG, B) AGED, C) WQ, D) AC, C) FC SAMPLES. THE CHANGE IN THE MORPHOLOGY OF THE EUTECTIC SI IS CLEARLY OBSERVED.	83
FIGURE 4.8 LOAD VS DISPLACEMENT CURVES OF THE ALSI10MG SAMPLES, AS BUILT AND HEAT TREATED MATERIALS.	85
FIGURE 4.9 SEM MICROGRAPHS OF THE INDENTATION IMAGES A) AS-BUILT, B) ARTIFICIALLY AGED, C) WQ, D) AC, E) FC.	88
FIGURE 4.11 VICKERS HARDNESS MEASURES OF THE AS-BUILT AND HEAT TREATED ALSI10MG MATERIALS.	90
FIGURE 4.12 SCHEMATIC OF ALSI10MG XY AND YZ PLANES.	91
FIGURE 4.13 NANO-HARDNESS RESULTS FOR THE ALSI10MG SAMPLES, A) YZ PLANE, B) XY PLANE (HEAT TREATED: ARTIFICIAL AGED).	92
FIGURE 4.14 NANO-HARDNESS RESULTS FOR THE ALSI10MG, A) YZ PLANE, B) XY PLANE.	93
FIGURE 4.15 INDENTATION SIZE EFFECT IN THE AS-PRINTED AND HEAT TREATED SAMPLES [1]	95
FIGURE 4.16 THE ISE AND THE CORRESPONDING CHANGES IN THE DISLOCATION CONTRIBUTIONS [14].	96
FIGURE 4.17 SCHEMATIC OF GEOMETRICALLY DISLOCATIONS (GNDS) CREATED DURING THE INDENTATION PROCESS. THE DISLOCATION STRUCTURE IS IDEALIZED AS CIRCULAR DISLOCATION LOOPS [11].	97
FIGURE 4.18 DENSITY OF GNDS VERSUS DEPTH IN THE AS-PRINTED MATERIAL [1].	98

## List of Tables

TABLE 2.1 THE CHEMICAL COMPOSITION OF THE ALSI10MG POWDER [20]	23
TABLE 2.2 THE COMPARISON OF THE MICROHARDNESS OF THE ALSI10MG PRODUCED FROM DIFFERENT TECHNIQUES [24]	34
TABLE 2.3 SLM PARAMETERS TO PRODUCE ALSI10MG [30]	38
TABLE 2.4 MECHANICAL PROPERTIES COMPARISON OF ALSI10MG [44]	46
TABLE 3.1 SPECIFICATION OF SLM 200 [1]	61

## 1. Introduction

Aluminum is the most consumed non-ferrous metallic materials. The global consumption of aluminum is 24 million tons with 18 million obtained from ores while the remaining is recovered from scrap metals, i.e., referred to as secondary aluminum [1]. The aluminum metal possesses a very high affinity for oxygen thus it exists as an oxide (alumina) in the nature. In terms of metallurgical perspective, the metal is a face-centered cubic (FCC) crystal structure characterized by a coordination number of 12 and an atomic packaging factor of 0.74 [2]. The plastic deformation in aluminum occurs via the process of crystallographic slip on the lattice in the plane direction therefore in an aluminum crystal 12 slip systems are leading to the high ductility of the metal [2]. Aluminum melts at 660 °C with a boiling temperature of 2520 °C [3]. The aluminum powder exists in a variety of diameters ranging from 0.015 μm to 17000 μm. Additionally, the metal powder can be in various forms and shapes, i.e., thin flakes, irregular powder, sphere, etc.

AlSi10Mg is an alloy of aluminum in which thermal properties and good strength are very well combined with flexible post-processing capabilities and low weight. It is due to these reasons only that it is widely preferred in automation, aerospace, and automotive [4]. This alloy of aluminum-silicon is primarily used in castings as they have low shrinkage comparatively and high melt fluidity [5]. When magnesium is alloyed to the alloy of Al-Si, the precipitation of Mg<sub>2</sub>Si is enabled due to which the matrix gets strengthened to a considerable extent without the mechanical properties being compromised [4].

Additive manufacturing is one of the most popular technologies of the recent years as it makes it possible to produce complex parts without the limitation of design as was in the case of traditional manufacturing methods. Additive manufacturing is different from subtractive or

normative manufacturing in the form that it follows the 'bottom-up' manufacturing technique where a structure can be built using the approach of layering *i.e.* 'layer-by-layer' approach.

Among various classes of the AM, selective laser melting (SLM) process is best suited to the production of Al-Si alloys and processing of Al-Si powder in order to get parts having functionally gradient material properties and super high strength. The AM-SLM method used to fabricate AlSi10Mg alloy leads to pre-alloyed powder solidification or melting resulting in a fine eutectic microstructure. The mechanical properties of SLM AlSi10Mg are found to be higher or at par to the AlSi10Mg cast material due to very fine distribution and microstructure of the Si phase. Thus, additive manufacturing is so much advantageous as for the SLM AlSi10Mg alloy, there is a high micro-hardness which surpasses the conventional cast alloy and is comparable to the die-cast alloy that has been hardened. There is a significant impact of the microstructure of SLM AlSi10Mg on mechanical properties such as elongation, strength, and fatigue behavior. Also, the imperfections formed in these parts at the time of post-processing procedures and during the process affect the microstructure of these parts [6].

Heat treatment is a common post process technique used to tailor the mechanical, physical and chemical properties of the material and it is used SLM AlSi10Mg to dissolve the formation of anisotropy in the microstructure caused by the layering process and improve the ductility of the alloy [7].

## **1.1 Objective**

The primary objective of this project is to analyze the impact of various cooling rates and heat treatment cycles on the microstructure and mechanical properties of the SLM AlSi10Mg alloys. The mechanical properties (hardness) and the microstructure analyses of various samples of SLM AlSi10Mg were observed through a small scale characterization (Vickers and

Nanoindentation testing) along with microstructural assessments (optical microscopy and scanning electron microscopy). Performing novel heat treatment processes on the SLM AlSi10Mg samples, the hardness values and evaluations on the microstructure were obtained. These were used to compare as-printed and heat treated (WQ, AC, FC and, artificially aged) samples.

The results upon heat treatment show that the microstructure from cellular grains, with coral-like silicon fiber colonies, to fragmented “spheroidized” eutectic silicon particles. In contrast to cast AlSi10Mg alloys, the SLM AlSi10Mg alloy, hardness is decreased; whereas-print presented a high value compared to the Furnace cooling with lowest out of the 5 samples, and that is mainly contributed to stress relief, elimination of solid solution strengthening, and silicon spheroidization phenomena.

The thesis is separated into five chapters as follows:

- The first chapter provides a short introduction to the topic and states and objectives of the project.
- Chapter two is a literature review introduces concept of additive manufacturing, Aluminum and AlSi10Mg alloy; its physical and mechanical properties, and heat treatment process.
- Chapter three provides the experimental procedure conducted in this project.
- Chapter four provides the observed results of the mechanical properties and microstructural features of as-print AlSi10Mg and various heat treated samples. The results were determined using Vickers hardness testing, nanoindentation testing, optical microscopy and scanning electron microscopy. Also it consists of discussion on the results obtained AlSi10Mg samples and further analysis on the relationship between microstructures and mechanical properties for each sample examined.



- Chapter 5 concludes the project with highlighting the main results and introducing future work to further understand the effect of heat treatment cycles on the AlSi10Mg alloy.

## 1.2 References

- [1] Davis, J R. "Aluminum and." *Alloying: Understanding the Basics* (2012): 351-416.
- [2] Ambroziak, A and M T Solarczyk. "Application and mechanical properties of aluminum alloys." *Shell Structures: Theory and Applications* 4 (2018): 525-528.
- [3] Burleigh, T David. "*Corrosion of Aluminum and Its Alloys.*" Totten, G E, and D S MacKenzie. *Handbook of Aluminum, Vol. 2, Alloy Production and Materials Manufacturing.* New Mexico: New Mexico Institute of Mining and Technology, 2003. 421-463.
- [4] Kempen, K., et al. "Mechanical properties of AlSi10Mg produced by Selective Laser Melting" *Physics Procedia* 2012, pp. 439-446.
- [5] Yang, Li, et al. *Additive Manufacturing of Metals: The Technology, Materials, Design and Production.* Cham: Springer International Publishing, 2017.
- [6] Yakout, Mostafa, Stephen Veldhuis and M.A. Elbestawi. "A Review of Metal Additive Manufacturing Technologies ." *Solid State Phenomena* 2018, pp. 1-14.
- [7] Yu, Xianglong and Lianfeng Wang. "T6 heat-treated AlSi10Mg alloys additive-manufactured by selective laser melting." *Procedia Manufacturing* 15 (2018): 1701-1707. Online.

## 2. Literature review

### 2.1. Additive Manufacturing

One of the most popular and disruptive technologies of recent years is additive manufacturing (AM) technology or 3D printing. The AM is based on the principle of 'layer by layer' manufacturing, which makes 'objects' by depositing separate layers of constituent materials [1]. The process is carried out by the means of digitally operated and controlled material setting tools. There are four main components that are essentially included in additive manufacturing broader definition; these include:

- The object's digital model;
- Materials that are integrated in the smallest form such as powder, wire, or liquid droplets;
- A tool for setting the materials;
- The tool's digital control system for building the object's shape by layering the material [2].

Additive manufacturing is different from the subtractive or normative manufacturing in the form that it follows the 'bottom-up' manufacturing technique where a structure can be built using the approach of layering, *i.e.* 'layer-by-layer' approach [3].

The 3D-printed objects are created using many different materials such as ceramics, polymers, and metals. There are seven broad categories into which AM processes have been classified by the International Organization for Standardization/ American Society for Testing and Materials which are Material Extrusion (ME), Directed Energy Deposition (DED), Binder Jetting (BJ), Powder Bed Fusion (PBF), Material Jetting (MJ), Sheet Lamination (SL), and Vat Photopolymerization (VP) [2].

## **2.2. Metal Additive Manufacturing (MAM)**

Direct methods such as electron beam melting, and selective laser melting, and indirect methods such as selective laser sintering, and binder jet processes are common methods used for metal additive manufacturing (MAM). Post-processing such as hot isostatic pressing (HIP) is required in indirect methods to produce parts that have more than 90% density [5]. On the other hand, parts with a density more than 90% are produced directly by direct methods by the means of optimized process parameters. MAM makes it possible to produce complex parts without the limitation of design as in the case of traditional manufacturing methods.

There are two major groups into which the AM processes of metals can be classified broadly; directed energy deposition (DED) based technologies and powder bed fusion (PBF) based technologies [6]. Depending on the type of the source of energy that is being used, both technologies can further be employed. The regions of powder bed are selectively fused by the thermal energy in PBF based technologies. The main processes of this technology are well represented by Electron Beam Melting (EBM), and Selective Laser Melting/Sintering (SLM/SLS). In directed energy deposition technologies, fusing of materials is carried out by focused thermal energy as it melts the metal while their deposition. Arc-based AM, Electron Beam Free Form Fabrication (EBFFF), Direct Metal Deposition (DMD), and Laser Engineered Net Shaping (LENS) are the main technologies based on DED [6].

### **2.2.1. Powder Bed Fusion (PBF)**

In this technology, the molten metal is shielded by putting the powder bed in a partial vacuum or inert atmosphere. Each layer of the metal powder that is already spread over there is scanned by an energy source (electron or laser beam) so that the material is melted selectively. The melting of the material takes place according to the part of the cross-section that is provided by the digital

part model. As shown in Fig. 2.1, upon completion the scanning of one layer, a downward movement of the building chamber piston takes place while an upward movement of the powder chamber's piston takes place by a defined thickness of the layer [6].

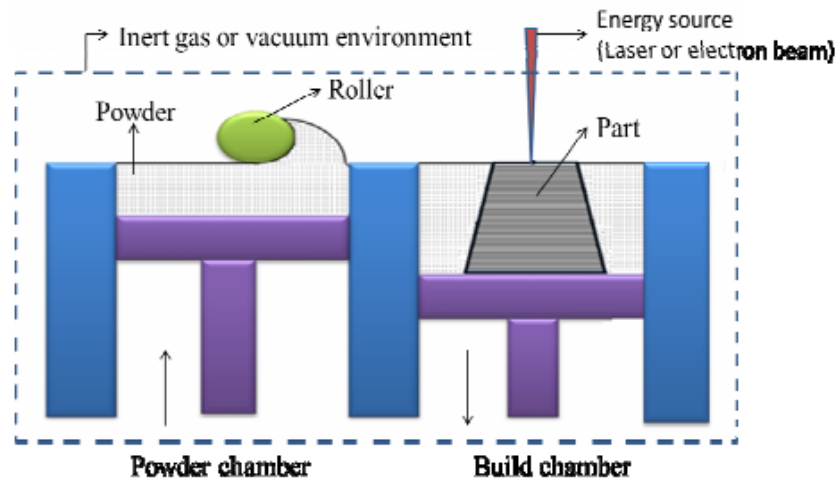


**Figure 2.1 The Process of powder bed fusion [6]**

The process results in the formation of powder cake, which is visible only after the removal of excess powder. In comparison to the DED technologies, the processes based on PBF technologies require more build time. However, it results in a better surface finish and high complexity in which minimum post-processing is needed.

### **2.2.2. Laser-Based Systems**

The laser-based metal additive manufacturing processes that are discussed in this section are SLS or DMLS, SLM, and LENS. The SLS or selective laser sintering is defined as the process that allows the building of structures and complex parts through the formation of multiple layers of powder. The thermal energy which is required for the sintering of the powder is provided by high laser power. When the temperature rises above the metal's melting point, sintering takes place between the particles of the powder [7]. Depending on the type of material, Yb-fiber and CO<sub>2</sub>

lasers are most commonly used. In laser sintering of metal powders, Yb-fiber lasers or Nd: YAG lasers are used most commonly as a wavelength of 1064 nm are generated by these lasers which indicates a high absorptivity for the powders of metal [7]. The SLS processes used in metals are known as DMLS or Direct Metal Laser Sintering. Fig. 2.2 shows the processing window for stainless Steel-Cu which is sintered by CO<sub>2</sub> and YAG laser.

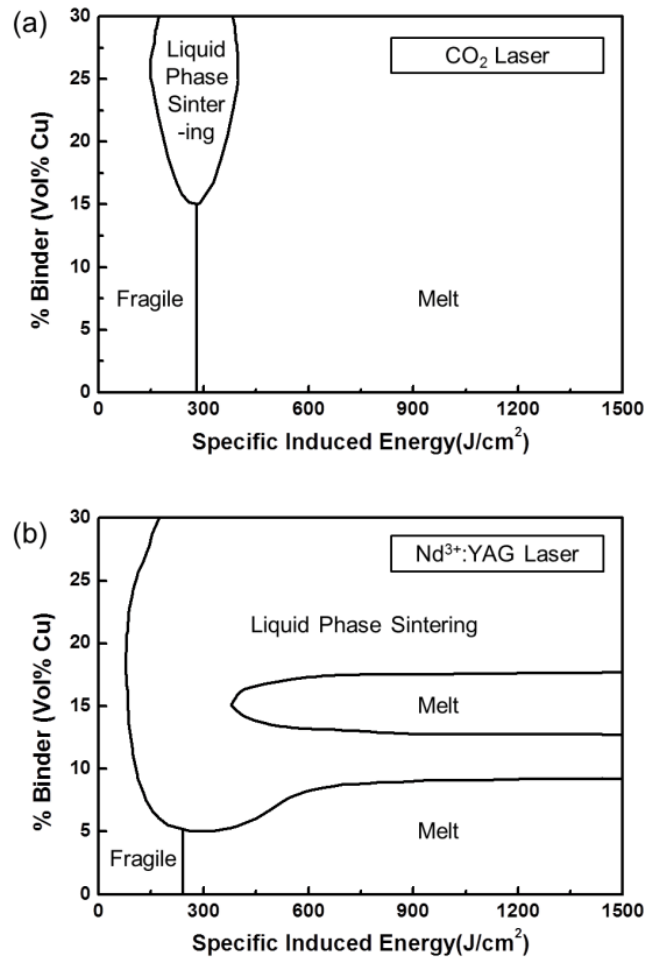


**Figure 2.2 Processing window for stainless steel-Cu sintered by a) CO<sub>2</sub> and b) Nd: YAG laser [7]**

Selective Laser Melting (SLM) is an advanced form of the SLS process in which one or more lasers are used to carry out the full process of/for melting of the particles of the powder bed [8]. After the deposition of a layer of powder on the building platform, the powder bed is directed towards the laser source and selective fusing of the material takes place. Because of the full melting of the powders, fully dense objects are produced having mechanical properties like bulk materials [4].

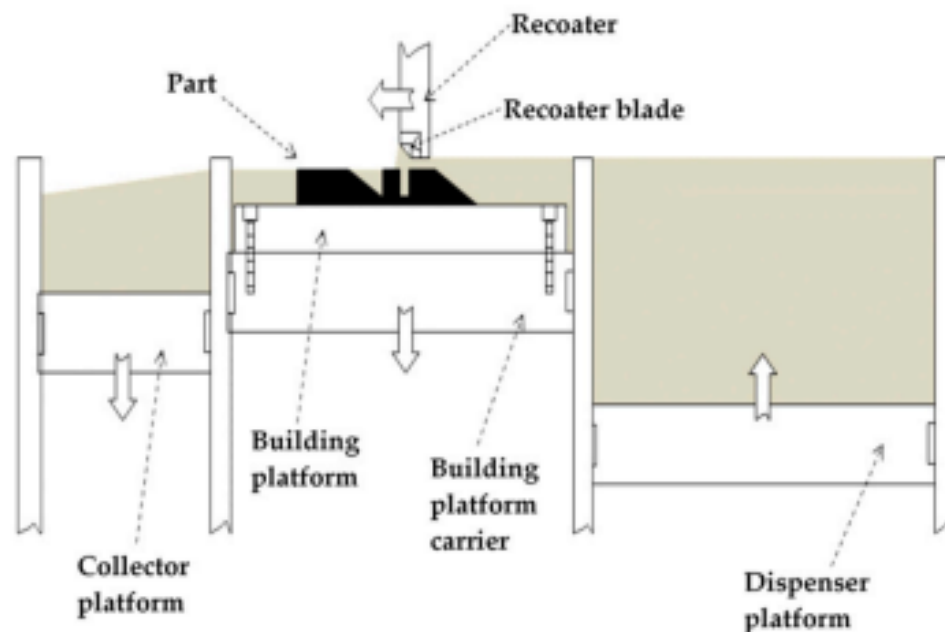


**Figure 2.3 Schematic representation of the SLM process [9].**

The SLM technique is used widely to produce complex shaped components for applications in a few industries such as biomedical, automotive, and aerospace sectors. Recently, it has also been demonstrated that SLM can also be used to produce MMCs i.e. metal matrix composites [9]. Fig. 2.3 shows the schematic of the SLM process.

According to ASTM/ISO 52900, the SLM process is also known by trade name direct metal laser sintering and it produces homogeneous metal objects directly by doing layering from 3D CAD

data, and by using a laser beam to selectively melt the metal powder's fine layers [9]. The currently available lightweight materials that are frequently explored for SLM processing are aluminum and titanium alloys. The most frequently used alloys of aluminum are Al-Si alloys, which contains about 80% of the all casting alloys of aluminum.

There is a large variety of variables and factors by which the final properties of the components are determined. The process parameters and powder properties are two main categories into which components final properties can be divided. Since the process of SLM is dependent on the metallic powders' processing, the fabricated parts' properties are largely dependent on the properties of starting material. Fig. 2.4 shows a typical Al powder which is normally preferred for the SLM processes as they are spherical in shape. Table 2.1 shows the chemical composition of the AlSi10Mg powders.

**Table 2.1 The chemical composition of the AlSi10Mg powder [20]**

Element	Amount (%wt)
Si	9.6
Fe	0.16
Cu	0.003
Mn	<0.001
Mg	0.4
Zn	<0.002
Ni	<0.005
Ti	0.004
Al	Remaining

The powder used for the AM process can either be produced via the gas atomization process or via plasma rotation electrodes. The quality of the powder utilized in the additive manufacturing process typically varies from process to process [35]. The additive manufacturing process entails



the successive deposition of the uniform layers of the powder thus the powder will require certain characteristics such as packing density, flowability and the size distribution [36]. For instances, spherical particles will increase the flowability and the dense packaging of the powder.

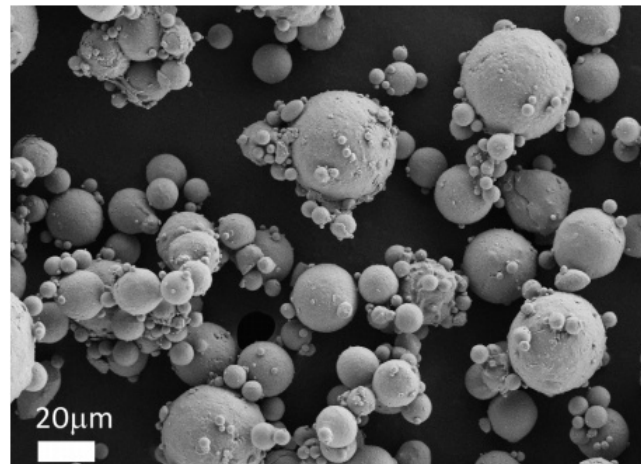


**Figure 2.4 Field Emission Scanning Electron Microscopy (FESEM) image of the powder of gas atomized aluminum [9].**

Some difficulties have been found while working with aluminum alloys because of the challenges posed by laser melting of aluminum due to the characteristics of powder such as poor flowability, high thermal conductivity, high reflectivity, and the oxide layer's stability [9].

Similarly, there is an impact of main process parameters such as scanning speed, layer thickness, hatching distance, and laser power on the intensity and the method that is carried out to send energy to the powder's single layer [9].

### **2.3. AlSi10Mg alloy**

Aluminum (Al) is almost always used as an alloy even if it is more than 99% aluminum [41]. Pure aluminum has a comparably lower strength when compared with its alloys. Pure Al is utilized in electrical connection and applications especially cable conductor. Therefore, alloying aluminum

is common approach to improve its mechanical properties. The primary alloying element is Mg, Cu, and Si used in strengthening aluminum. The elements Sb and Mn are utilized for enhancing corrosion resistance while Cr and Ti are utilized in grain refinement, Ni improves the thermal strength of the element and Co, Fe and Bi for enhancement of the machinability.

Aluminum possesses a low melting point and excellent castability which makes it naturally attractive for casting purposes. This leads to the development of the existing manufacturing processes which allow for complex engineered shaped being produced through melting and casting of aluminum alloys [10].

Among various Al alloys, aluminum-silicon (Al-Si) alloys are used in a large variety of applications in both the automotive and aerospace industries. This is due, in part, to the combination of excellent mechanical properties and castability, along with the alloy's affinity for wear and corrosion resistance [11]. The addition of Si to Al will improve several of its properties such as reduction in the solidification contraction and fluidity. The two components have eutectic reaction especially at 12.6% Si at a temperature of 577 °C [13], see Fig. 2.5. The Al-Si alloy is not, however, easily machined due to the introduction of the hard phases of Si. The addition of Mg in the alloy will lead to the formation of the Mg-Si precipitate that would allow the alloy to heat treatment. The Mg also increases the strength of the element and solubility, improves corrosion resistance and improves weldability and machinability [14].

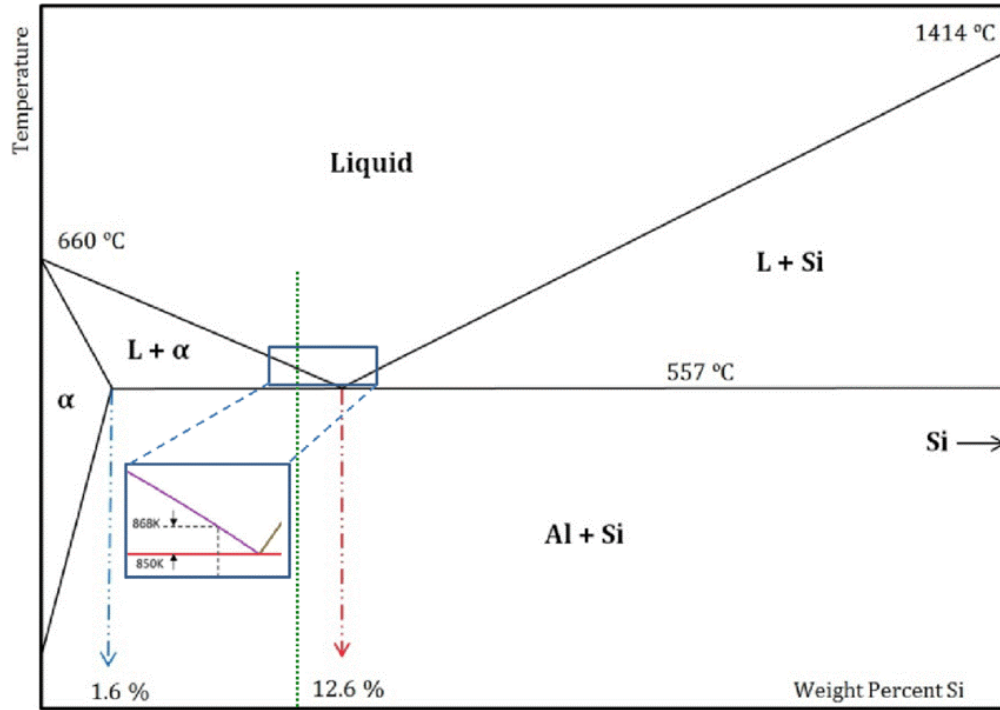


**Figure 2.5 Al-Si phase diagram [13]. The green dashed line shows the position of the AlSi10Mg alloy.**

AlSi10Mg is an alloy of aluminum in which thermal properties and good strength are very well combined with flexible post-processing capabilities and low weight. Due to these reasons, AlSi10Mg alloy is widely preferred in automation, aerospace, and automotive [13]. This alloy of aluminum-silicon is primarily used in castings as they have low shrinkage comparatively and high melt fluidity [12]. When magnesium is alloyed to the alloy of Al-Si, the precipitation of  $Mg_2Si$  is enabled due to which the matrix gets strengthened to a considerable extent without the mechanical properties being compromised [13]. There is a significant impact of the microstructure of SLM AlSi10Mg on mechanical properties such as elongation, strength, and fatigue behavior. Also, the imperfections formed in these parts at the time of post-processing procedures and during the process affect the microstructure of these parts [4].

Cast aluminum alloys possess the highest castability rating where it can be produced within a wide variety of characteristic. One of the common casting methods for aluminum and aluminum alloys is pressure die casting [15]. It began as a mechanical process where the molten metal was pumped under pressure into the molds using hydraulic systems. Aluminum can be cast using all the existing casting methods such as permanent mold, clay/water bonded sand, chemically bonded sand, plaster mold, and investment casting. The advantages of cast aluminum alloys are good fluidity, low melting point, fast rapid heat transfer from molten aluminum to the mold and cost effective. On the other hand, internal porosity during the solidification, stress concentrations at the voids and shrinking during solidification are some limitations of aluminum casting [15].

The SLM process is best suited to the production of Al-Si alloys and processing of Al-Si powder to get parts having functionally gradient material properties and super high strength [14, 15]. The metal powder of AlSi10Mg is comparatively easy to be processed due to a small difference between the solidus and liquidus temperature in comparison to high strength alloys of aluminum (Al-wrought alloys). The initial SLM process is carried out on AlSi10Mg powder which is shown in Fig. 2.6. The aluminum powder has particles spherical in shape and are near cast eutectic casting alloys.

The process of deformation in aluminum occurs via the process of crystallographic slip on the lattice in the plane direction therefore in an aluminum crystal 12 slip systems are leading to the high ductility of the metal. Aluminum melts at 660 °C with a boiling temperature of 2520 °C [16]. The aluminum powder exists in a variety of diameters ranging from 0.015 μm to 17000 μm. Additionally, the metal powder can be in various forms and shapes, *i.e.* thin flakes, irregular powder, sphere, etc. The aluminum powder is classified based on several parameters such as specific surface, apparent density, and oxygen content, these powders can be air atomized,

acicular, water atomized, spherical atomized, granulated, grained, flakes, and fiber, chopped, balled, flitter, cut foil, shot particles, brittle alloy, ultra-fine and machine particles [17].

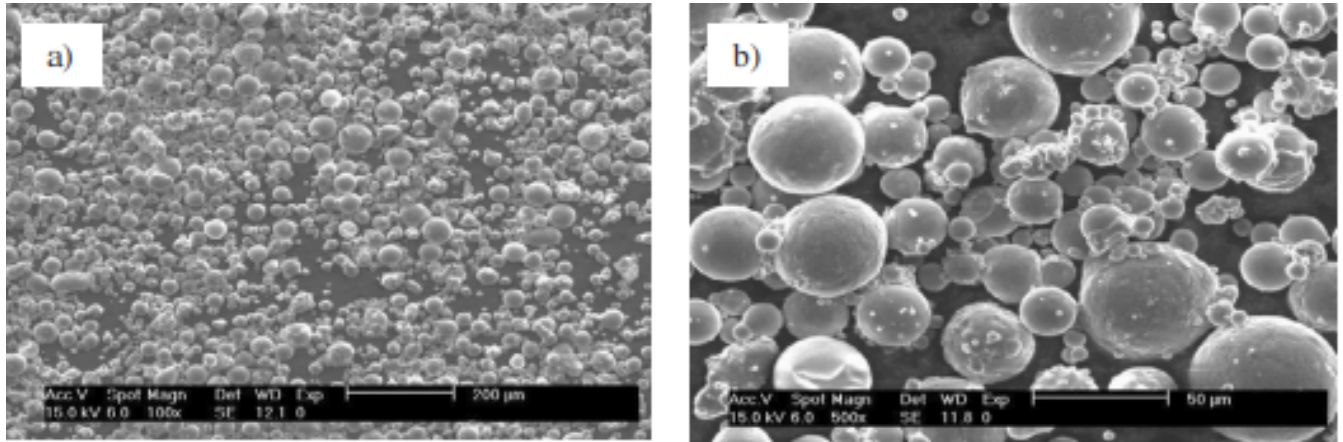


**Figure 2.6 AlSi10Mg alloy powder under SEM micrographs a) Sample of powder b) grain size close-up [14]**

In an experiment carried out by [14], the SLM process investigations were carried out on the AlSi10Mg powder. They deposited a single track of powder of AlSi10Mg on a substrate of Al 6082 after laser processing which is visible in Fig. 2.7. As shown in Fig. 2.7b, the metal powder of melted AlSi10Mg shows a crack-free and dense structure which is easily visible in higher magnification as well.

Fig. 2.8 shows the upper surface layer of the deposited AlSi10Mg under SEM micrographs. In the upper layer, no hard or brittle oxidation is observed which provides a promising ground for the establishment of reactive materials multilayer manufacturing process. The deposited layer's bottom zone shows that it is homogeneous having a smooth transition zone between the powder of the deposited metal and base material [14].

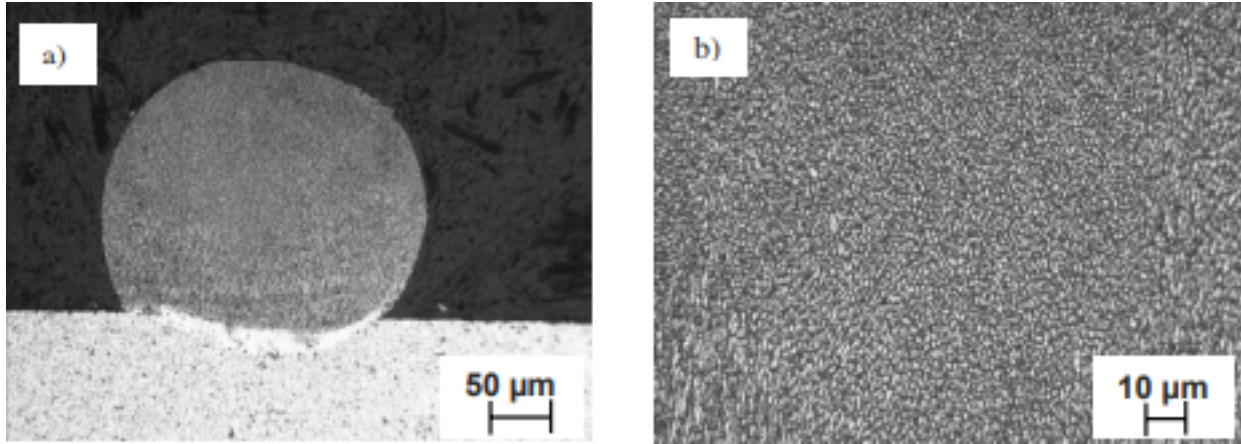


**Figure 2.7 Optical micrographs of AlSi10Mg aluminum alloy after laser processing a) formation of single-track b) microstructure of melted middle zone [14].**

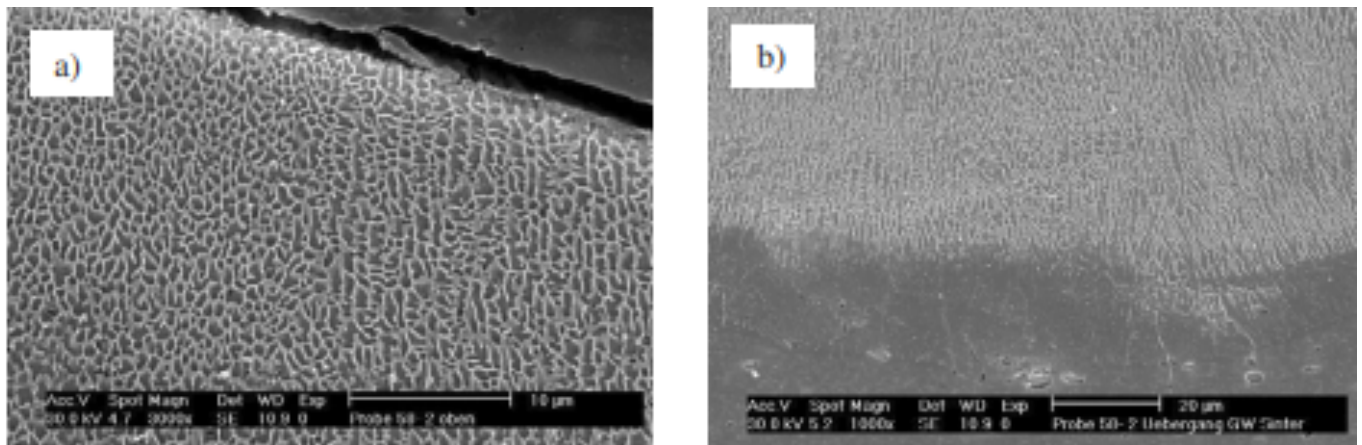


**Figure 2.8 SEM micrographs of AlSi10Mg on Al6082 substrate after Selective Laser Melting process a) microstructure of upper surface formation of single track, b) bottom area's microstructure [14].**

### **2.3.1. The Microstructure of conventional cast AlSi10Mg and AM AlSi10Mg alloy**

The AM-SLM method used to fabricate AlSi10Mg alloy leads to pre-alloyed powder solidification or melting resulting in a fine eutectic microstructure [16]. The dual impact of rapid melting and directional cooling caused by repeated cycles of heating has a great influence on the alloy's

microstructure [17]. Fig. 2.9 shows the AM-SLM AlSi10Mg alloy's fine eutectic microstructure. The borders of the melt pool show a coarse structure due to repeated cycles of melting and solidification. The defects that are included in the additive manufacturing process are shown in the form of asymmetrical pores (solidification) and symmetrical pores (entrapped gas).

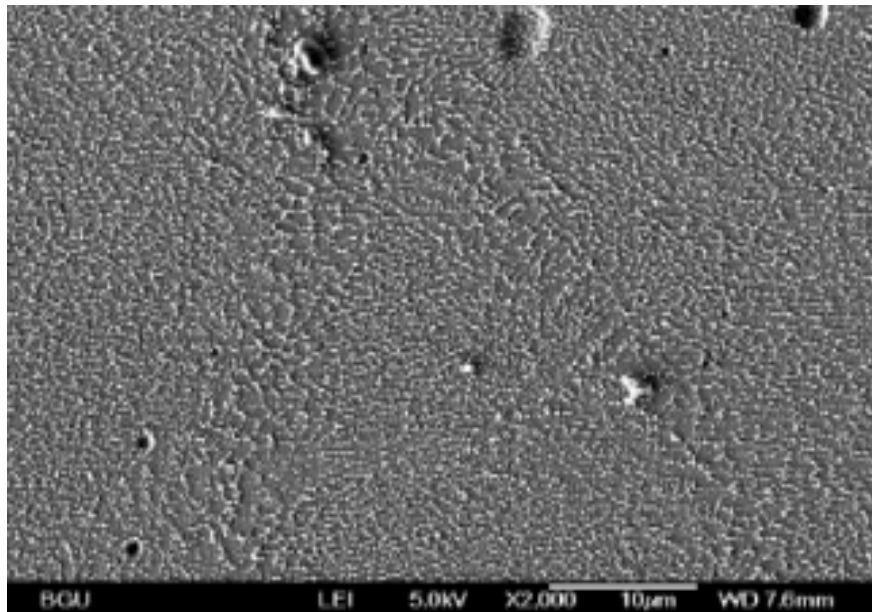


**Figure 2.9 Fine eutectic microstructure in the SLM AlSi10Mg alloy [17].**

In another study carried out by [18], the microstructure of the SLM and the cast AlSi10Mg alloy was studied after T6 heat treatment and in as-built conditions on an optical microscope. Fig. 2.10 shows the AlSi10Mg alloy microstructure obtained by the SLM process in as-built condition, there are three different types of structures of grains. Fine grain structures are seen in melt pool's middle section. Elongated and coarser grain structures towards the source of heat are observed at the sides of the melt pool. Heat affected zone (HAZ) is the area between the overlapping of two melt pools. Fig. 2.10 (right) shows the pores present in the produced cross-section. The length of the key-hole pores varies to around 700 micrometers from 250 micrometers. The smaller spherical pores are known as metallurgical pores [18].

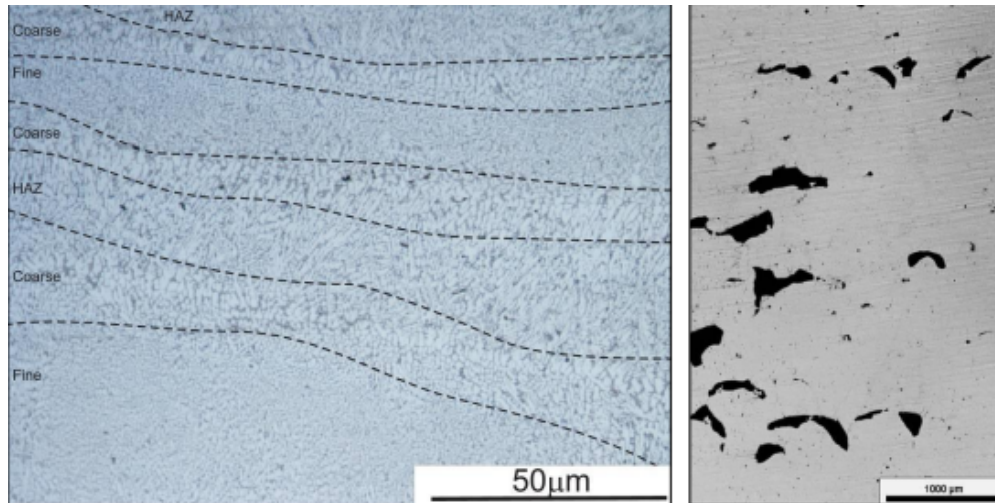


**Figure 2.10 left) The AlSi10Mg microstructure in as-build SLM form; right) Porosity in the SLM sample [18].**

Fig. 2.11 shows the microstructure of cast AlSi10Mg alloy which includes an irregular eutectic phase and large  $\alpha$ -Al grains in the as-delivered structure condition. In Fig. 2.11b, it is indicated that microstructure's morphology has been changed due to the heat treatment. It is also clearly indicated that around the primary grains of  $\alpha$ -Al, spherical particles of Si are located which have been converted from the eutectic phase. The microstructure of SLM AlSi10Mg alloy after T6 heat treatment is demonstrated in Fig. 2.11c. The Si particles are found to be uniformly distributed and grown in the Al matrix in the resulting solution treatment [18].

The impact of preheating during SLM of AlSi10Mg alloy was determined by [17]. They found that at a temperature of 150 °C, a significant reduction in distortion was observed while at 250 °C, no considerable distortion was observed [17]. It was concluded by them that a very fine eutectic microstructure was exhibited by the components of AlSi10Mg which did not require much machining.



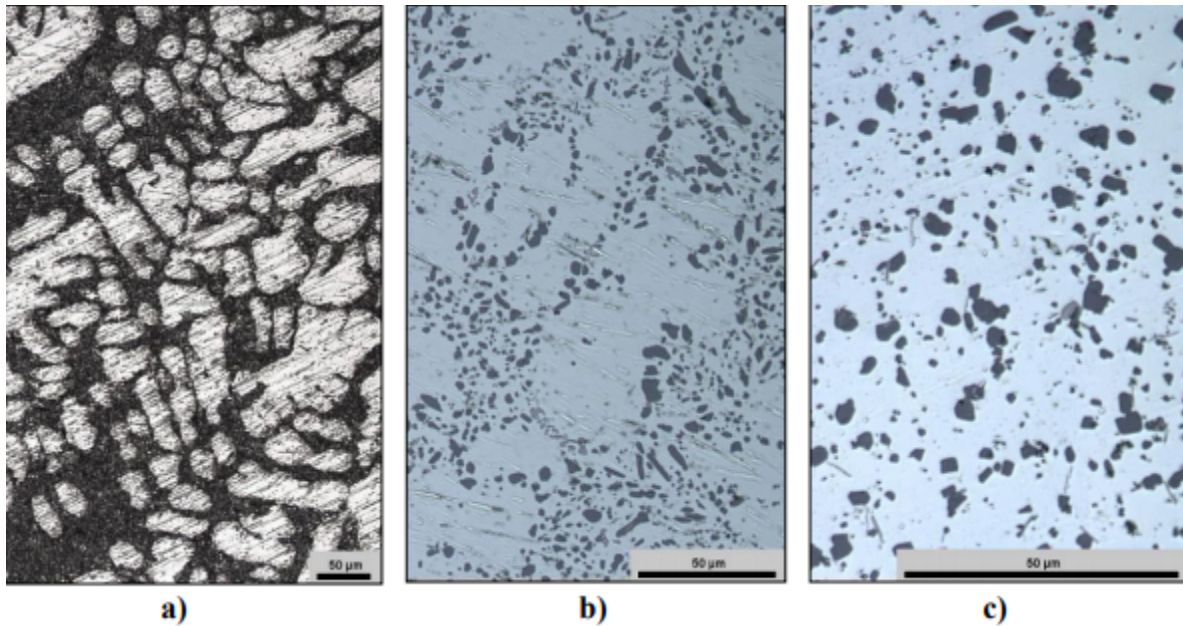


**Figure 2.11 a) Cast AlSi10Mg alloy microstructure-etched; b) Cast AlSi10Mg alloy after T6 heat treatment; c) SLM AlSi10Mg alloy after T6 heat treatment [18]**

#### **2.4. Mechanical properties of AM-SLM AlSi10Mg alloy and conventional cast alloy**

The fracture behavior and mechanical properties response of the AlSi10Mg alloy with respect to different temperatures and treatment regimens show that the elongation values are increased, and the tensile strength is decreased under hot isostatic pressure (HIP) treatment [17]. Additionally, there were considerable changes in the size, dimple shape, and content of porosity with HIP. Normal ductile behavior was exhibited by all the fractured surfaces. Under the treatment of high temperature, the tensile strength is lowered, and elongation values are increased [17].

The mechanical properties of SLM AlSi10Mg are found to be higher than the AlSi10Mg cast material due to very fine distribution and microstructure of the Si phase [17]. Even after conducting a T6 heat treatment on conventional cast AlSi1Mg alloys, the properties for SLM AlSi10Mg are

still higher. For the SLM AlSi10Mg alloy, there is a high micro-hardness which surpasses the conventional cast alloy and is comparable to the die-cast alloy that has been hardened [19].

The Al-Si casting alloys which are desirable for welding have been recently developed using optimization of the AM deposition process via the use of powder bed fusion laser (PBFL) and the direct energy deposition (DED) techniques [20]. The DED technique results in the production of fully dense, functional metal components that is carried out by depositing metal powders on a substrate then utilizing a laser beam as the energy source maintained in a closed-loop control system to regulate the dimensional accuracy and the integrity of the material [2]

The main use of the DED is to generate components used to repair or rebuild a section or a damaged or worn out parts. Moreover, this technology can be used in the manufacture of new elements. The resultant Al-Si has a high reflectivity that may lead to a low rate of energy absorption that may result in the consolidation defects while ageing such as cracks, pores and un-milted areas [22]. In practice, the AlSi10Mg casting is traditionally solidified in a dendritic structure that is made of Al-Si and primary  $\alpha$ -Al at the eutectic phase. The solidification process is substantially influenced by the parameters applied in the process hence the evolution of the microstructure, and the morphology will be affected as well [21]. One experiment [23] illustrated that AlSi11 alloy created from direct melt deposition led had banding microstructure so that the layers, in this case, were solidified with cellular morphology. The structure was further from the substrate particularly after the tenth layers leading to the formation of a dominant dendritic morphology [23]. As mentioned earlier, the resultant microstructure will affect the mechanical properties of the alloy for instance Table 2.2 compares the microhardness of the AlSi10Mg formed from three different processes.

**Table 2.2 The comparison of the microhardness of the AlSi10Mg produced from different techniques [24]**

<b>Process</b>	<b>Microhardness (HV)</b>
SLM	130
Conventional cast alloys	55
Direct melt deposit	107

To better understand the behavior of the SLM AlSi10Mg, a single track “single layer” of the alloy were examined by Aboulkhair et al [24]. Due to the slow scan speed, 250 mm/s, used to produce the single track, it resulted in a microstructure lacking any irregularities, see Fig 2.12, which leads to a decrease in pores formation when building a component [24]. The decrease in pores is a result of the longer exposure time to the laser heat [24]. The single track was built on top of cast AlSi substrate, where the melting pool of AlSi10Mg powder were melted into the cavity created by laser beam and solidified (Fig. 2.12). Just like in welding, where one can apply different modes such as conduction or keyhole, and that depends on beam power and feed speeds, see Fig 2.14, SLM exhibit same procedure. Due to the high energy transfer “the ratio between the laser energy absorbed by material and the laser power compared to the material’s absorptivity” and the slow scan speed, a keyhole melting pool shape was observed when single track was created [24, 25]. The melt pool zone shown in Fig. 2.13a has a depth that is more than half its width which indicates that it is keyhole mode rather than conduction [24, 26]. Thus, the laser beam penetrates deeply, it results in minimizing the heat affected zone, Fig. 2.15.

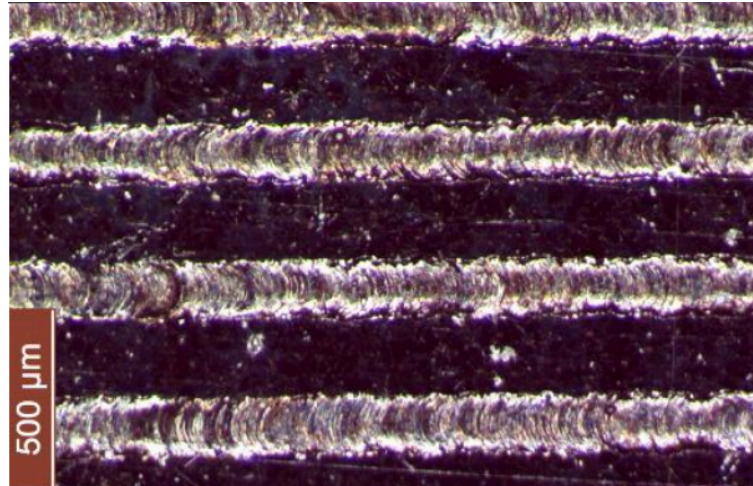


Figure 2.12 Single track AlSi10Mg [19].

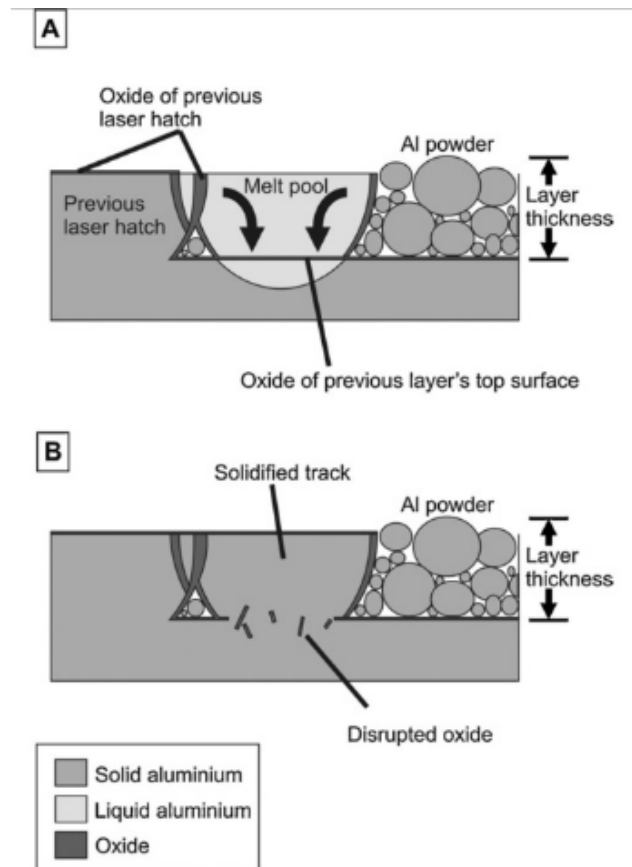


Figure 2.13 Diffusion process showing a) melt pool b) solidified track [21].

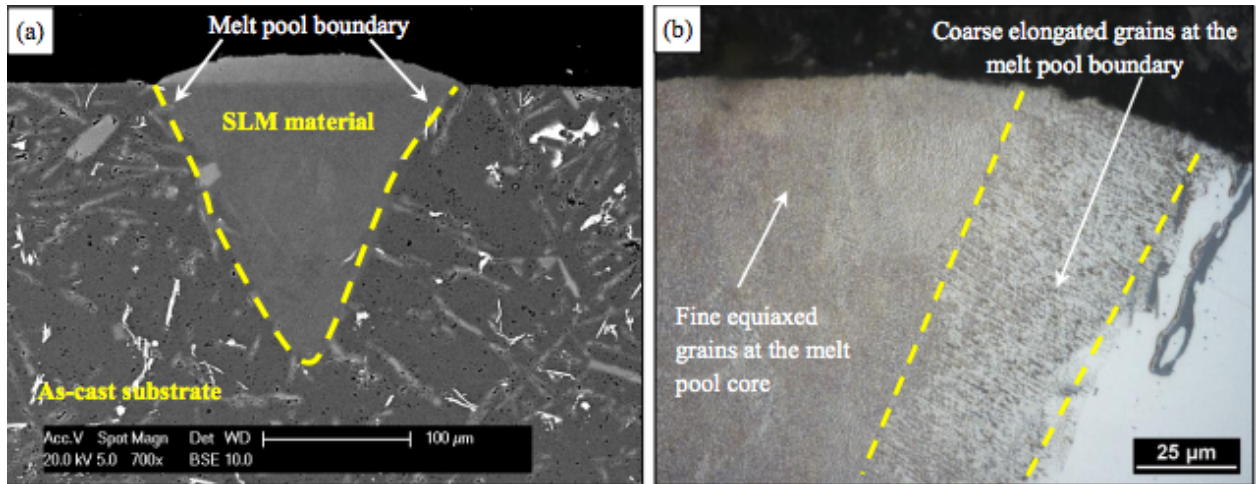


Figure 2.14 AISi10Mg microstructure a) keyhole melting pool shape b) fine grain at melt pool and coarse at melt pool boundary [21].

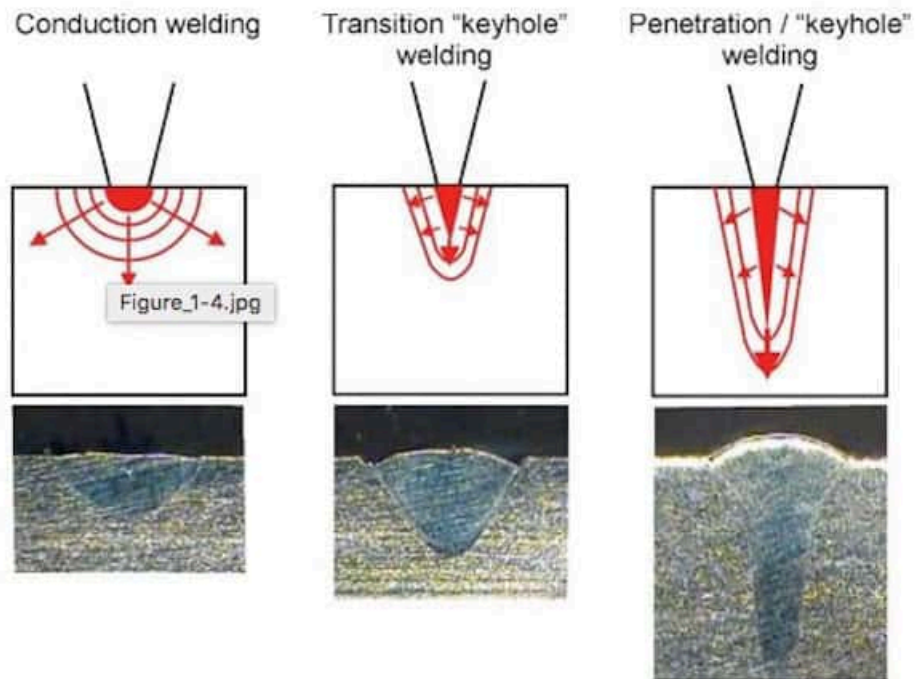
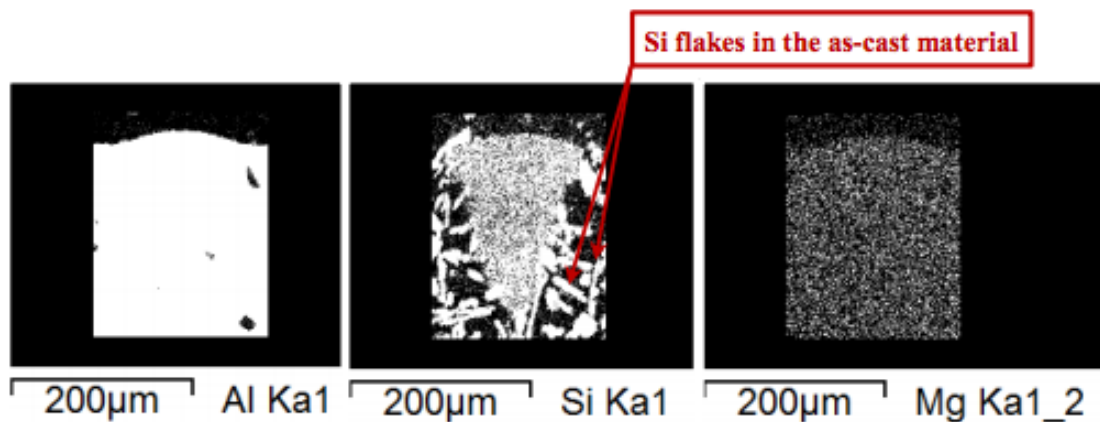


Figure 2.15 Compression of different melting pool mode that result in different rate of heat affected zone [21].

Due to the fast-rapid cooling, that result into a fine microstructure at the melting pool zone, the melt pool boundary exhibits coarsened form and elongate because of the thermal gradient. To validate that thermal conductivity plays a role on the microstructure, similar study conducted on SLM AlSi10Mg cubes [24, 28, 29] proving that with a lower thermal conductivity of Al substrate, the result is identical where the melt pool boundary is coarser compared to the core. Moreover, same behavior occurs when comparing SLM and cast AlSi10Mg, where cast alloy has a coarser microstructure and that because of low solidification rate that allow the Si to diffuse with Al matrix creating Si flakes, see Fig. 2.16 [24]. Because of the fine microstructure, the mechanical properties of the SLM alloy improved, in particularly the nano-hardness of SLM alloy is twice the value of the cast alloy where the average nano-hardness of the SLM alloy was  $2.2\pm 0.1$  GPa but average nano-hardness of cast alloy was  $0.9\pm 0.03$  GPa [24]. The authors pointed out that the results on SLM alloy were uniform and that due to the homogenous microstructure compared to the cast alloy.



**Figure 2.16 Chemical composition of the AlSi10Mg [24].**

Multi-track printing is preferred over a single track as it provides more information and confident before building the whole component. Aboulkhair et al [24] provided great studies over the past

few years on the additive manufacturing of the AlSi10Mg alloys and their metallurgical behaviour; for instance, in a study [24] cubic and dog-bone shaped samples were produced to demonstrate hardness and tensile tests respectively using parameters in Table 2.3. The AlSi10Mg exhibited a typical uniform homogenous distribution (due the fast solidification [30]). As a result, a fine microstructure with constant needle like Si fibers at the grain boundaries was produced, see Fig. 2.17. Moreover, due the fine microstructure, a uniform nano-hardness values with an average of  $1.82 \pm 0.01$  GPa was observed which is higher than its cast counterpart [30].

**Table 2.3 SLM parameters to produce AlSi10Mg [30]**

Laser power (W)	Point distance ( $\mu\text{m}$ )	Exposure time ( $\mu\text{s}$ )	Hatch spacing ( $\mu\text{m}$ )	Layer thickness ( $\mu\text{m}$ )
200	80	140	130	25

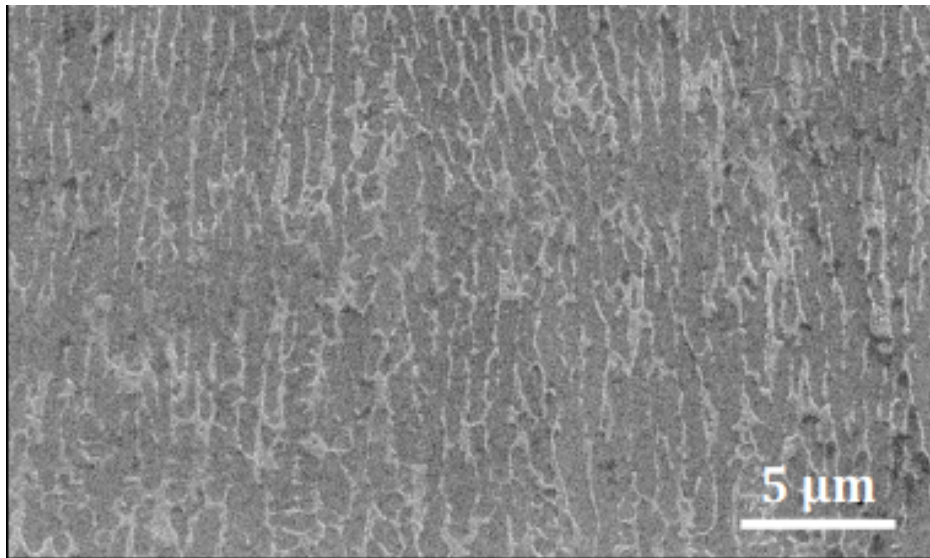


**Figure 2.17 The AlSi10Mg microstructure in AM [30].**

In addition, micro-hardness “Vickers” was obtained to have an average of  $109.7 \pm 0.9$  HV for XY plane where average micro-hardness for YZ plane was  $99.07 \pm 2$  HV [30]. the different in results between XY and YZ plane is due to the anisotropy behavior that caused by grain of the multi-layer

structure and thermal conductivity, see Fig. 2.18 [6,7,8]. More important, the micro-hardness of SLM AlSi10Mg is still higher than its cast counterpart with a value of 95 HV [30,32].

Read et al [30] extracted the mechanical properties by extrapolating the stress-strain curve where the SLM alloy behaved in a brittle manner, in which tensile strength was about 320 MPa and yield strength at 175 MPa (higher than cast alloy), see Fig. 2.19 [30, 33]. On the other hand, the ductility of the SLM alloy was less than the cast only (around 3% elongation) [9]. The main reasons for enhanced mechanical properties in the the SLM alloys are grain size reduction developed by rapid solidification, solid solution strengthening, and dislocation strengthening [30].

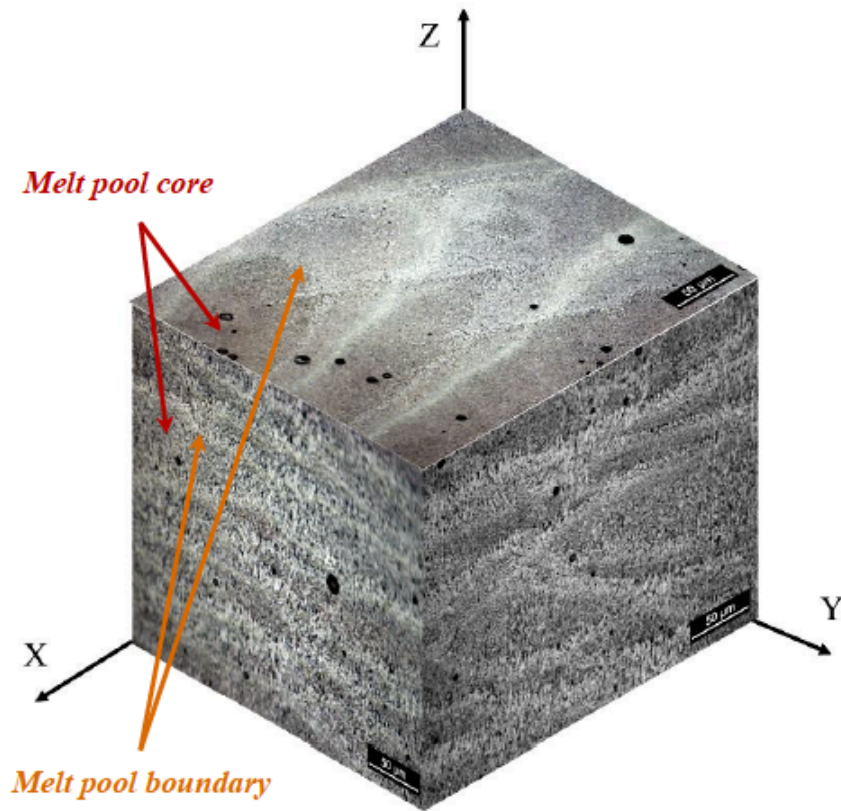


**Figure 2.18 AlSi10Mg cubic schematic [34].**



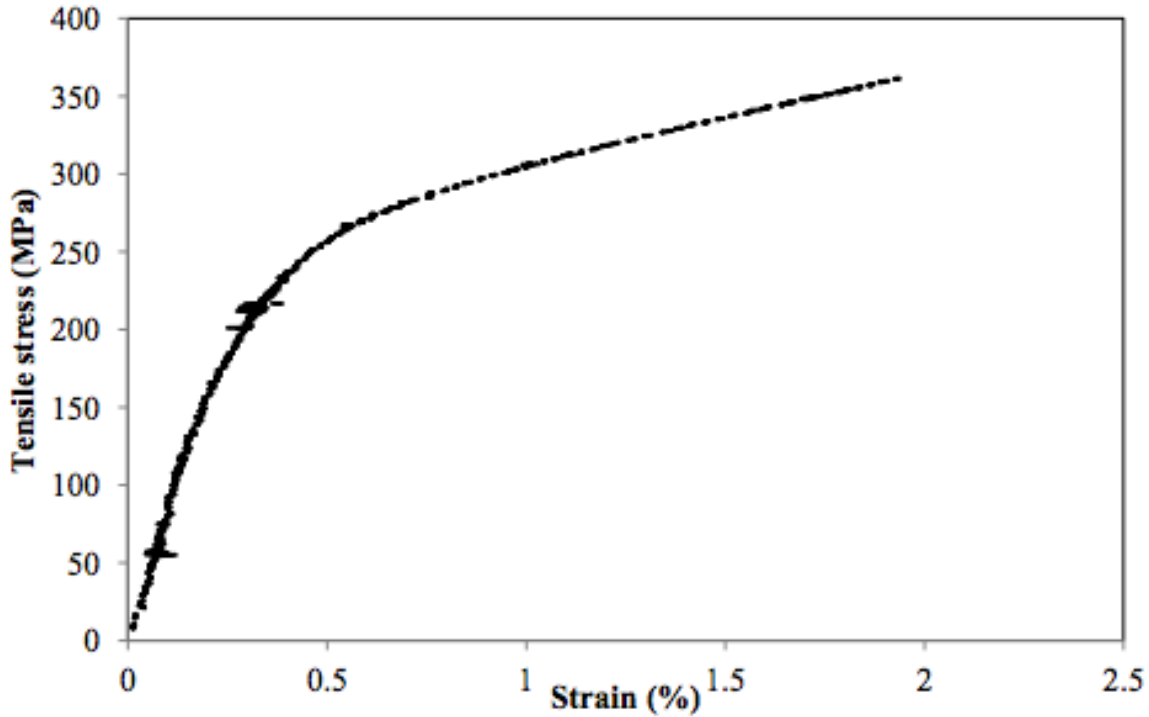


**Figure 2.19 Stress and strain curve of AlSi10Mg [30].**

## **2.5 Heat treatment of aluminum alloys**

The cast AlSi10Mg requires the T6 treatment (Fig. 2.20) for improvement of the performance, for instance, the temperature for the solution and ageing treatment are 500-545°C and 150-180°C, respectively [24]. The components created from the SLM AlSi10Mg require heat treatment since upon the solution, ageing and quenching treatments there is the formation of anisotropy in the microstructure caused by the layering process. The heat treatment will dissolve the microstructure and improve the ductility of the alloy [33].

The addition of Si to Al will improve its properties such as reduction in the solidification contraction and fluidity. The two components have eutectic reaction especially at 12.6% Si at a temperature of 577 °C [13]. The Al-Si alloy is not easily machined due to the introduction of the hard phases of Si. The addition of Mg in the alloy will lead to the formation of the Mg<sub>2</sub>Si

precipitates that would allow the alloy to be heat treated. The Mg also increases the strength of the element and solubility [34].

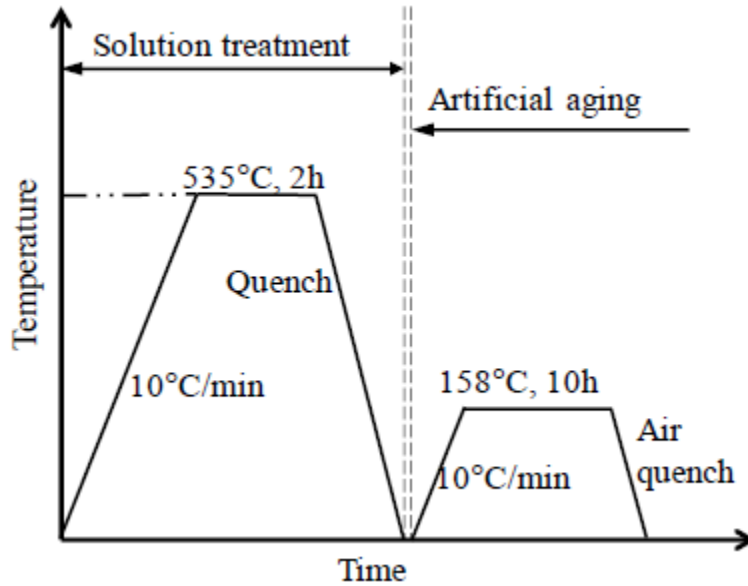


**Figure 2.20** The process schematic for the two-stage T6 process [18].

The heat treatment process of Al-Si-Mg takes the following sequence:

- *Solution heat treatment (SHT)*

This process entails the heating of the material at a high temperature in a single-phase region, but not exceeding the solid temperature but below the eutectic temperature that will avoid overheating or inducing localized heating [35].

- *Quenching*

The hot material is quenched to room temperature which entails rapid cooling to room temperature to create a supersaturated solid solution (SSSS). Water is typically used in the quenching process for large objects, but for the small parts, the process may introduce residual stress thus an alternative quenching rate of boiling water is utilized or sometimes air-cooling [13].

- *Ageing or precipitation hardening*

The ageing process can either be natural or artificial thus the product can be kept at an elevated desired temperature for a specific duration of time to permit the SSSS to decompose into a fine precipitate.

Several studies have explored the effect of such heat treatment on the SLM alloy and have compared SLM with their cast counterpart. According to Aboukir et al [38] the hardness varies depending of the duration of the treatment; overall hardness value decreases after heat treatment and that is due to the difference in strengthening mechanisms [38]. The heat treatment cycle used by Aboukir et al [29, 38] includes: homogenizing at elevated temperature of 793 K for various times, i.e. 1, 2, 3 and 4 hrs, then quenching to maintain supersaturated structure, and finally artificial ageing between 423-453 K for different time windows (6, 8, 10 and 12 hrs) [38]. The particles in microstructure during the solutionizing began to form with a specific size and density and their size increased with different range of time duration with average sizes of 1.04 and 1.42  $\mu\text{m}$  for the 3 and 4 hours respectively [38]. On the other hand, the density of the particles decreased with increasing solutionizing duration that because the particles combined to form larger particles but remained constant quantity [38]. When artificial ageing utilized, both particles size and density did not show significant changes, see Fig. 2.21 [38].

To further investigate the change in the SLM AlSi10Mg microstructure, the authors conducted a hardness tests “Vickers”. Although with the increasing of the solutionizing time duration, the hardness values were slightly increased yet all of them showed a significant drop in the hardness values compared to the as built sample, see Fig. 2.22, where during solutionizing the alloy softened and with the increase of time duration the particle sizes increased [38]. Moreover, the hardness value increased after the being artificially aged and that is due to  $\text{Mg}_2\text{Si}$  precipitates formation,

and it the different time duration of this process has a slight effect of the hardness value [38]. It is important to mention that the hardness value after the heat treatment cycle still lower than the as built value.

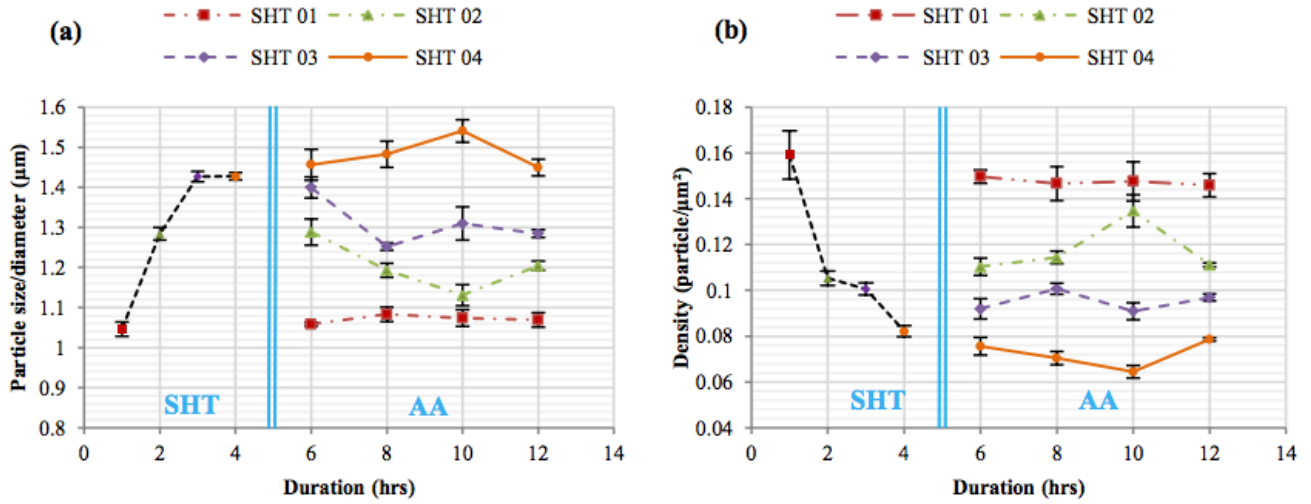


**Figure 2.21 Particles and density values comparison along different heat treatment duration [38].**

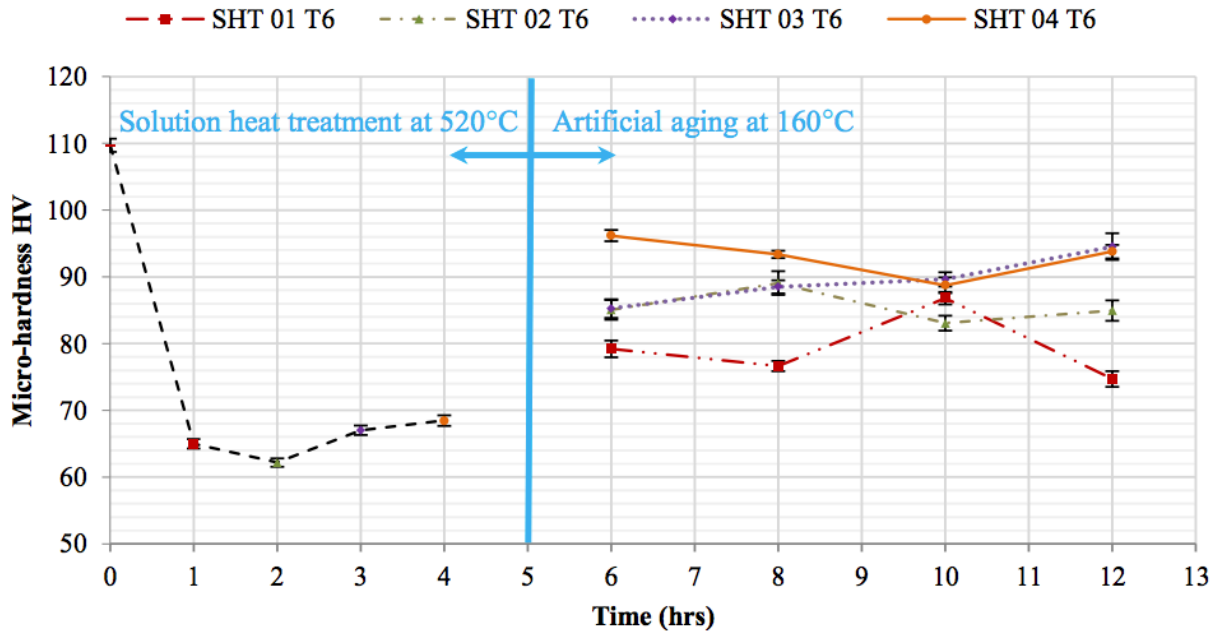


**Figure 2.22 Vickers hardness results for the as-built and heat treated AlSi10Mg [38].**

As mentioned in the previous study [29], the as built SLM AlSi10Mg mechanical properties are affected by three main strengthening mechanisms, where mainly the reduction of the grain size thus increases of grain boundaries that block the dislocation motion. On the other hand, Orowan strengthening is the mechanism observed as precipitates in the heat-treated alloy microstructure where these precipitates act as obstacles to stop the dislocation motion along with solid solution strengthening and dislocation strengthening [38, 39]. Important to notice that the strength of the alloy decreases if alloy is overaged, and it is because the increasing size of precipitates that lower the effect of Orowan strengthening [38, 40, 41].

Sjölander and Seifeddine [40, 41] compared the SLM alloy with its cast counterpart; in terms of microstructural behavior before and after the heat treatment cycle, they reached the following conclusions:

- A fine microstructure with continuous Si separation represented in SLM alloy whereas a coarsened microstructure with Si flakes in cast alloy [38,42]
- After the heat treatment, the SLM microstructure coarsened to become a solid Si whereas in the cast alloy a fine Si particle formed and clustered at the grain boundaries [38, 42]
- The hardness value for the SLM decreased after the heat treatment whereas the hardness values increased for the cast alloy [38,43].

Using another heat treatment approach, Aboulkhair et al [44, 45] investigated the nano-hardness of the SLM alloy of same cubic samples to deeply understand the local mechanical properties characterization. The heat treatment cycle was in following sequence a solution heat treatment for 1 hr at 520°C followed by quenching, then immediately the samples were artificial aged for 6 hrs at 160°C [44, 45]. The result of nanoindentation showed uniform hardness within the alloy, yet an outstanding spatial variation was observed after heat treatment. The fine microstructure is of the uniformity in the as built sample whereas the spatial variation was due to phase transformation during treatment in which during solutionization the Si particles had enough to diffuse, form spheroids and coarsen [45, 46]. The average nano-hardness of the as-built SLM was  $1.82 \pm 0.01$  GPa whereas the average nano-hardness was reduced to  $1.52 \pm 0.02$  GPa after heat treatment [44]. The decrease in nano-hardness after heat treatment is attributed to softening and that is due the changes in the strengthening mechanisms of the microstructure as explained previously. After heat treatment, the microstructure is no longer fine structure, but Si particles spheroid “spherodisation” resulting in strengthening the alloy through Orowan strengthening [44]. Thus, the dislocation motion in the as-built is limited by the increased volume of grain boundaries where in the heat-treated alloy it is through obstruction by the Si spheroids. Furthermore, micro-hardness “Vickers”,

provides the same trend as the nano-hardness results where the as-built alloy was  $125 \pm 1$  HV and the heat-treated alloy was  $100 \pm 1$  HV which conforming the alloy softening [44, 45]. Moreover, the heat treatment cycle produces harder alloy when used on cast sample, where it increased the micro-hardness from 95 HV to 130 HV [44,47] and that caused by precipitating  $Mg_2Si$  through solution heat treatment and artificial ageing [4, 48].

A macro analysis was conducted as well, to provide the tensile strength and the ductility of the alloy before and after the heat treatment. The as-built samples behaved in a brittle manner under tensile loading, whereas the heat treatment enhanced the alloy ductility. According to the authors, brittle failure originated at a surface flaw and it is because of the poor surface roughness, or the presence of sub-surface defects “pores or laser spatter” [44,50] and that fracture surface was flat with a few regions showing shear lips [44,51].

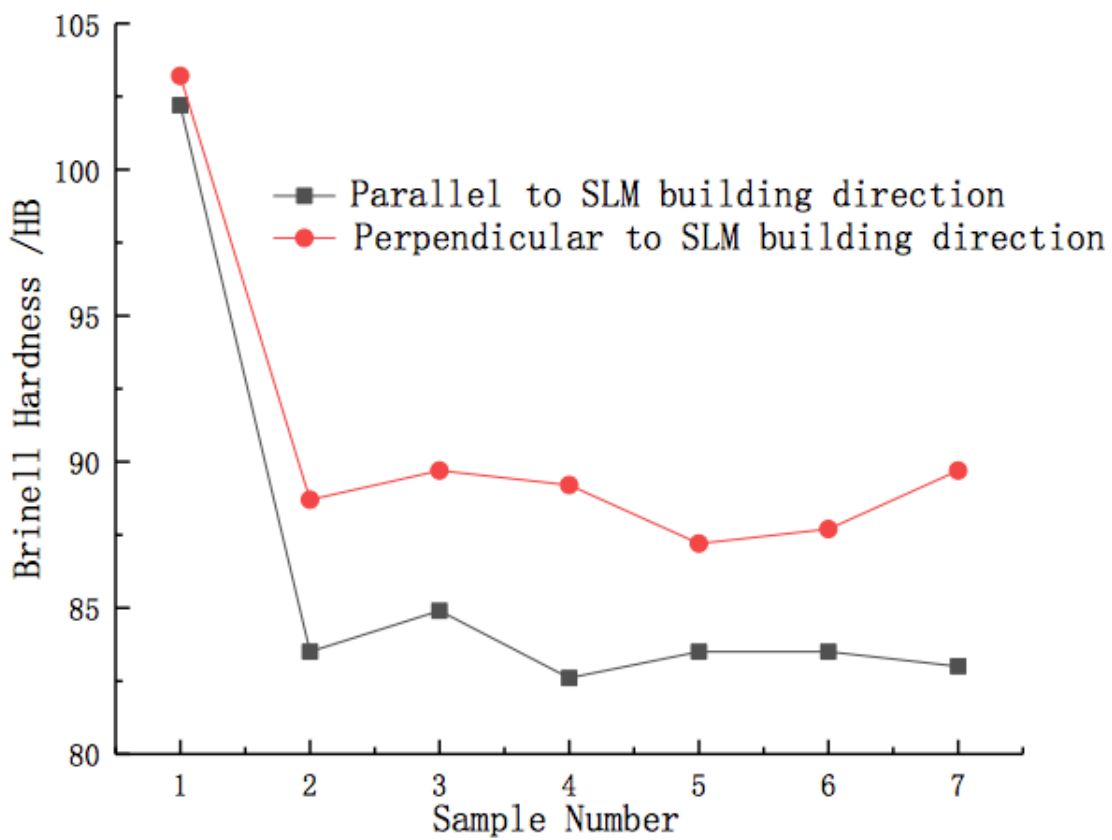
The results in Table 2.4 show a decrease in the heat treated SLM alloy’s ultimate tensile strength, yield strength, because of microstructural coarsening, because of grain boundary reduction that behave as obstacle for the dislocations motion during deformation. On the other hand, the ductility of heat-treated alloy enhanced. The ultimate and yield tensile strengths of the as-built SLM material were higher than the cast counterpart but presented poorer elongation.

**Table 2.4 Mechanical properties comparison of AlSi10Mg [44]**

Sample	Yield strength (MPa)	Ultimate Strength (MPa)	Elongation (%)
SLM - As-built	$268 \pm 2$	$333 \pm 15$	$1.4 \pm 0.3$
SLM – Heat treated	$239 \pm 2$	$292 \pm 4$	$3.9 \pm 0.5$
Cast	175	320	3.0

Yu et al [51] studied the effect of heat treatment on SLM AlSi10Mg through Brinell hardness test as well as its microstructure. The SLM samples were heat treated at an elevated temperature of

535 °C and then artificial aged for 10 h at 158 °C. The average hardness of the as-built alloy was 102.2 HB on XY plane and 103.2 HB on YZ plane [51]. On the other hand, the average hardness of the heat-treated alloy was 83.5 HB on XY plane and 88.7 HB on YZ plane [51]. From the results, a significant drop in the hardness values are observed which confirm the results, see Fig. 2.23. The authors explained the reason for this lower hardness after heat treatment and it is because of the fine grain recrystallization of the microstructure formed during solutionizing [51].



No. 1, As-built; Nos. 2-7, Heat-treated

**Figure 2.23 AlSi10Mg Brinell hardness results [51].**

In the as-built samples, as it contains the cellular dendritic microstructure and the spread of eutectic Si in the matrix, high hardness values were observed [48, 51, 52]. However, the solutionizing dissolved the Si particles in the microstructure and made the hardness reduce significantly.



Although, artificial aging can initiate the precipitation of the  $Mg_2Si$  phase [53], this transformation only causes a limited backlash to the hardness values. Thus, the heat treatment could relieve stresses and enhance ductility instead of benefiting to hardness values. Important to notice that propagate in the heat-treated samples which can cause the Si particles to spheroidize around oxidation regions to create a dimple structure thus enhance the mechanical properties [51].

## **2.6 Parameters in additive manufacturing**

To achieve the desired mechanical properties, almost fully dense AlSi10Mg need to be produced. The dense of the alloy depends on the parameters of the AM technique used, the main parameters to provide a part with minimum porosity are hatch spacing, scan speed and scan strategy [35]. Hatch spacing is the distance between track or layers see Fig. 2.24, as the distance decreases the denser the sample becomes, see Fig. 2.25. The increase of hatch spacing would create gap between the tracks which would cause balling when continue creating multi-tracks samples see Fig. 2.26. Thus, accumulation of balling would create porosity that increases with the increase of hatch spacing [35].

When it comes to the speed of scanning, it has significant impact of the porosity formed in the microstructure not only quantitatively but also qualitatively. The presence of porosity in the alloy is inevitable but by altering the parameters, the porosity percentage would get lower or higher, these porosities are of different types. A metallurgical porosity is small spherical shaped hydrogen porosity trapped in the melt pool due to the low scanning speed, see Fig. 2.27 [35]. This type of porosity would decrease with the increasing of speed scanning, but keyhole porosity “keyhole instabilities” would appear because of the rapid solidification creating [35]. Moreover, with increasing of scan speed, balling would occur that is due to the large distance of hatch spacing of

a single scan, as a result the alloy powder would be fully melt. Important to mention that to reduce the balling, altering the scan strategy would be required, to be discussed later in this section.

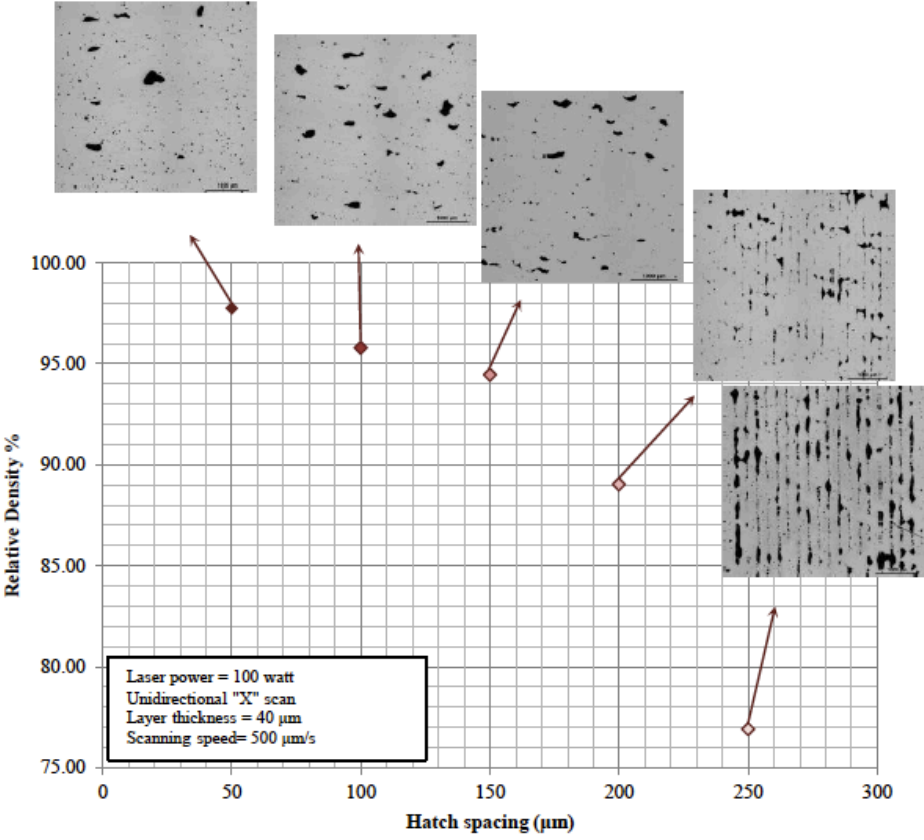


Figure 2.24 Density of AlSi10Mg with various hatch spacing [35].

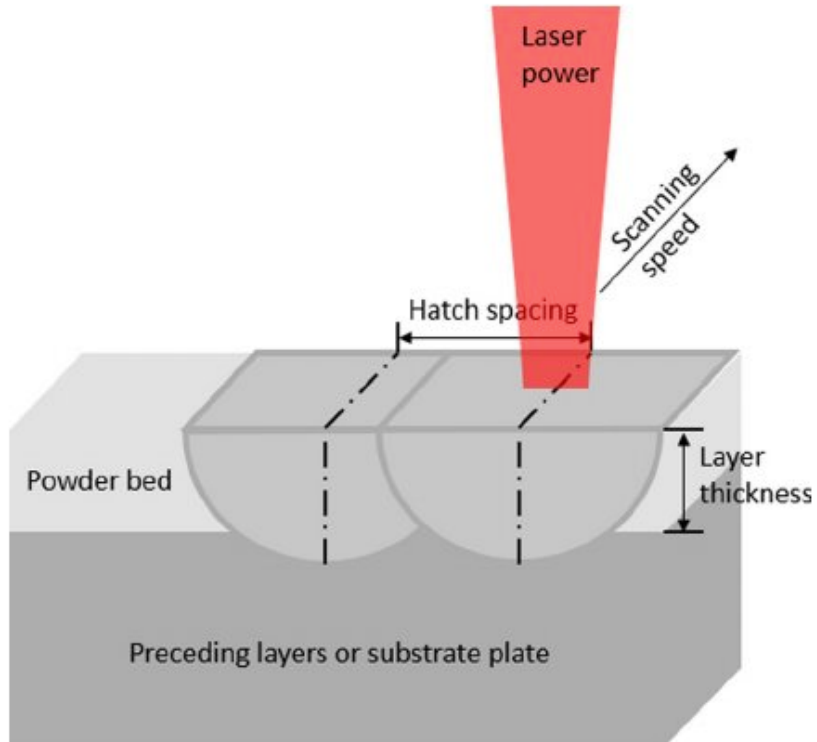


Figure 2.25 Schematic of SLM shows the hatch spacing.

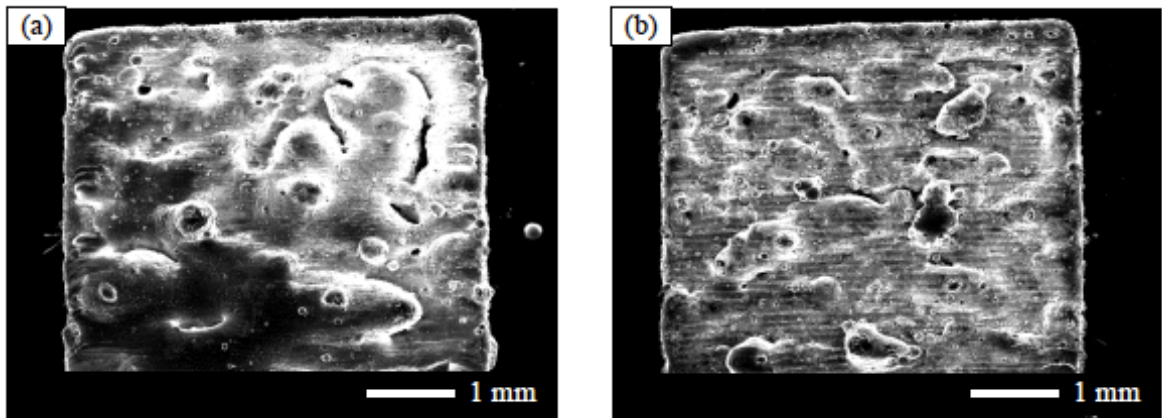
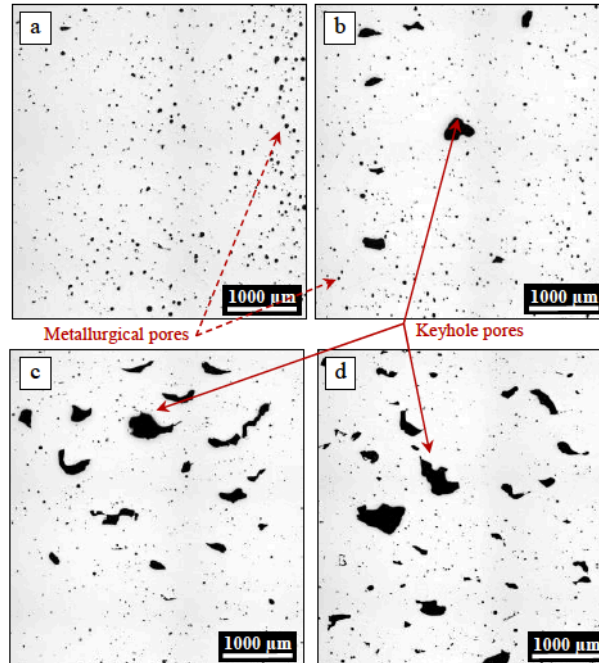


Figure 2.26 Topography of AlSi10Mg samples a)  $50\ \mu\text{m}$  hatch spacing b)  $100\ \mu\text{m}$  hatch spacing with noticeable spacing between layers [35].

The hatch spacing, and the scan speed proportionally affect the energy density through Eq. 2.1 [35]. Even though energy density and the presence of porosity can be related, yet it is important to mention to observe what type of porosity would be presented.

$$\text{Areal Energy Density} = \frac{\text{Laser power}}{\text{Hatch Spacing} * \text{Scan Speed}} \text{ (J/mm}^2\text{)} \quad (2.1)$$



**Figure 2.27 presence of pores with various scan speed (a) 250, (b) 500, (c) 750, and (d) 1000 mm/s [35].**

As mention before, scan strategy affects the presence and type of porosity on the microstructure. By scanning the same layer twice or over lapping or pre-melting “alternating, checkerboard etc” see Fig. 2.28, a decrease in keyhole porosity would be achieved in the microstructure see Fig. 2.29. But it important to mention that at a lower scan speed the double scanning strategy would produce metallurgical pores and that is due to the high amount of energy.

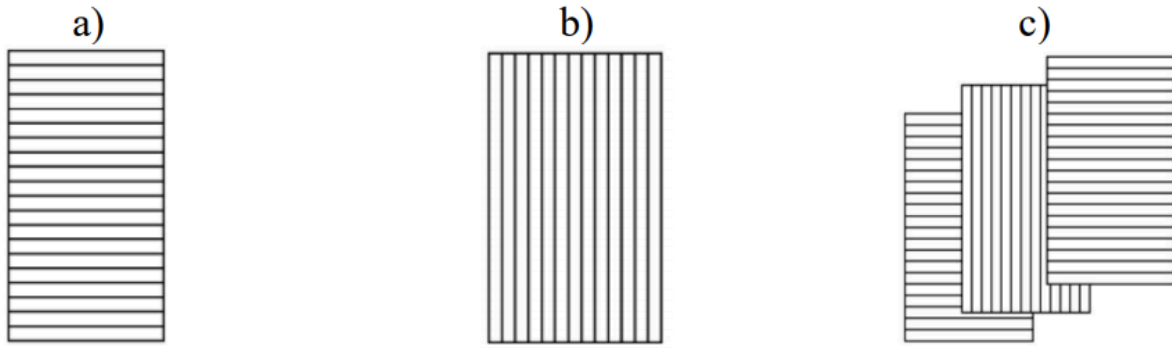


**Figure 2.28 Examples of various scan strategies a) x-direction b) y-direction c) alternating [56].**

According to Aboulkhair et al [35], at scan speed of 500 mm/s, hatch spacing of 50  $\mu\text{m}$  and using the pre-melting strategy with 100 W laser power, a 40  $\mu\text{m}$  layer thickness with  $99.77 \pm 0.08$  % dense sample can be produced, see Fig. 2.30 [35]. Similar results were achieved with a 200 and 900 W laser power [47, 15]. The importance of finding the balance between these parameters would result in the desired almost fully dense microstructure of AlSi10Mg with improved mechanical properties.

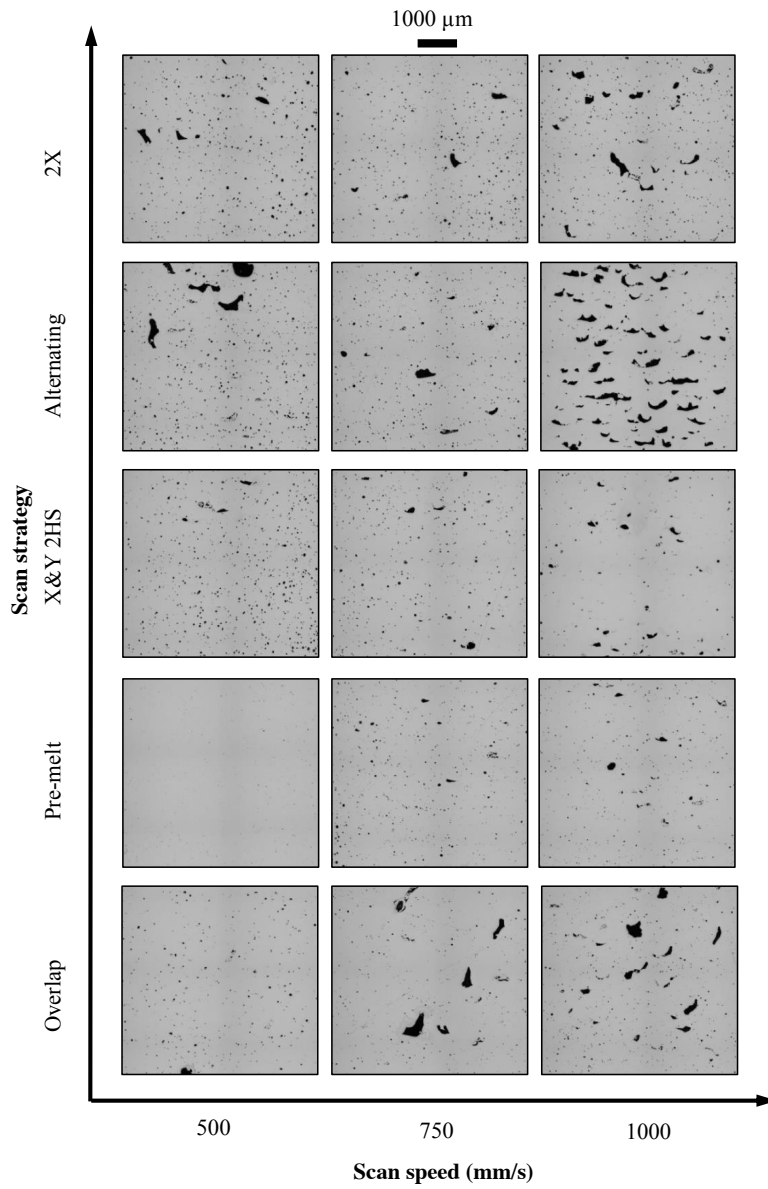


**Figure 2.29 The presence of porosity in the AlSi10Mg microstructure at various scan speed with different scan strategy [35].**

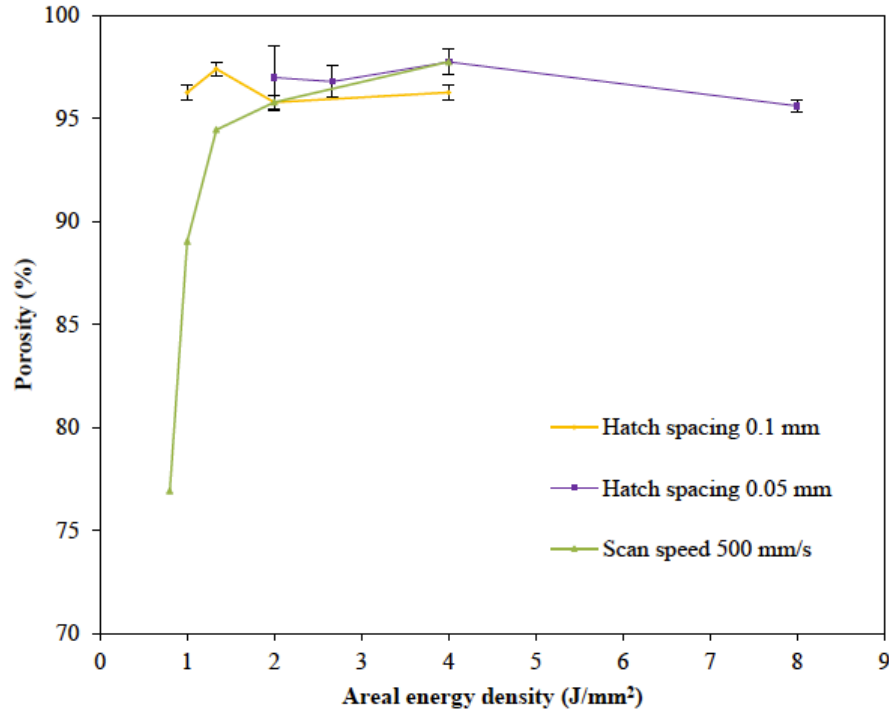


**Figure 2.30 The percentage of porosity with respect to energy density at scan speed of 500 mm/s and hatch spacing of (50 and 100)  $\mu\text{m}$  [35]**

## 2.7 Overview

Aluminum alloys are being used as alternatives to steel in the automotive industry due to the changes in the standards for fuel efficiency, recycling, air pollution and safety [20]. This has led to most components such as, cylinder heads, suspension link, wheels, pumps, engine heads, engine blocks, calipers, etc. to be created from aluminum alloy. Initially, the Aluminum parts were made from foundry processing, low pressure or gravity die casting. For instance, the Al-Si alloys have been hardened via the addition of Mg which will form the  $\text{Mg}_2\text{Si}$  precipitates when the solution is treated then naturally or artificially aged [21].

In this chapter a brief literature review was provided on the additive manufacturing, the metal additive manufacturing, and additive manufacturing on the AlSi10Mg alloy. This is a friendly

alloy for the MAM, however, in most cases, to reach the desired mechanical and microstructural properties, different post processing techniques are required. To this end, heat treatment, *i.e.* T6, and the HIP are quite common.

Current thesis aims at assessing the microstructure and the local mechanical properties induced through additive manufacturing and T6 heat treatment on an AlSi10Mg alloy.

The post heat treatment cycle will enhance the mechanical properties of AM AlSi10Mg using artificial ageing. However, due the lack of published reports and results on the AlSi10Mg alloy with various cooling rate such as Air Cooling, Furnace Cooling and water Quenching, the focus for this study is to expand and explore of such methods. Therefore, the novelty of this work is detailed characterization of the controlling mechanisms of microstructural evolution in the printed and the heat treated AlSi10Mg alloys. In the following chapters, first, the experimental procedures that were conducted in this project will be provided. Then, the main results are presented and discussed in the preceding chapters. Finally, the main conclusions that were extracted from this study along with suggestions for the future works will be provided.



## 2.8 Reference

- [1] Santos, David and Almudena Alvarez. ADDITIVE MANUFACTURING FEASIBILITY STUDY & TECHNOLOGY DEMONSTRATION. Art and Strategic Report. Zaragoza: eda.europa.eu, 2018.
- [2] Tofail, Syed, Susmita Bose and Elias Koumoulos. "Additive manufacturing: scientific and technological challenges, market uptake and opportunities." *Materials Today* 2018, pp. 22-37.
- [3] Gibson, Ian, David Rosen and Brent Stucker. *Additive Manufacturing Technologies: 3D Printing, Rapid Prototyping, and Direct Digital Manufacturing*. New York: Springer Science, 2010.
- [4] Yakout, Mostafa, Stephen Veldhuis and M.A. Elbestawi. "A Review of Metal Additive Manufacturing Technologies" *Solid State Phenomena* 2018, pp. 1-14.
- [5] Yang, Li, et al. *Additive Manufacturing of Metals: The Technology, Materials, Design and Production*. Cham: Springer International Publishing, 2017.
- [6] Bhavar, Valmik, Shreyans Khot and Prakash Kattire. "A Review on Powder Bed Fusion Technology of Metal Additive Manufacturing." 4th International conference and exhibition on Additive Manufacturing Technologies-AM-2014. Bangalore, 2014, pp.1-7.
- [7] Lee, Hyub, et al. "Lasers in Additive Manufacturing: A Review" *International Journal of Precision Engineering and Manufacturing-Green Technology* 2017, pp. 307-322.
- [8] Lucas, Briantais. "Metal Additive Manufacturing:Process, Conception and Post-treatments." *Technic*
- [9] Trevisan, Francesco, et al. "On the Selective Laser Melting (SLM) of the AlSi10Mg Alloy: Process, Microstructure, and Mechanical Properties." *Materials (Basel)* 2017, pp. 1-23.
- [10] Lboro University. *About Additive Manufacturing*. Technical Report. Leicestershire: lboro.ac.uk, 2017.
- al Report. 2017.
- [11] Milewski, John O. *Additive Manufacturing of Metals: From Fundamental Technology to Rocket Nozzles, and Custom Jewelry*. Cham: Springer International Publishing, 2017.
- [12] Li, Xiaodan, et al. "Structure and Mechanical Properties of the AlSi10Mg Alloy Samples Manufactured by Selective Laser Melting." *IOP Conference Series: Materials Science and Engineering*. Shenyang: Shenyang Aircraft Industry, 2017. 1-5.
- [13] Kempen, K., et al. "Mechanical properties of AlSi10Mg produced by Selective Laser Melting" *Physics Procedia* 2012, pp. 439-446.
- [14] Ullrich, Sven, et al. "New Developments of Laser Processing Aluminum Alloys via Additive Manufacturing Technique." *Physics Procedia* 2011, pp. 393-401.
- [15] Buchbinder, D., W. Meiners and J. Bultmann. "High Power Selective Laser Melting (HP SLM) of Aluminum Parts" *Physics Procedia* 2011, pp. 271-278.
- [16] Awd, Mustafa, et al. "Comparison of Microstructure and Mechanical Properties of Scalmetal<sup>®</sup> Produced by Selective Laser Melting and Laser Metal Deposition." *Materials* 2017, pp. 1-17.

- [17] Rosenthal, Idan, et al. "Post-processing of AM-SLM AlSi10Mg specimens: Mechanical properties and fracture behavior." *Advanced Material Densification* 2015, pp. 33-38.
- [18] Zygula, Krystian, Bart. Nosek and Hubert Pasiowiec. "Mechanical properties and microstructure of AlSi10Mg alloy obtained by casting and SLM technique." *World Scientific News* 2018, pp. 462-472.
- [19] Aboulkhair, Nesma, et al. The microstructure and mechanical properties of selectively laser melted AlSi10Mg: the effect of a conventional T6-like heat treatment. Technical Report. Nottingham: University of Nottingham, 2017.
- [20] Girelli, L, et al. "Optimization of heat treatment parameters for additive manufacturing and gravity casting AlSi10Mg alloy." 2017 International Conference on Building Materials and Materials. Lyon, France: IOP Conf. Series: Materials Science and Engineering, 2017. 1-8. Print.
- [21] Javidani, M, et al. "Additive Manufacturing of AlSi10Mg Alloy Using Direct Energy Deposition: Microstructure and Hardness Characterization." *Journal of Thermal Spray Technology* 26 (2017): 587-597. Print.
- [22] Iturrioz, A, et al. "Selective laser melting of AlSi10Mg alloy: influence of heat treatment condition on mechanical properties and microstructure." *Welding in the World* 62.4 (2018): 885-892. Online.
- [23] Dinda, G P, A K Dasgupta, and J Mazumder. "Evolution of Microstructure in Laser Deposited Al-11.28%Si Alloy." *Surface and Coatings Technology* 206 (2012): 2152-2160. Online.
- [24] Aboulkhair, Nesma & Maskery, Ian & Tuck, Christopher & Ashcroft, Ian & M. Everitt, Nicola. (2015). On the formation of AlSi10Mg single tracks and layers in Selective Laser Melting: Microstructure and Nano-mechanical properties. *Journal of Materials Processing Technology*. 230. 10.1016/j.jmatprotec.2015.11.016.
- [25] Yadroitsev, I. Gusarov, A., Yadroitsava, I., and Smurov, I., "Single track formation in selective laser melting of metal powders," *J. Mater. Process. Technol.* 210(12), 1624-1631 (2010).
- [26] King, W. E., Barth, H. D., Castillo, V. M., Gallegos, G. F., Gibbs, J. W., Hahn, D. E., Kamath, C., Rubenchik, A. M., Observation of keyhole-mode laser melting in laser powder-bed fusion additive manufacturing," *J. Mater. Process. Technol.* 214(12), 2915-2925 (2014).
- [27] Aboulkhair, N. T., Everitt, N. M., Ashcroft, I., and Tuck, C., "Reducing porosity in AlSi10Mg parts processed by selective laser melting", *Additive Manuf.* 1-4 (0), 77-86 (2014).
- [28] Baudouy, B. and Four, A., "Low temperature thermal conductivity of aluminum alloy 5056," *Cryogenics* 60, 1-4 (2014).
- [29] Aboulkhair, Nesma & Stephens, Alex & Maskery, Ian & Tuck, Christopher & Ashcroft, Ian & M Everitt, Nicola. (2015). MECHANICAL PROPERTIES OF SELECTIVE LASER MELTED AlSi10Mg: NANO, MICRO, AND MACRO PROPERTIES.
- [30] Read N, Wang W, Essa K, Attallah MM. Selective laser melting of AlSi10Mg alloy: Process optimisation and mechanical properties development. *Materials & Design* 2015 (65) 417-424.
- [31] Kempen K, Thijs L, Van Humbeeck J, Kruth JP. Mechanical Properties of AlSi10Mg Produced by Selective Laser Melting. *Physics Procedia* 2012 (39) 439-446
- [32] Properties of aluminum alloys tensile creep and fatigue data at high and low temperatures. Materials Park (Ohio): ASM International 1999.

- [33] Yu, Xianglong and Lianfeng Wang. "T6 heat-treated AlSi10Mg alloys additive-manufactured by selective laser melting." *Procedia Manufacturing* 15 (2018): 1701-1707. Online.
- [34] Ambroziak, A and M T Solarczyk. "Application and mechanical properties of aluminum alloys." *Shell Structures: Theory and Applications* 4 (2018): 525-528.
- [35] Aboulkhair, Nesma T. Additive manufacture of an aluminum alloy: processing, microstructure, and mechanical properties. Nottingham, UK: University of Nottingham, 2015.
- [36] SriLathabai. "Chapter 2 - Additive Manufacturing of Aluminium-Based Alloys and Composites." *Fundamentals of Aluminium Metallurgy* (2018): 47-92.
- [37] Wong, Kaufui V, and Aldo Hernandez. "A Review of additive manufacturing." *International Scholarly Research Network* (2012): 1-10.
- [38] Aboulkhair, Nesma & Tuck, Christopher & Ashcroft, Ian & Maskery, Ian & M. Everitt, Nicola. (2015). On the Precipitation Hardening of Selective Laser Melted AlSi10Mg. *Metallurgical and Materials Transactions A*. 46. 10.1007/s11661-015-2980-7.
- [39] K. Ma, H. Wen, T. Hu, T. D. Topping, D. Isheim, D. N. Seidman, E. J. Lavernia, and J. M. Schoenung, *Acta. Mater.*, 2014, vol. 62, pp. 141-155.
- [40] J. F. Nie and B. C. Muddle, *Mater. Sci. Eng. A*, 2001, vol. 319-321, pp. 448-451. [16] E.
- [41] Sjölander and S. Seifeddine, *J. Mater. Process. Technol.*, 2010, vol. 210, pp. 1249-1259.
- [42] Sjölander and S. Seifeddine, *Mater. Des.*, 2010, vol. 31, pp. S44-S49. [19] T. Hu, K. Ma, T.
- [43] S. Wisutmethangoon, S. Thongjan, N. Mahathaninwong, T. Plookphol, and J. Wannasin, *Mater. Sci. Eng. A*, 2012, vol. 532, pp. 610-615.
- [44] Aboulkhair, Nesma & Maskery, Ian & Tuck, Christopher & Ashcroft, Ian & M. Everitt, Nicola. (2016). The microstructure and mechanical properties of selectively laser melted AlSi10Mg: The effect of a conventional T6-like heat treatment. *Materials Science and Engineering: A*. 667. 10.1016/j.msea.2016.04.092.
- [45] N.T. Aboulkhair, C. Tuck, I. Ashcroft, I. Maskery, N.M. Everitt, *Metall Mater Trans A*, 46A (2015) 3337-3341.
- [46] K.G. Prashanth, S. Scudino, H.J. Klauss, K.B. Surreddi, L. Löber, Z. Wang, A.K. Chaubey, U. Kühn, J. Eckert, *Materials Science and Engineering: A*, 590 (2014) 153-160.
- [47] K. Kempen, L. Thijs, J. Van Humbeeck, J.P. Kruth, *Physics Procedia*, 39 (2012) 439-446.
- [48] W. Li, S. Li, J. Liu, A. Zhang, Y. Zhou, Q. Wei, C. Yan, Y. Shi, Effect of heat treatment on AlSi10Mg alloy fabricated by selective laser melting: Microstructure evolution, mechanical properties and fracture mechanism, *Materials Science and Engineering: A* 663 (2016) 116-125.
- [49] M. Simonelli, C. Tuck, N.T. Aboulkhair, I. Maskery, I. Ashcroft, R.D. Wildman, R. Hague, *Metall Mater Trans A*, 46A (2015) 3842-3851.
- [50] Charlie R. Brooks, A. Choudhury, *Failure analysis of engineering materials*, McGraw-Hill, United states of America, 2002.
- [51] Xianglong Yu, Lianfeng Wang, T6 heat-treated AlSi10Mg alloys additive-manufactured by selective laser melting, *Procedia Manufacturing*, Volume 15, 2018, Pages 1701-1707

- [52] M.M. Sistiaga, R. Mertens, B. Vrancken, X. Wang, B.V. Hooreweder, J. Kruth, J.V. Humbeeck, Changing the alloy composition of Al7075 for better processability by selective laser melting, *Journal of Materials Processing Technology*, 238 (2016) 437–445.
- [53] N. Takata, H. Kodaira, K. Sekizawa, A. Suzuki, M. Kobashi, Change in microstructure of selectively laser melted AlSi10Mg alloy with heat treatments, *Materials Science and Engineering: A*, 704 (2017) 218–228.
- [54] Burleigh, T David. "Corrosion of Aluminum and Its Alloys." Totten, G E, and D S MacKenzie. *Handbook of Aluminum, Vol. 2, Alloy Production and Materials Manufacturing*. New Mexico: New Mexico Institute of Mining and Technology, 2003. 421-463.
- [55] Cevik, E, Y Sun and H Ahlatci. "Effect of Peak-Aged Heat Treatment on Corrosion Behavior of the AA6063 Alloy Containing Al3Ti." *Archives of Metallurgy and Materials* (2012): 469-477.
- [56] Ahrari, Ali et al. "Multi-objective optimization of cellular scanning strategy in selective laser melting." 2017 IEEE Congress on Evolutionary Computation (CEC) (2017): 2730-2737.

### 3. Experimental Procedure

#### 3.1. Part fabrication

The part was fabricated by SLM 280 printer at CalRAM Inc. This machine is suitable for aluminum alloys, nickel, and titanium (specifications are provided in Table 3.1). Five AlSi10Mg cubic samples 1 cm<sup>3</sup> were produced from atomized powders using the SLM 280 printer with twin 400-watt lasers at CalRAM Inc. (Figs. 3.1 and 3.2). The AlSi10Mg test samples were built according to the default parameters of SLM 280. The process of printing was performed in an inert argon atmosphere to avoid oxidation in the samples. After printing, the samples were disassembled from the substrate using electron discharge machining (EDM).



**Figure 31 Selective Laser Melting machine (SLM200) [1].**

**Table 3.1 specification of SLM 200 [1]**

<b>Build Envelope Volume (x/y/z)</b>	280 x 280 x 365 mm
<b>IPG Fiber Laser Power</b>	Single: 400W or 700W Twin: 2x 400W or 2x 700W
<b>Build Rate</b>	88 ccm/h 400W Twin
<b>Layer Thickness</b>	20 – 75 $\mu\text{m}$
<b>Min. Feature Size</b>	150 $\mu\text{m}$
<b>Beam Focus Diameter</b>	80 – 115 $\mu\text{m}$
<b>Scan Speed</b>	10 m/s
<b>Inert Gas Consumption in Operation</b>	Ar/N <sub>2</sub> , 2.5 L/min
<b>Inert Gas Consumption Purging</b>	Ar/N <sub>2</sub> , 70 L/min
<b>E-Connection / Consumption</b>	400 Volt 3NPE, 63 A, 50/60 Hz, 3.5 5.5 KW
<b>Compressed Air Requirement</b>	ISO 8573-1:2010 [1:4:1], 50 l/min @ 6 bar
<b>Dimensions in mm (L x W x H)</b>	2600 x 1200 x 2700 mm

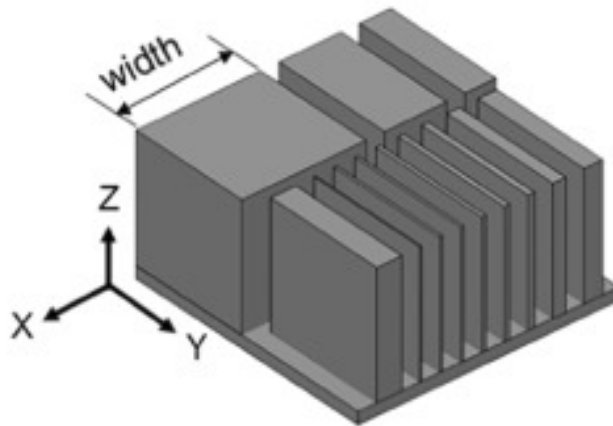


**Figure 32 Schematic of AlSi10Mg sample [2].**

### 3.2. Cutting

A cutting equipment known as Buehler- IsoMet low speed saw were used to cut the cubic samples in half through their z-plane (Fig. 3.3). Coolant is used to reduce the heating at the cutting location caused by the friction. The cutter is perfect for precision cutting processes. Since the low speed

saw does not produce much heat on the cutting location, the microstructure stands less chances of being altered. The machine' speed was set at 200-300 rpm and it used gravity fed force to cut.



**Figure 33 Buehler- IsoMet cutting machine [3].**

### **3.3. Heat treatment**

A separate set of as-printed samples were employed toward T<sub>6</sub> heat treatment (artificial aging). This includes solutionizing at 520 °C for 1 h, followed by water quenching, and the artificial ageing at 170 °C for 4 h. A separate set of samples (another three samples) were solution treated at 520 °C for 1 h followed by various cooling rate at different cooling media. This includes air cooling (AC) where the sample cooled down in the air, furnace cooling (FC) where the sample cooled down gradually inside the furnace and water quenching (WQ), see Fig. 3.4.

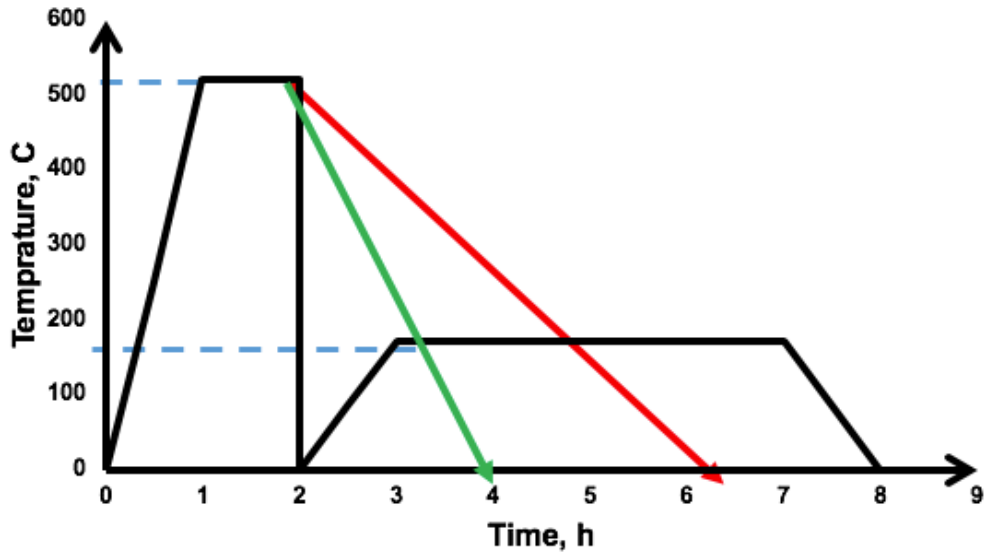


**Figure 34 Heat Treatment cycle diagram: black line represents artificial ageing, green represent air cooling and red represent furnace cooling.**

### 3.5. Mounting

By employing the Buehler metallurgical mounting – Simplimet 1000 equipment’s technique for hot mounting, the samples were mounted. A force of 29kN was subjected to the black phenolic resin, which was used a material for mounting. The heating and cooling time was 6 and 2 hours respectively, Fig. 3.5.

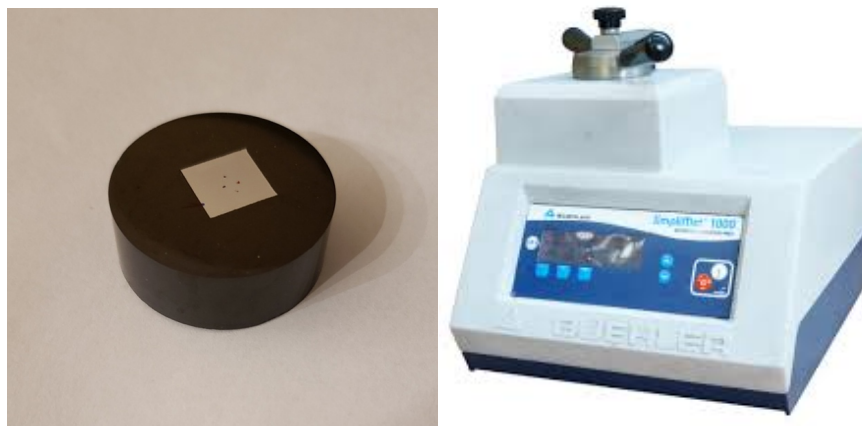


**Figure 35 A mounted AlSi10Mg sample (left), Simplimet 1000 machine (right) [4].**



### 3.6. Polishing

To prepare the samples for further microstructural assessments and the nanoindentation testing, the Struers- Knuth Rotor manual polisher was required for Fig. 3.6. Several steps were carried out in polishing of all the used samples. All the samples generated from the X, Y and inner Z plane were grounded using the Strueres SiC abrasive papers for grindings. These were 320 grits for a period of 10 minutes, 600 grits for a period of 10 minutes, 1000 grits for 10 minutes and 1200 for a period of 10 minutes, 600 grits for a period of 10 minutes, 1000 grits. More so, these were later polished using the 0.05  $\mu\text{m}$  AP-D suspension 5 minutes and then using the 0.25  $\mu\text{m}$  diamond suspension for another 5 minutes.



**Figure 36 Struers- Knuth Rotor polisher [5]**

### 3.7. Etching

As the final step in the metallographic preparation and to prepare the samples for the microstructure studies, an etchant solution should be applied in order to reveal the AlSi10Mg microstructure. To this end a Keller's reagent: 2.5%  $\text{HNO}_3$ , 1% HF, 1.5% HCl, 95% distilled water was used for 30 seconds.

### 3.8. Optical Microscopy

Upon polishing and etching, a metallurgical light microscope model MM 500T was used to observe the thin microstructures, Fig 3.7. These were observed using the lens magnification of 50X, 100X, 200X and 500X.

### 3.9. Scanning Electron Microscopy (SEM)

The microstructures were later observed using the SEM model FEI 650 FEG machine, Fig. 3.7. For the SEM observations, samples need to be prepared, mounted and grounded inside the machine. The session can start only when the pressure inside the machine is less than  $2 \times 10^{-5}$  Pa. The surface is usually focused, and then different images are taken at a desired location using the desired panel in front. It is advisable that the focus be taken at 3 times the magnification. An example is if we take an image using the 2000X magnification lens, it is therefore recommended that we take a focus of this image at 6000X and after zooming it out. A magnification of 500x-25000x were collected for all samples.



**Figure 37 Optical microscopic (left) and SEM (right) to capture the microstructure of the alloy [6].**

### 3.10. Nanoindentation

Mechanical properties were measured and observed using the Hysteron Triboindenter TI 750 nanoindentation machine, Fig. 3.8. A self-similar pyramidal Berkovich tip was employed to obtain the hardness and the Young's modulus, Fig. 3.9. This also shows the force/ displacement curves calculated using the various properties. The diagram indicates the schematics of the nanoindentation pattern where the Young's modulus was computed. While in this process, a trapezoidal shaped loading and unloading was applied with the maximum force of  $9500 \mu\text{N}$  as indicated in the diagram. While in this method, the loading force goes up to a constant  $9500 \mu\text{N}$  in a period of just 5 seconds. This holds for about 5 seconds holding and the unloading force goes back to zero within a period of 5 seconds as a constant rate, Fig. 3.10. Indentation load ( $P$ ), indentation depth ( $h$ ), and time are three main parameters that are recorded during the testing.



**Figure 38 Hysteron Triboindenter TI 750 [8].**

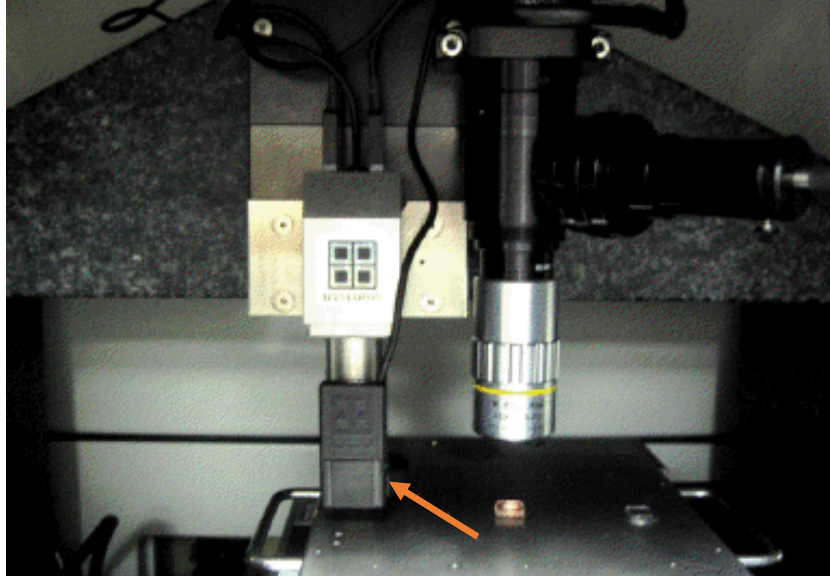


**Figure 39 Berkovich indenter tip [9].**

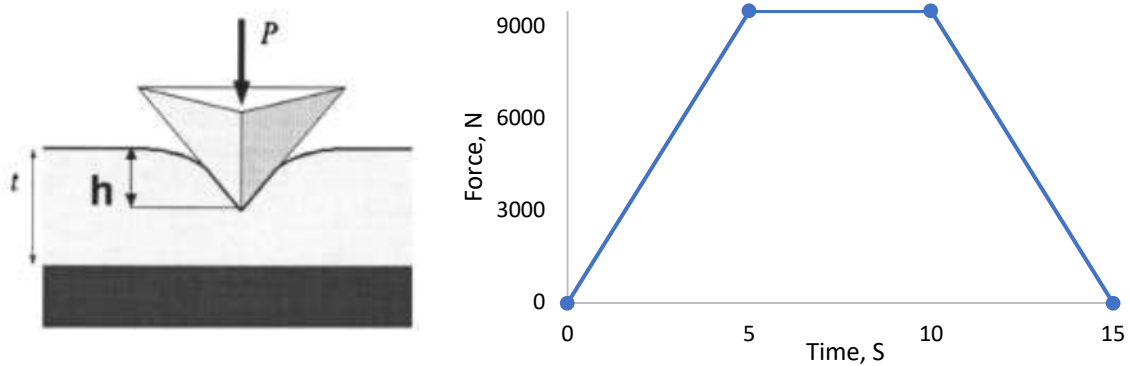


**Figure 40 Schematic of Berkovich indent apply  $F$  load on sample with  $h$  displacement (left) loading and unloading cycle (right).**

When all the calibrations are done, the actual tests were taken at center of each samples where the distances between these indents were observed to have an indent of  $5\mu\text{m}$  in both X and Y direction. Upon completion of the indents, the young' modulus plotted against the hardness is obtained from the load displacement curve. The derived young's modulus from the machines is reduced young's modulus constant which is a result of its deformation of the tip of itself. Data was calculated from

the different locations so that an average can be obtained and reduce on the margin of error. Reducing the margin error also increases the level of accuracy of the experiment hence the experimenter can easily draw conclusions about this data set.

### 3.11 References

- [1] "SLM 280." SLM Solutions, [slm-solutions.us/wp-content/uploads/2017/10/SLM280\\_NA\\_Web.pdf](http://slm-solutions.us/wp-content/uploads/2017/10/SLM280_NA_Web.pdf).
- [2] Naoki Takata, Hirohisa Kodaira, Asuka Suzuki, Makoto Kobashi, Size dependence of microstructure of AlSi10Mg alloy fabricated by selective laser melting, *Materials Characterization*, Volume 143, 2018, Pages 18-26, ISSN 1044-5803,
- [3] "IsoMet Low Speed Precision Cutter." Buehler, [www.buehler.com/isoMet-low-speed-cutter.php](http://www.buehler.com/isoMet-low-speed-cutter.php).
- [4] "Simplimet 1000." Buehler, [www.buehler.com/PDF/Service/SimpliMet-1000-PM-Package-Flyer.pdf](http://www.buehler.com/PDF/Service/SimpliMet-1000-PM-Package-Flyer.pdf).
- [5] "Struers-Knuth Rotor Manual Polisher." Geminibv, [www.geminibv.nl/labware-fr/struers-knuth-rotor-2-polijstmachine-de?set\\_language=de&pts\\_language=de](http://www.geminibv.nl/labware-fr/struers-knuth-rotor-2-polijstmachine-de?set_language=de&pts_language=de).
- [6] "EQ-MM500T-USB." MIT Corporation , [www.mtixtl.com/advancedmetallurgicalmicroscopewithpolarizingdarkfieldandduallights30mpdigitalcamera40x-1600x-eq-mm500t-usb.aspx](http://www.mtixtl.com/advancedmetallurgicalmicroscopewithpolarizingdarkfieldandduallights30mpdigitalcamera40x-1600x-eq-mm500t-usb.aspx).
- [7] "FEI Quanta 650 FEG SEM." The Thermo Scientific, [www.fei.com/products/sem/quanta-sem/](http://www.fei.com/products/sem/quanta-sem/).
- [8] "TI 750H Ubi." Irida , [irida.es/docs/catalogos/TI750H.pdf](http://irida.es/docs/catalogos/TI750H.pdf).
- [9] "Hysitron TriboIndenter Optics." Ebatco, [www.ebatco.com/laboratory-services/metallurgy/metallography/](http://www.ebatco.com/laboratory-services/metallurgy/metallography/).

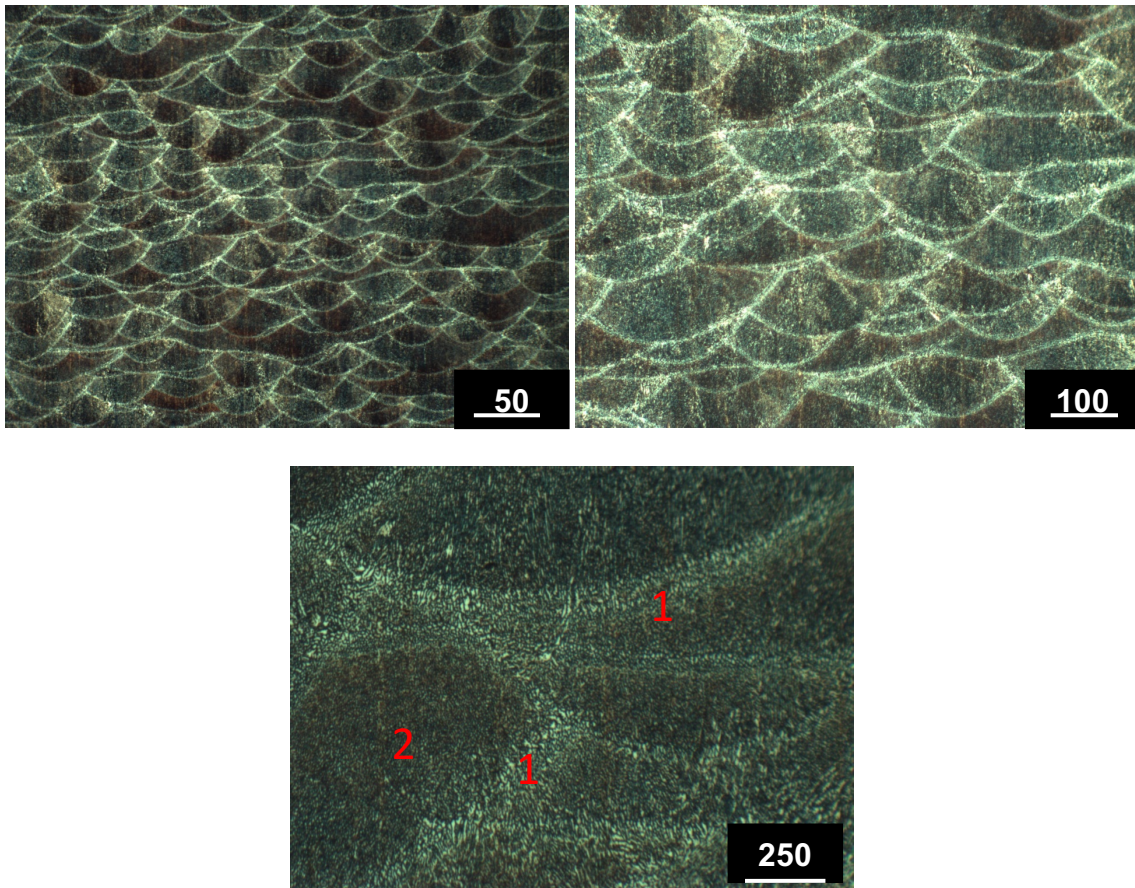
## Chapter 4: Results and Discussion

In this chapter, microstructure and mechanical analysis of Selective Laser Melting (SLM) AlSi10Mg is studied for the as-built and the heat treated samples through optical, scanning electron microscopy (OM, SEM) and the instrumented indentation testing techniques (Vickers, Nano-indentation). The goal of this project is to discover processing-structure relationship of the SLM process for AlSi10Mg cellular structures in the as-printed and heat treated conditions. Cellular structures fabricated by SLM have great potential for extreme loads due to high specific strength and stiffness. However, the product quality is often inconsistent due to complex geometry and manufacturing process. The key barriers include the lack of understanding of the physics involved in process and the inaccurate control of the process, leading to huge variations in microscale features and defects. The inability to understand the effects of uncertainties in material handling and properties also leads to a lack of consistency in the product quality.

It is worth mentioning that SLM could potentially manufacture parts with superior, tailored properties because of its high degree of local control over the microstructure of a manufactured part. In particular, cellular structures have many advantages, compared to their fully solid counterparts, including high specific strength and stiffness, high energy absorption, and low heat conductivity. However, the fabrication of cellular structures using conventional machining processes is often an impossible or at least extremely time-consuming task with many limitations. In this regard, SLM is an excellent solution for producing metal parts due to its superior capability of constructing complicated geometry.

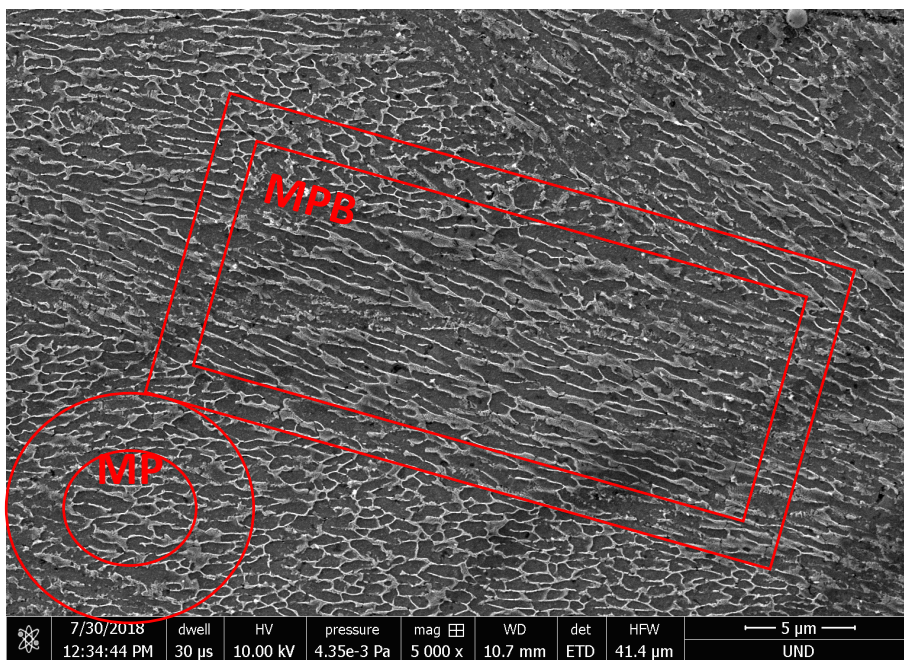
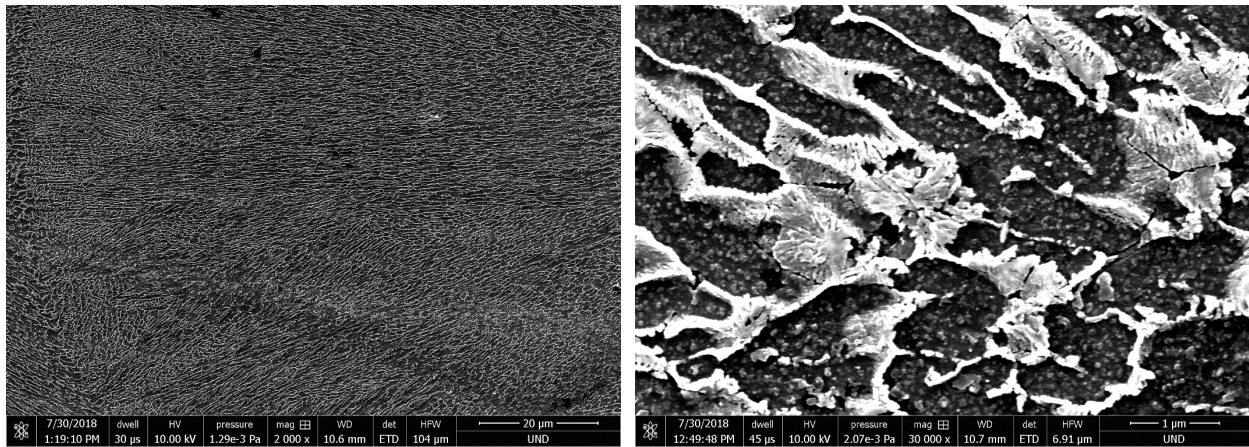
#### 4.1 Microstructural analysis

Fig. 4.1 shows the OM images of the as-printed (SLM) AlSi10Mg samples. The present microstructure is a result of the rapid solidification from SLM laser where the sample experienced fast cooling rate during the printing operation. Cellular microstructure characteristic observed in as-built sample where supersaturated Al matrix with continuous fibrous coral shape of eutectic Si particles of the SLM AlSi10Mg are existing in a half circular shape melt pools which coincide with local melting and rapidly solidifying regions.



**Figure 41 a) Optical microcopy images of as-built AlSi10Mg and b) shows half circular shape grain at different magnification c) a close look at the grain where “1” is melt pool and “2” melt pool boundary**





**Figure 42 SEM images of as-built sample a) cellular like shape microstructure with Al as matrix, b) a higher magnification shows Si in different orientation “1” elongated and “2” equiaxed, c) shows elongated Si at melt pool boundary “MPB” and equiaxed in melt pool “MP”.**

The breakdown of the microstructure, employing the SEM, shows that it is distinguished into layers see Fig 4.2. There are sections known as the melt pools that are divided into three regions. These are:

- the heat affected zone (HAZ)
- the melt pool boundary
- the melt pool core

Due to the SLM “layer by layer” manufacturing nature, the microstructures are often non-homogenous. The Al cells usually appear equiaxed towards the melt pool core when viewed perpendicular to the build direction. When viewed parallel to the build direction, the Al cells at the melt pool boundaries appear elongated.

The microstructure changes dramatically after heat treatment, Figs. 4.3 & 4.4 show a comparison between the SLM AlSi10Mg microstructures before and after heat treatment (heat treatment cycles were explained in Chapter 4 of this thesis). The interconnected fibrous coral shape of silicon transform into spherical shape silicon particles which are uniformly distributed throughout the Al matrix with different shape and size. Fig. 4.3 shows the SEM micrographs of the as-printed and the various heat treated samples (AC, FC, WQ and Aged). Comparing Fig. 4.2a, the as-built, with 5.4a, the artificially aged, it is unambiguous that Si particles in the aged sample become larger, spaced more uniformly spread because of coalescence and Ostwald ripening.

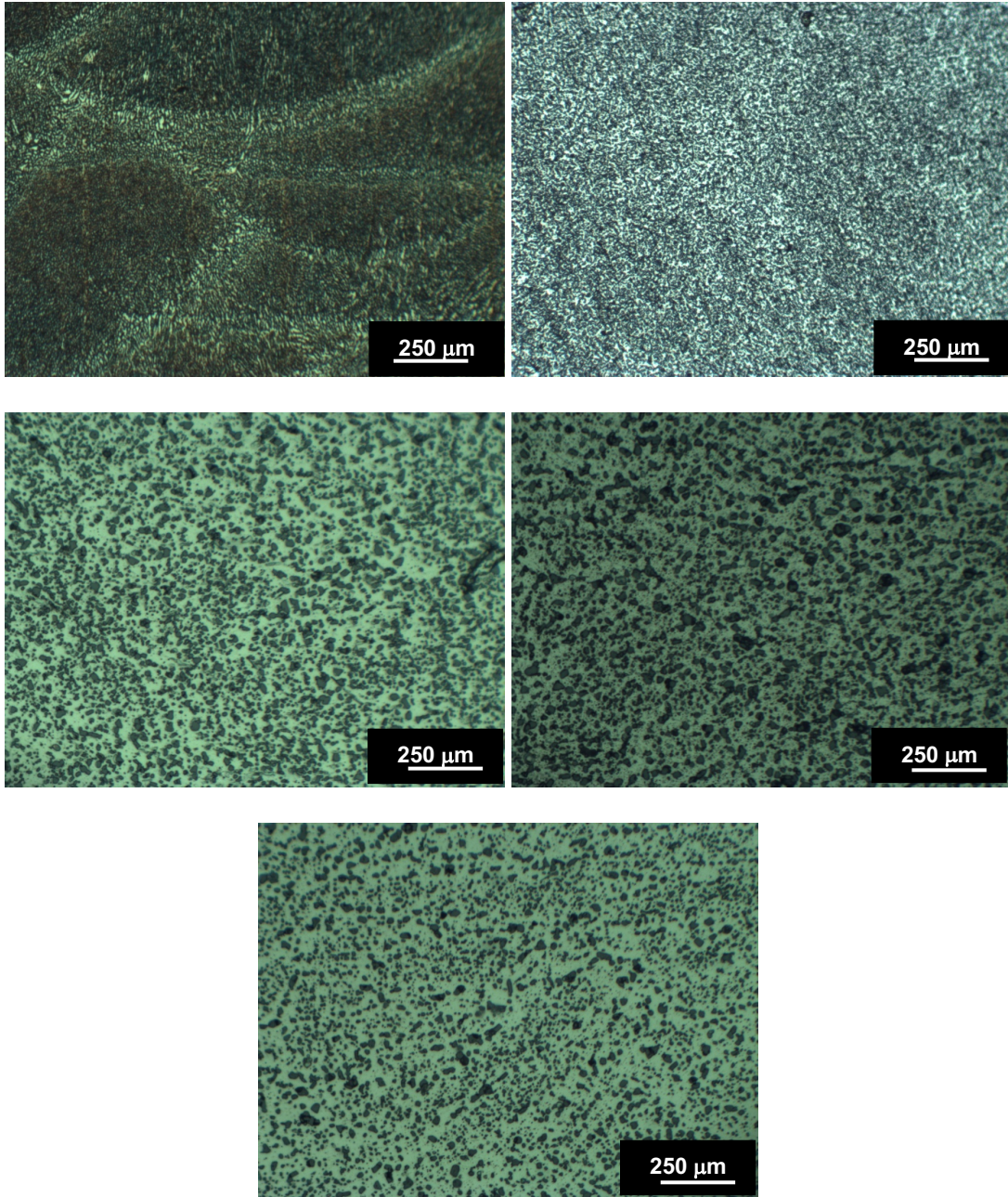
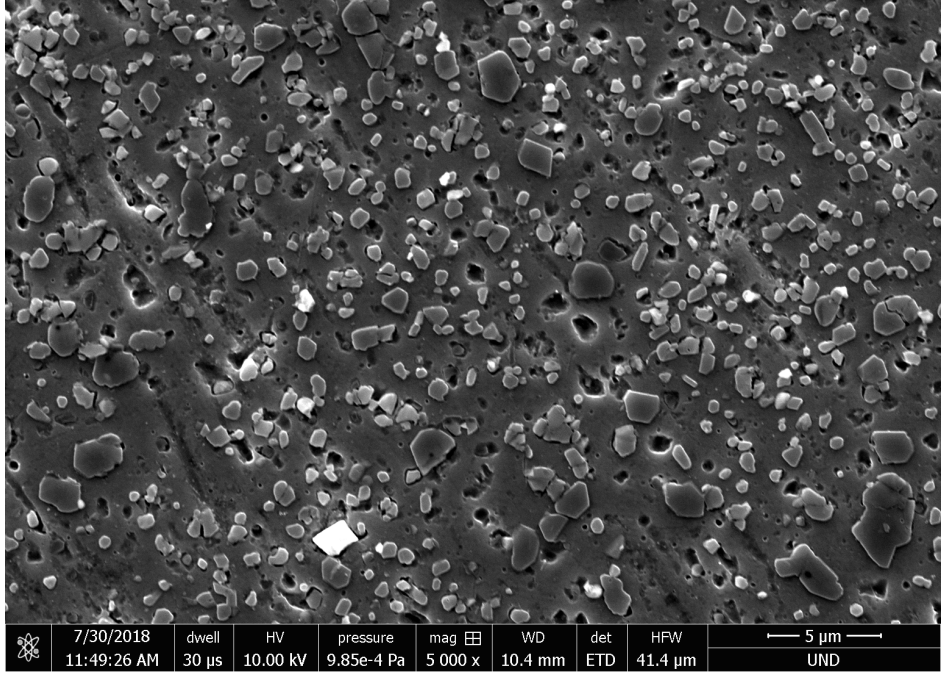
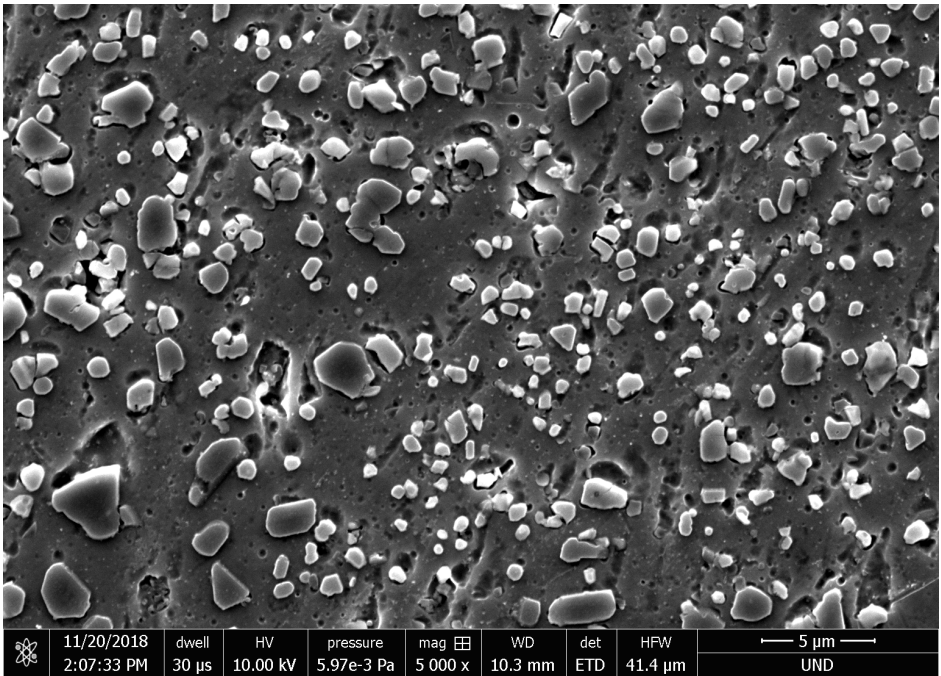


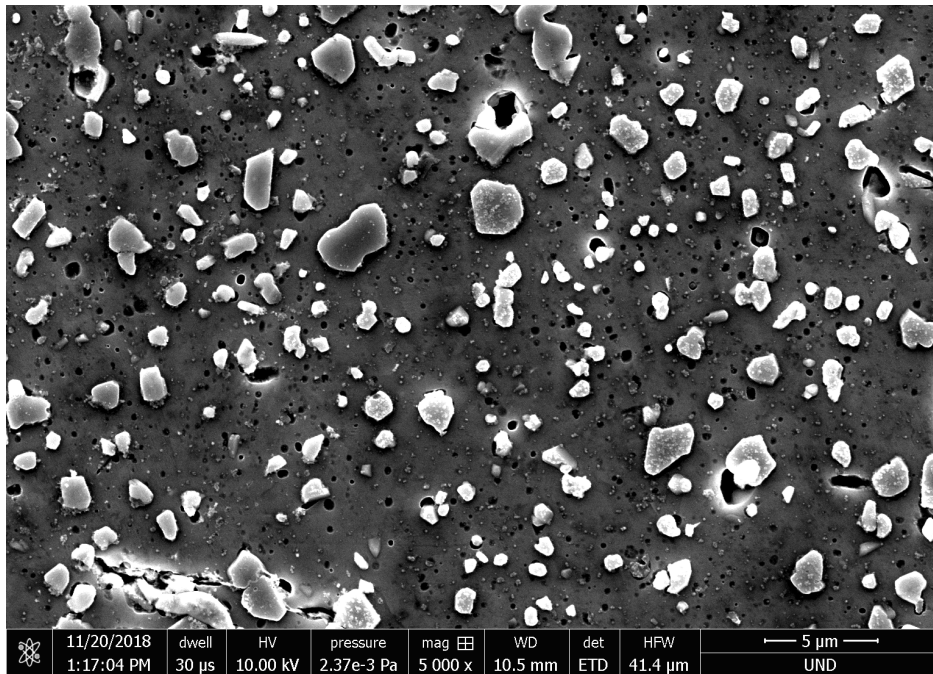
**Figure 43 Side by side OM comparison of a) as-built, b) artificially aged, c) WQ, d) AC, e) FC samples.**



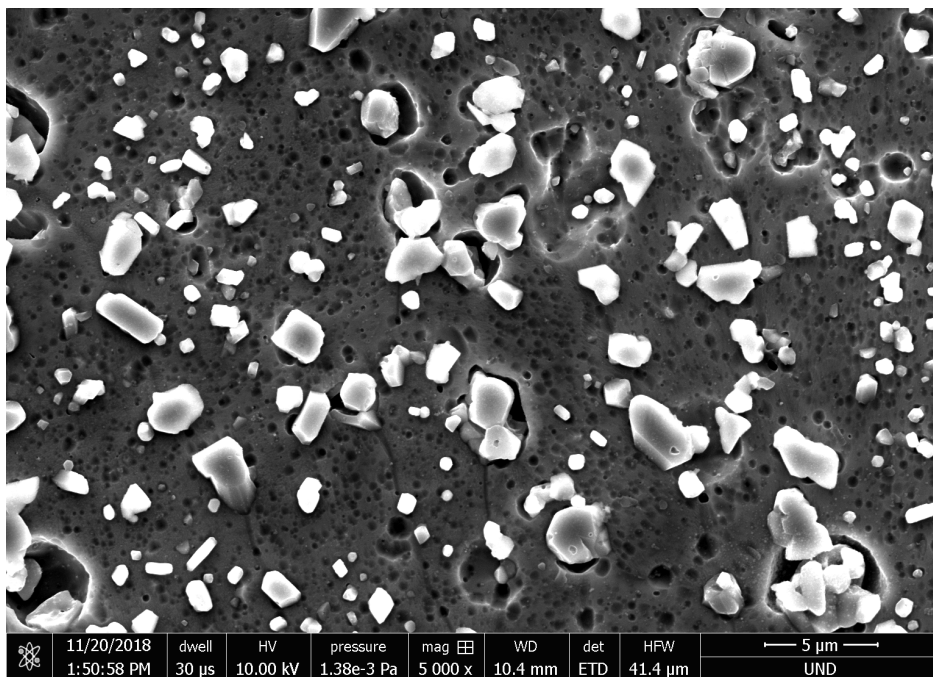
a



b



c



d

**Figure 44 SEM micrographs the AlSi10Mg when a) artificially aged, b) WQ, c) AC, d) FC.**

Ostwald ripening is a phenomenon where large particle grows at the cost of collective small particles. It is a spontaneous process that reduces internal energy of a system thermodynamically [1]. Small particles possess large surface-to-volume ratio that results in high internal energy of the system because of large surface energy. However, when particles grow, this internal energy reduces as surface-to-volume ratio becomes smaller. Having said this, smaller particles on the surface tend to disengage themselves and migrate (diffuse) to the surface of coarser particles. In Fig. 4.4, a clear gradually decreasing trend can be observed from aged, WQ, AC to FC samples respectively, where the artificially aged sample microstructure shows large number of Si particles spread throughout the matrix; on the other hand, the FC sample shows small number of coarsened Si particles. The coarsening phenomenon of the Si particles is a diffusion based process and diffusion is a time and temperature dependent phenomenon. That is, with providing time and temperature the diffusion process is expedited. Here the rate of cooling the FC sample is the slowest which mean that sufficient time is available for the Ostwald ripening to occurs as compared with the AC sample where there is literally no time for the Ostwald ripening phenomenon to be effective. Since Si coarsening is directly related to the cooling rate and it is obvious that  $WQ_{cooling\ rate} > AC_{cooling\ rate} > FC_{cooling\ rate}$ , therefore, the Si particle coarsening is greatest in the FC condition and the least in the WQ conditions.

The Si particle size for the as-built sample cannot be quantified since it is placed at the boundary with no particular shape. However, the average particle size of Si for the heat treated samples particles were measured between 0.7 and 1  $\mu\text{m}$ . According to Aboulkhair et al [2] particles would start to form at solution heat treatment, and this is not completed until beyond 6 hours of ageing that the particles size start to increase. Moreover, according to Li et al [3] at artificial ageing time of 12 h, the Si particles can grow to a size up to 5  $\mu\text{m}$ . This increasing in the Si particles size

indicate that in the as-built sample, the Al matrix is supersaturated and during the heat treatment excessive Si particles would precipitate throughout the matrix. To grasp the effect of heat treatment on the Si morphology better, the modification mechanisms of these eutectic collection need to be understood. During solution heat treatment, eutectic Si particles are evicted for the Al matrix in the supersaturated state, Fig 4.5. This results in the segregation of Si particles all along the grain boundaries with coral like eutectic Si fibers [3, 4–6]. Si fibers are fragmented, therefore Si spheroidization is driven through surface self-diffusion where the element changes the location by diffusing on the surface [7] or Al–Si inter-diffusion at Si/Al interface where the silicon atoms move through the aluminum at the interface.

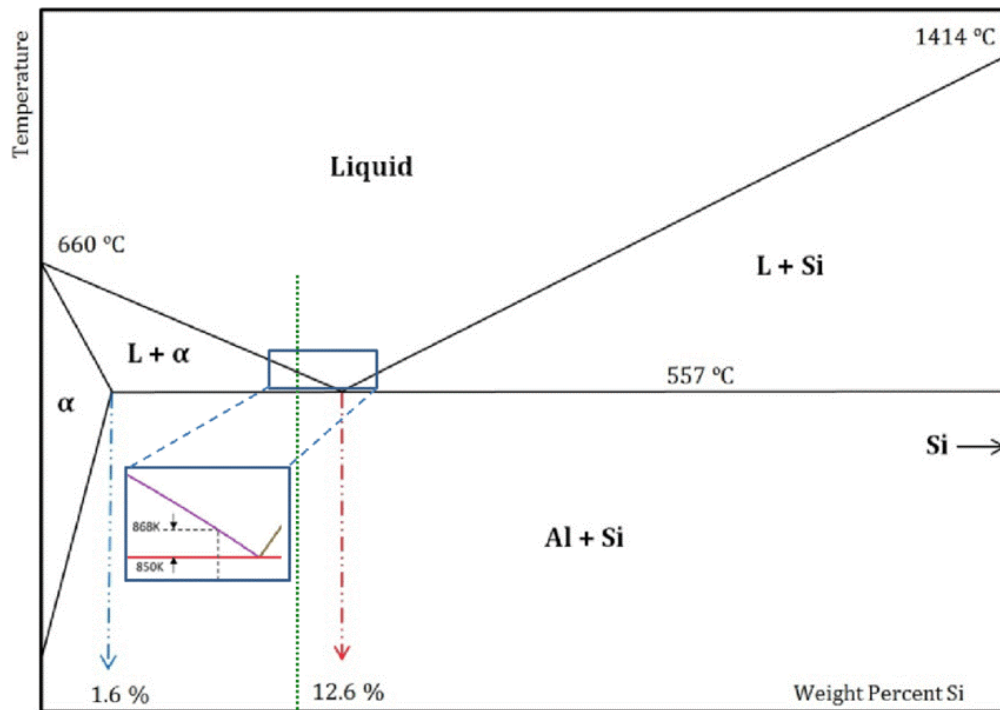


**Figure 45 Al-Si phase diagram shows the region of elevated temperature of heat treatment solution that is below eutectic temperature around 10% of Si [8]**

The energy from the Si/Al interface diffusion is more promising, where the chemical potential gradient between the interfacial discontinuities and the adjacent area provides the required energy

from the solid-state atomic diffusion and therefore morphological evolution (spheroidization), see Fig. 4.6. Considering the solid-state atomic diffusion as a time and temperature dependent phenomenon, a heat treatment cycle at an elevated temperature but below eutectic temperature could be an efficient technique to change the shape and morphology of the Si. Upon providing sufficient time and temperature particle coarsening occurs to reduce the overall energy of the system. That is, the particles become coarse as the aspect ratio reduces leading to loss of the interconnection of the eutectic phases. Temperature and the duration of exposure determine the rate at which interconnectivity is lost.



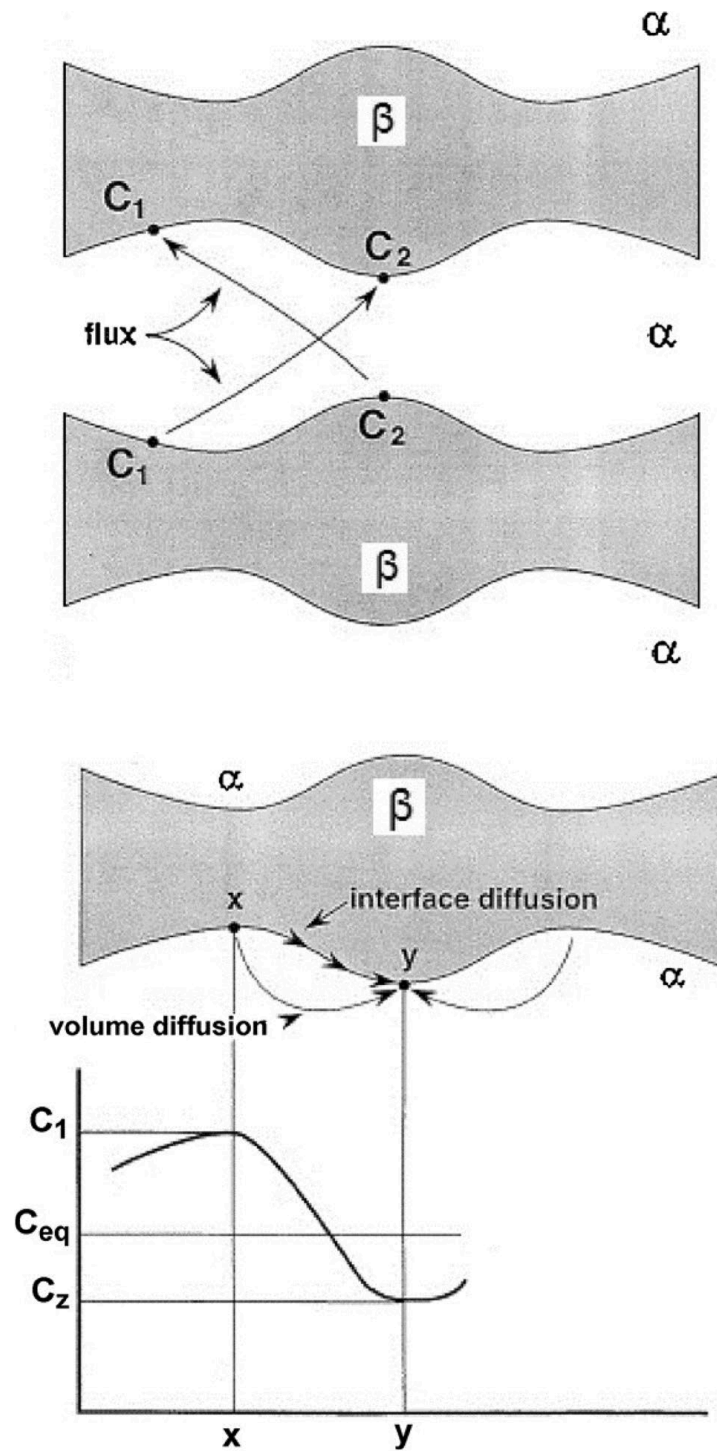
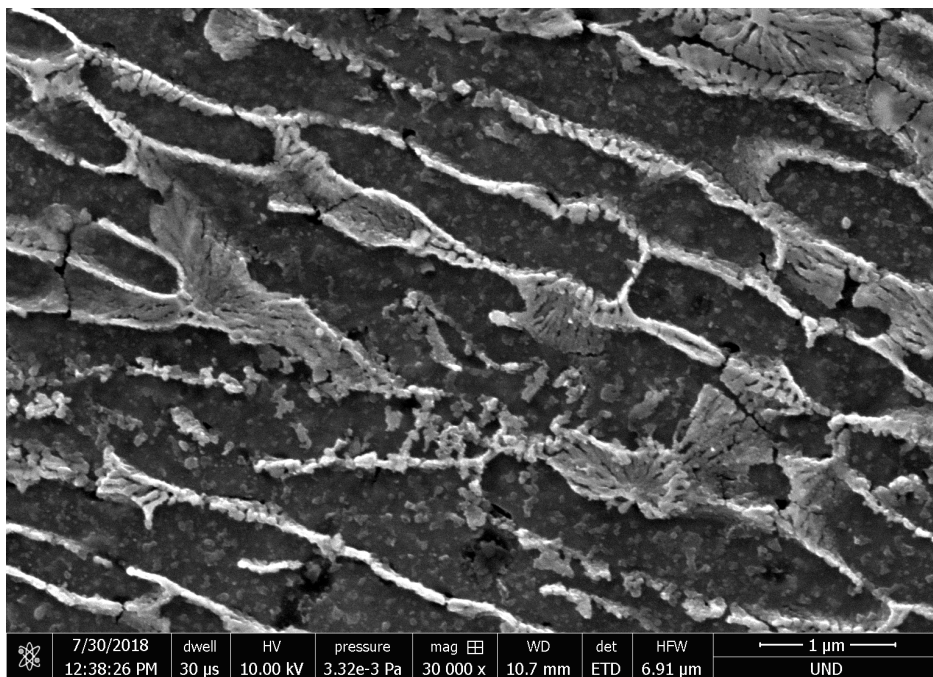


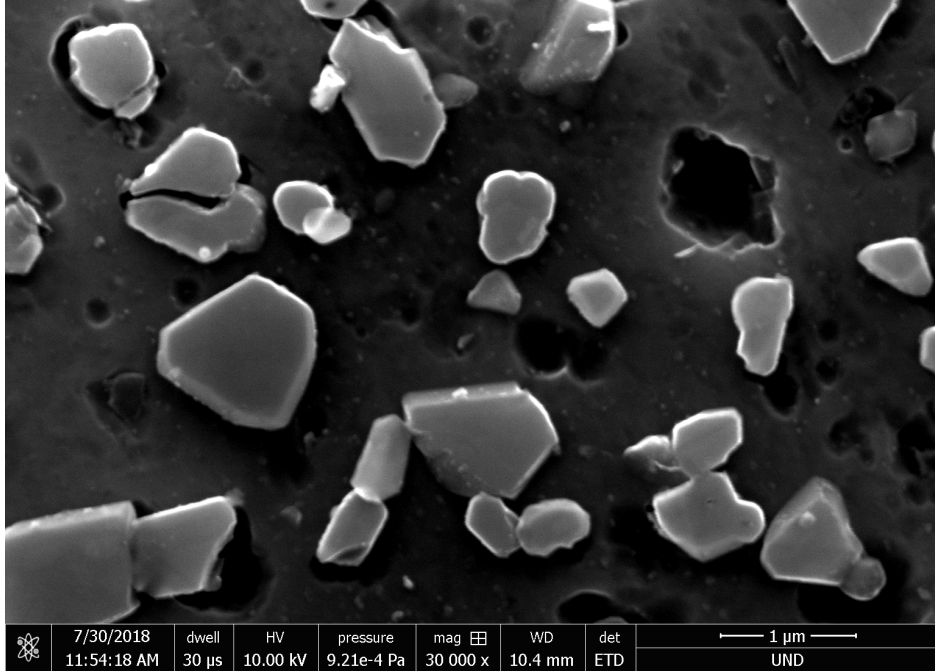
Figure 46 The schematic representation of volume and interface diffusion resulting in the Si fragmentation and spheroidization [9, 10]

Fig. 4.7 shows the Si morphology in the as-printed and the heat treated microstructures. Si spheroidization phenomenon and Si coarsening are clearly observed here.

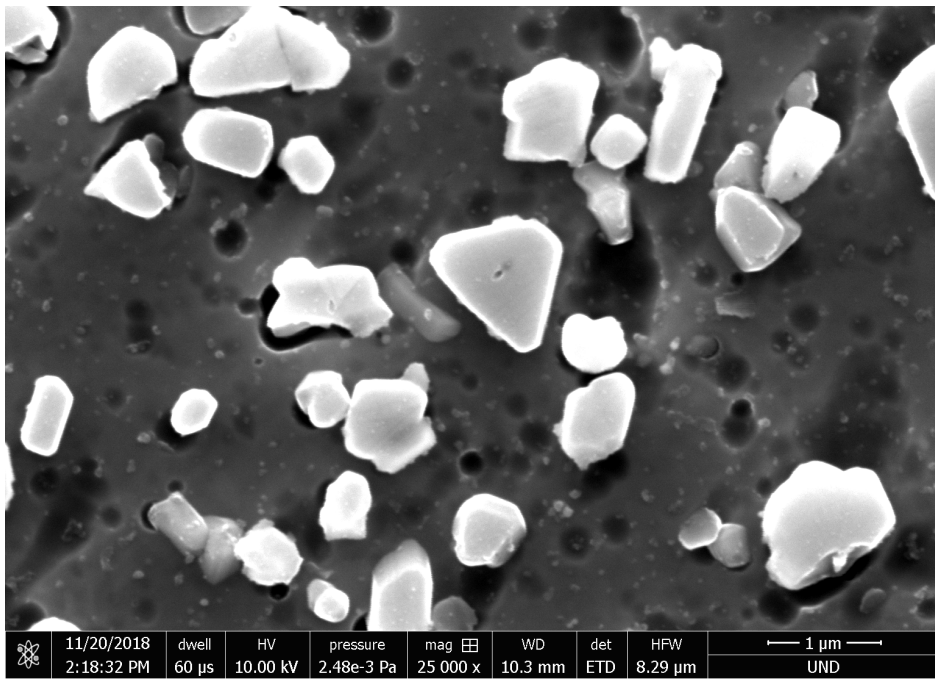
- Artificially aged: spread small coarsened Si particles presented
- WQ: small Si particles.
- AC: larger Si particle
- FC: largest Si particles with nucleation sites on top of Si.



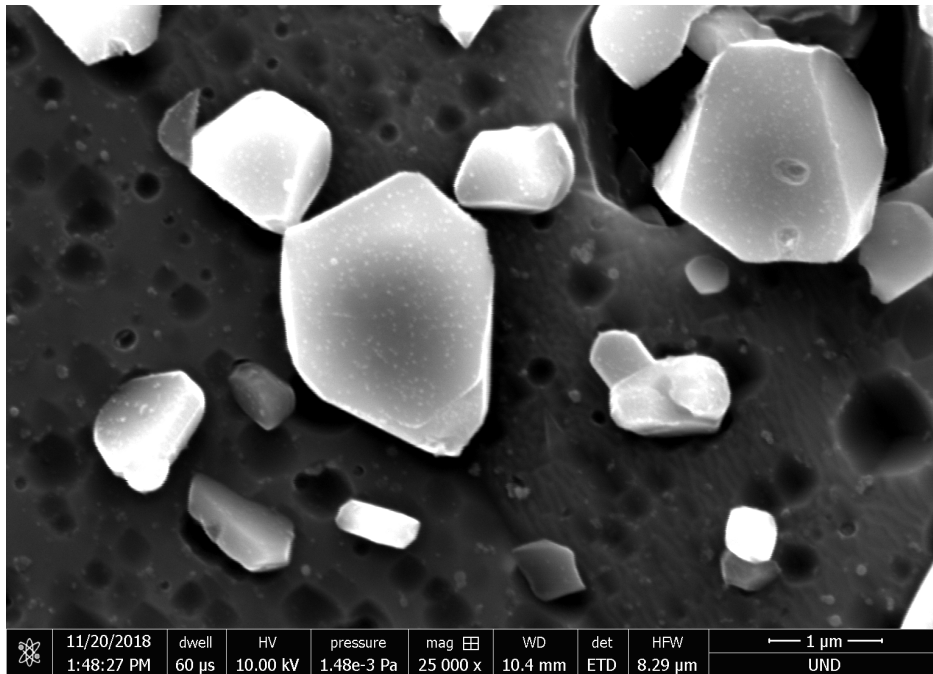
a



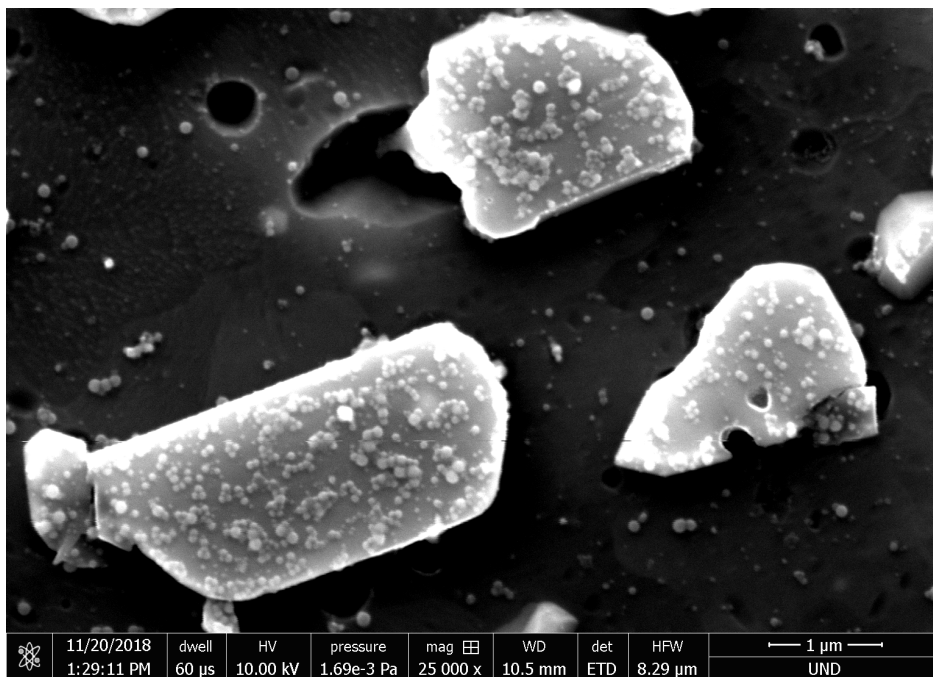
b



c



d



d

**Figure 47** The SEM micrographs of a) as-built AlSi10Mg, b) aged, c) WQ, d) AC, e) FC samples. The change in the morphology of the eutectic Si is clearly observed.

## 4.2. Mechanical properties

Qualifying parts produced by the SLM process (or any other AM process) for real-world applications is a major challenge, as the existing ASTM test standards cannot capture the fine variations in the material properties of SLM produced parts. Therefore, in the present project, the mechanical properties of the as printed and heat treated materials will be achieved mainly using a depth-sensing nanoindentation testing approach which is capable of estimating a variety of material properties through non-destructive testing. The baseline mechanical properties to be measured include strength (nano-hardness) and stiffness (Young's modulus).

Nanoindentation tests were performed at a constant load of 9.5 mN. Figs. 4.8 provides the load/ displacement curves of the tested materials under a constant load of 9.5 mN. A significant softening is observed in the heat treated samples (aged, WQ, AC and FC) as compared to the as-built AlSi10Mg alloy. That is, the indenter displacement within the material is less in the as the printed sample as compared with other heat treated samples. This softening can be directly attributed to the change in the morphology of the Eutectic-Si particles upon various heat treatments. The heat treatment causes the eutectic Si fibers to convert to spherical shape particles through a diffusion based spheroidization phenomenon. The spheroidization occurs when the temperature of the alloy is held below the eutectic temperature which is provided through heat during the heat treatment cycle. The Si particles assume a spheroidal shape and then is spread evenly through the alloy. Through the spheroidization phenomenon, the contribution of the Si particles toward strengthening of the alloy, as compared with the Eutectic Si-fibers, is reduced tangibly. The strengthening of the Si precipitates at melt pool boundary are eliminated upon the heat treatment. The reduction in hardness results to an increase in the ductility of the AlSi10Mg

alloy, in which the spherical Si particles allow the alloy to deform plastically which in turn increases the machinability and ductility of the alloy.

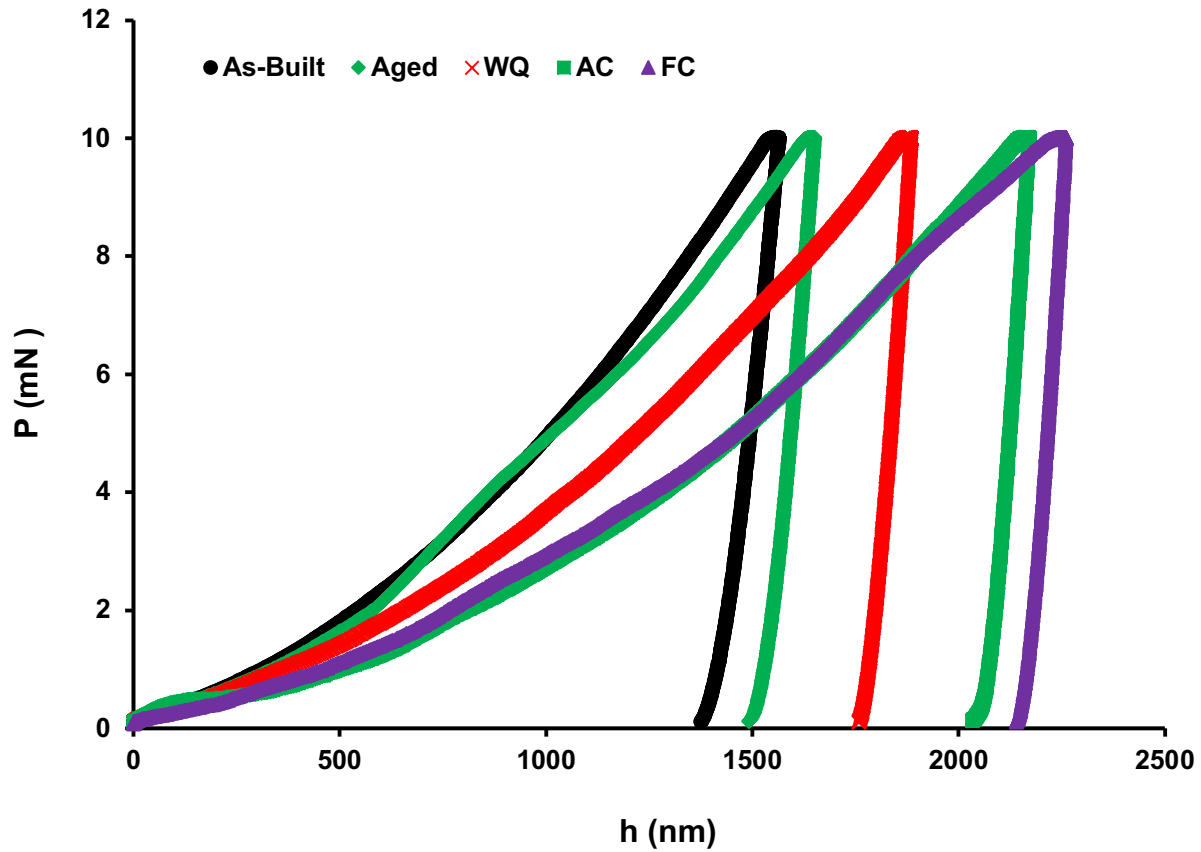
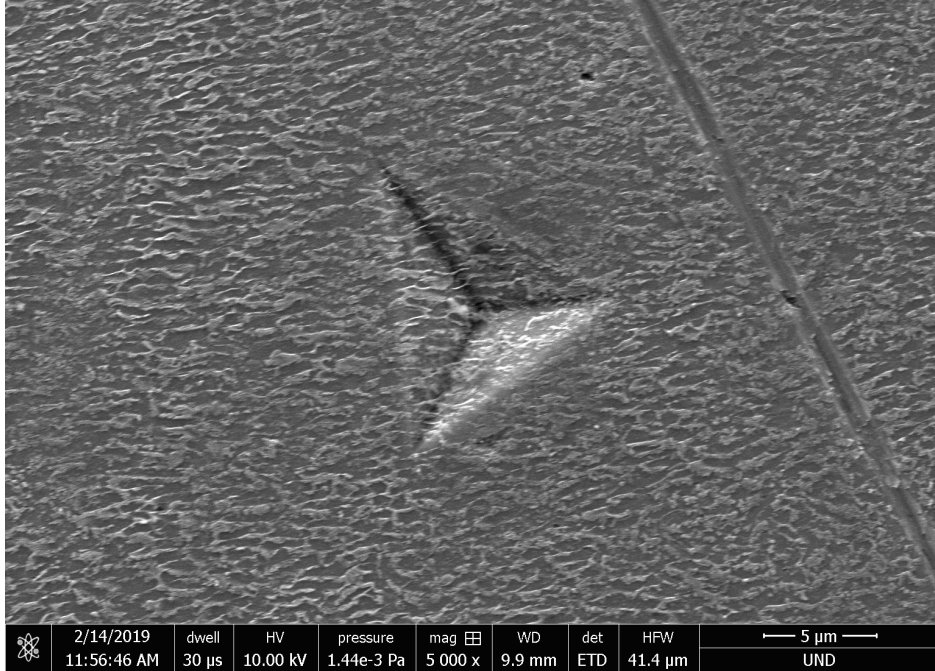
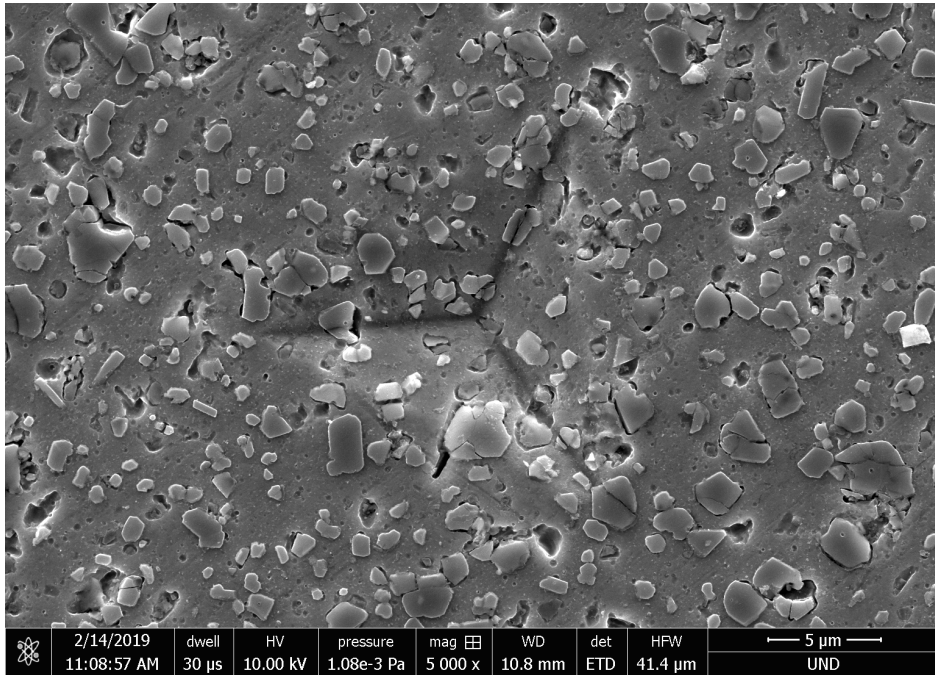


**Figure 48 Load vs displacement curves of the AlSi10Mg samples, as built and heat treated materials.**

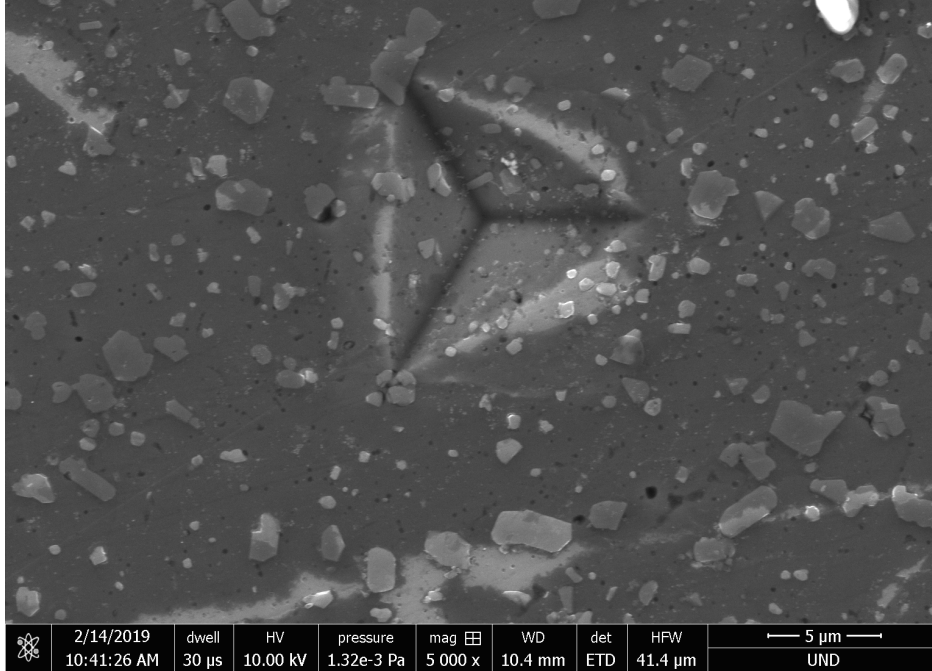
Fig. 4.9 shows the SEM micrographs of the actual indents made on various specimens including as-printed and the heat treated materials. It is clear that the size of the indents become bigger when the rate of cooling decreases which confirm the softening phenomenon occurring due to the heat treatment cycles.



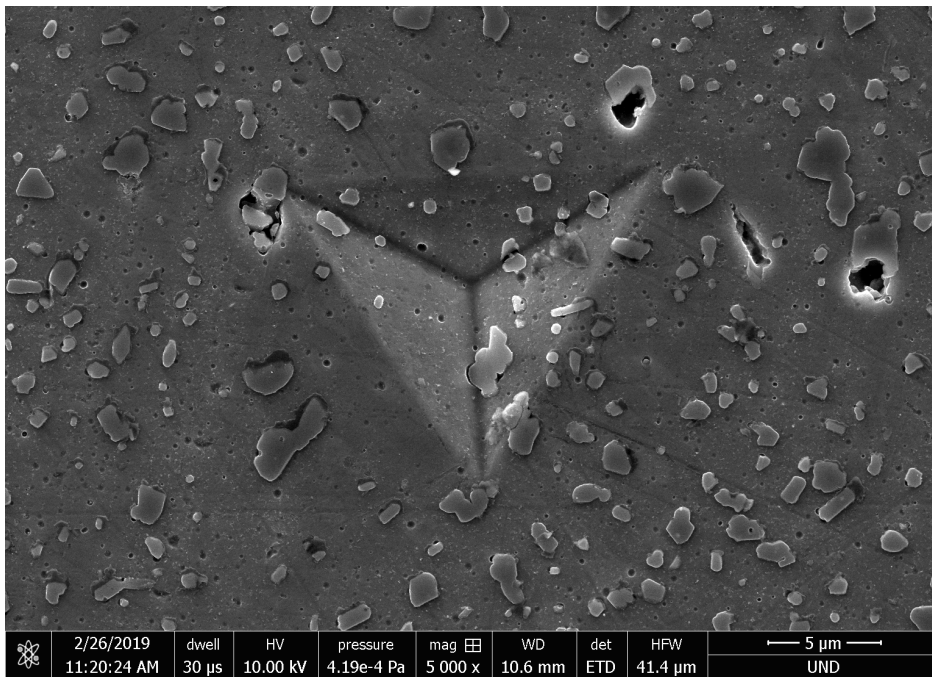
a



b

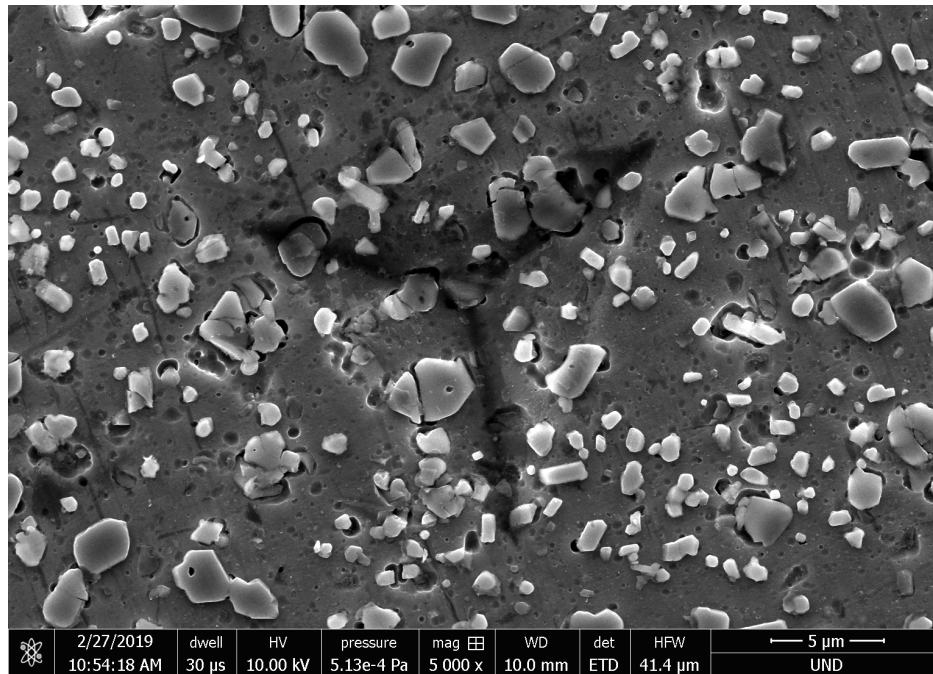


c



d





e

**Figure 49 SEM micrographs of the indentation images a) as-built, b) Artificially aged, c) WQ, d) AC, e) FC.**

From the load/displacement curves, the hardness value results expected to be highest in the as-built samples and lowest in FC sample. In Fig. 4.10 the hardness values of each samples are observed. The average hardness values are measured as  $1.90 \pm 0.11$  GPa,  $1.55 \pm 0.05$  GPa,  $1.13 \pm 0.04$  GPa,  $0.92 \pm 0.04$  GPa, and FC  $0.78 \pm 0.02$  GPa, for the as-built, the artificially aged, the WQ, the AC, and the FC, respectively.

It is worth mentioning that each provided hardness number is an average of six hardness values, however, to make the actual hardness values visible and not to make the hardness graphs busy and unreadable the error bars have not been provided. Important to note that the hardness value shows a uniform results across the microstructure of all samples because of the spread of spherical Si particles. Since the Al solution (matrix) is softer than the Si fibers, if the hardness was to be taken in the primary Al phase as compared with the eutectic Al-Si phase, it would show a

lower hardness. From results a sharp drop in hardness is observed and that is due to the softening induced by the Si-spheroidization.

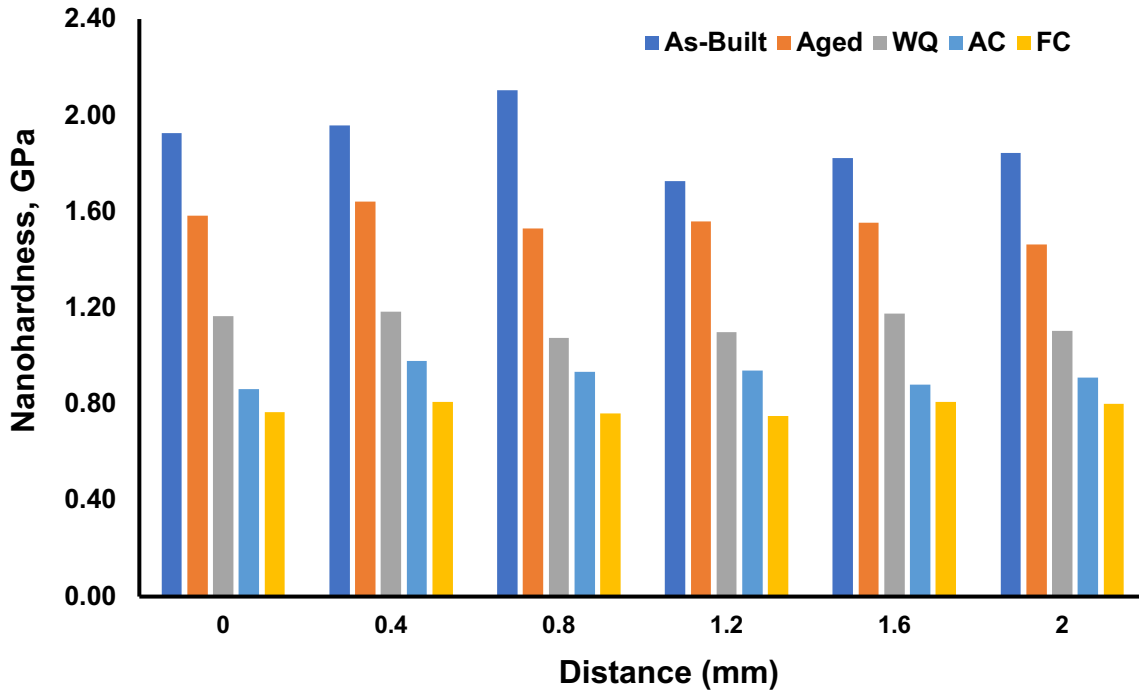


**Figure 4.10 Load vs displacement curves of the AlSi10Mg samples, as built and heat treated materials.**

The difference in hardness between all samples is affected by the thermal gradient of the heat treatment process. The hardness values in the as-built is higher than the all the other ones, and it is mainly attributed to that the aged, WQ, AC and FC being exposed to more of a thermal cycle than the as-built and thus more precipitation distribution in those four samples are seen than the as-built.

To confirm the results from the nanoindentation “localized” approach and to find the hardness over a larger area, Vickers hardness test was utilized and the result in Fig. 5.11. The average hardness values are measured as  $116.6 \pm 3.3$  HV,  $91.6 \pm 2.4$  HV,  $72.7 \pm 2.3$  HV,  $57.3 \pm 3.9$  HV

and  $43.9 \pm 3.7$  HV, for the as-built sample, the artificially aged, the WQ, the AC, and the FC, respectively (each provided hardness number is an average of six hardness values). The result provided the same trend where the hardness value drops gradually from as-built sample to FC, highest to lowest respectively.

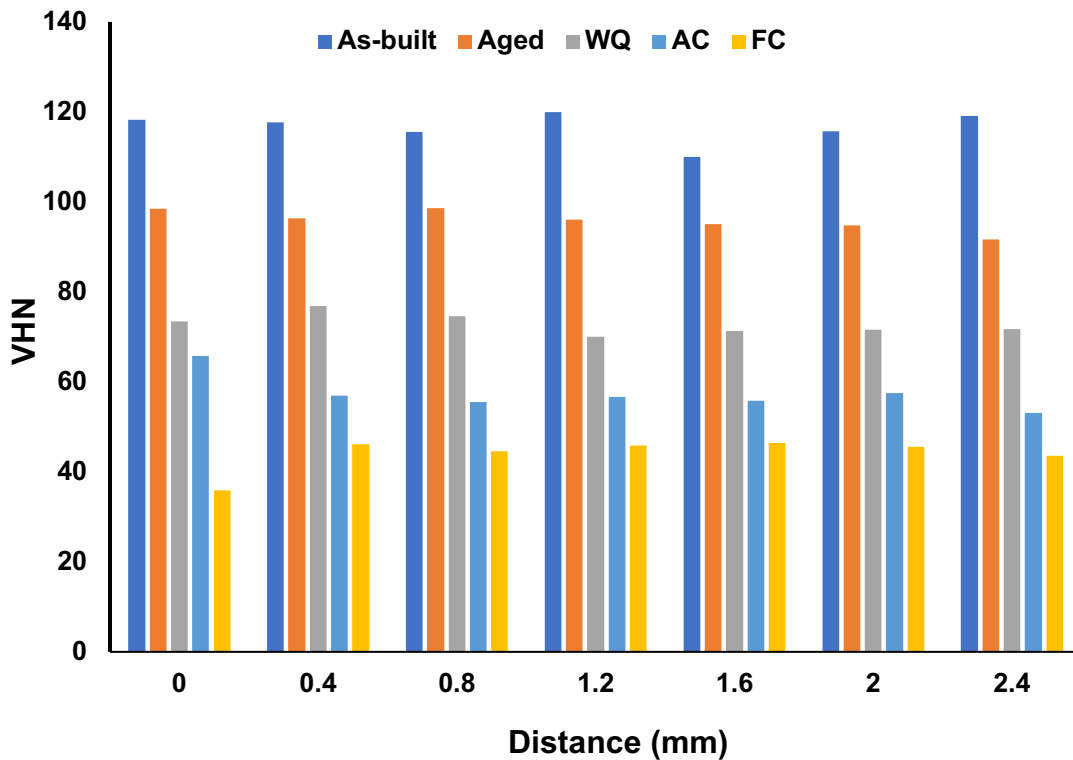


**Figure 50 Vickers hardness measures of the as-built and heat treated AlSi10Mg materials.**

### 4.3. As-built vs artificially aged

The most common heat treatment process on the Al-Si alloys is the T6 (artificial aging). Therefore, further investigation was conducted and the results compared to as-built sample. The results of both nano-indentation and Vickers tests show the same trend as previously stated in Figs. 5.10 and 5.11. The result extracted from these two tests were conducted on the XY and YZ plane, see Fig 5.12.

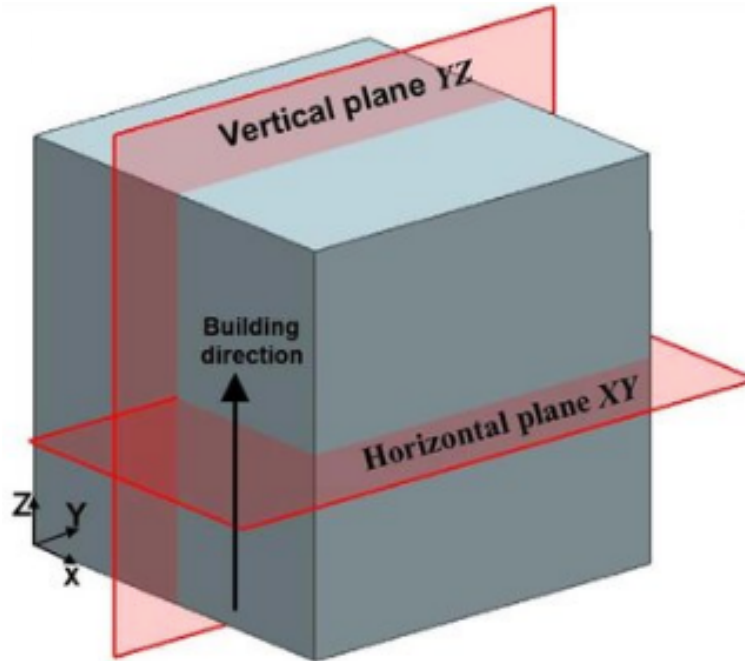


**Figure 51** Schematic of AlSi10Mg XY and YZ planes.

There is a clear change in the hardness values of the artificially aged alloy is observed; As seen in Fig. 5.13, the average nano-hardness value on the YZ plane for the as-built materials is measured as  $2.71 \pm 0.12$  GPa whereas the heat treated one shows  $1.56 \pm 0.11$  GPa. This confirms 42% decrease in the strength upon heat treatment. On other hand, the average nano-hardness on XY for the as-printed and the heat treated materials is  $2.58 \pm 0.12$  GPa and  $1.59 \pm 0.11$  GPa, respectively (38% decrease in strength); each provided hardness number is an average of 25 hardness values.

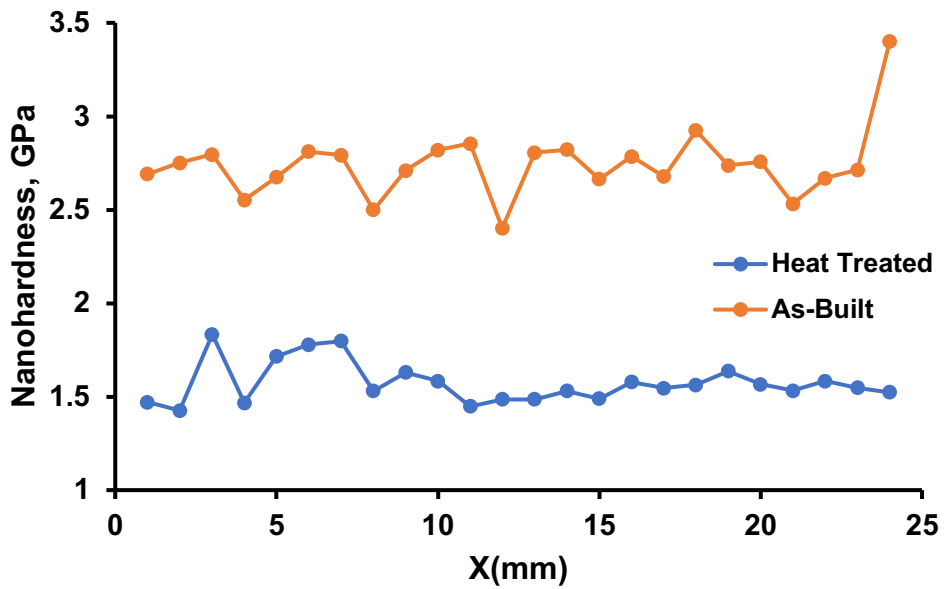
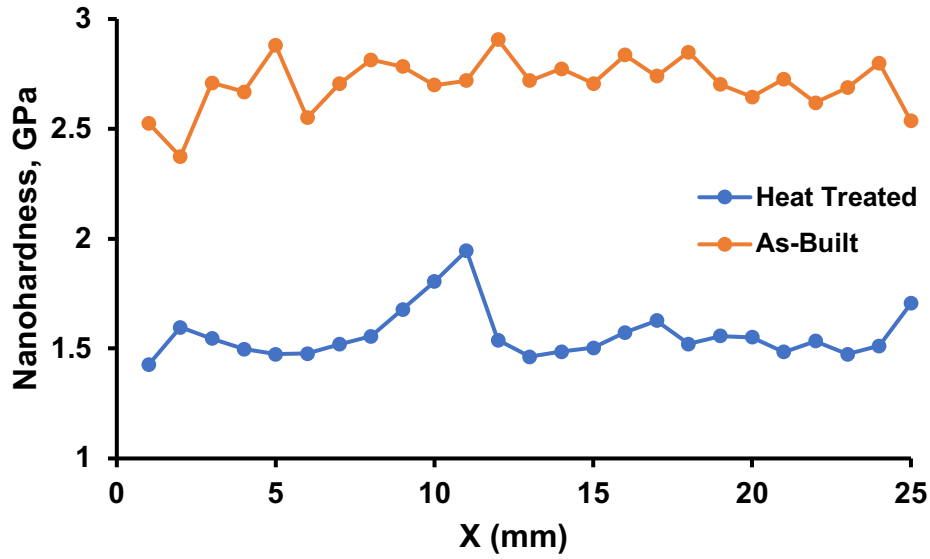
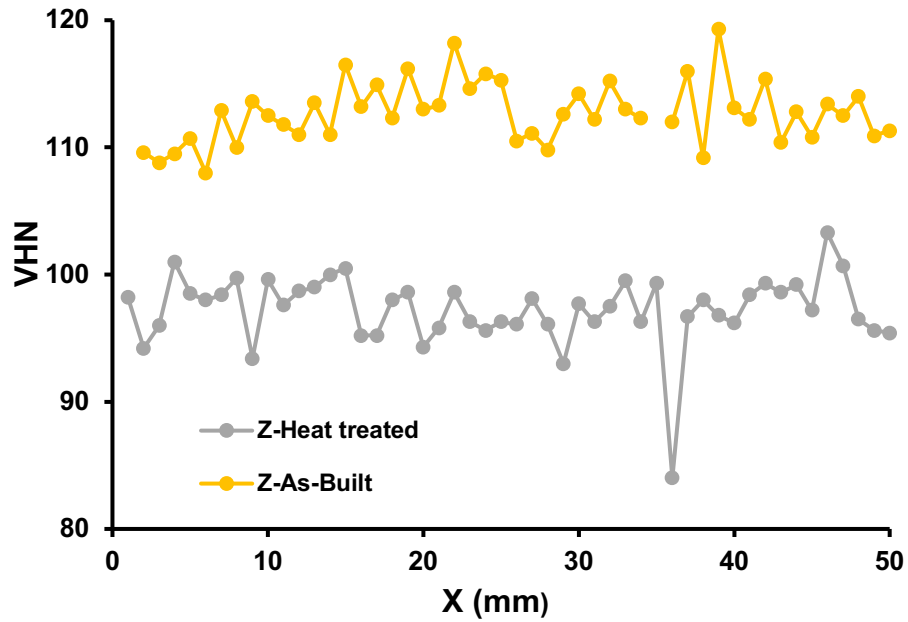


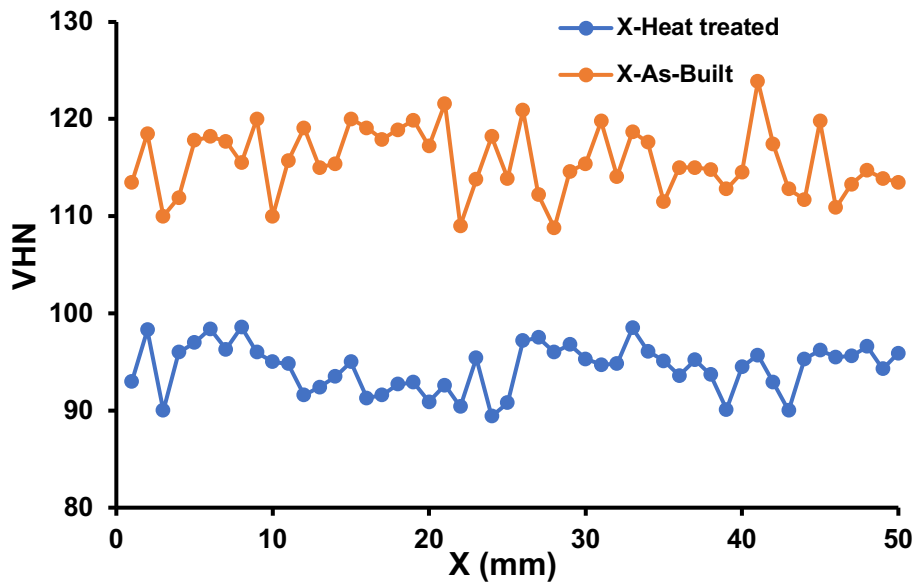
**Figure 52 Nano-hardness results for the AlSi10Mg samples, a) YZ plane, b) XY plane (heat treated: artificial aged).**

These results were confirmed upon performing Vickers hardness tests, see Fig 5.14; the average Vickers hardness value on the YZ plane for the as-built and the heat treated materials is  $115.7 \pm 3.5$  and  $97.3 \pm 2.8$ , respectively. The average Vickers hardness value on the XY plane for

the as-built and the heat treated materials is  $112.7 \pm 2.4$  and  $94.4 \pm 2.84$ , respectively; each provided hardness number is an average of 50 hardness values.



a



b

Figure 53 Nano-hardness results for the AlSi10Mg, a) YZ plane, b) XY plane.

As-built SLM AlSi10Mg tend to form anisotropy where the mechanical properties of one direction on the sample is different than the other direction. From the results, it is clear that the average nano-hardness values for as-built on both planes does not necessarily match; this is due to the layer by layer nature of the SLM which results in a complex cooling gradient. Yet the heat treatment dissolves formation of anisotropy in the microstructure thus improve the ductility and that is observed from the average nano-hardness value of heat treated on both planes where they match.

Indentation size effect (ISE) is the change of mechanical properties observed by indentation where reduction of the indent size leads to an increase in the hardness and a decrease in the plasticity deformation through indentation [12, 13]. Through the following equation, one can expect that indentation hardness (stress) is a depth dependent phenomenon:

$$\sigma_{\text{ind}} = \frac{P}{24.56 * (h_{\text{ind}} + 0.06R)^2} \quad (4.1)$$

where  $R$  is Berkovich tip radius equal to 100 nm.

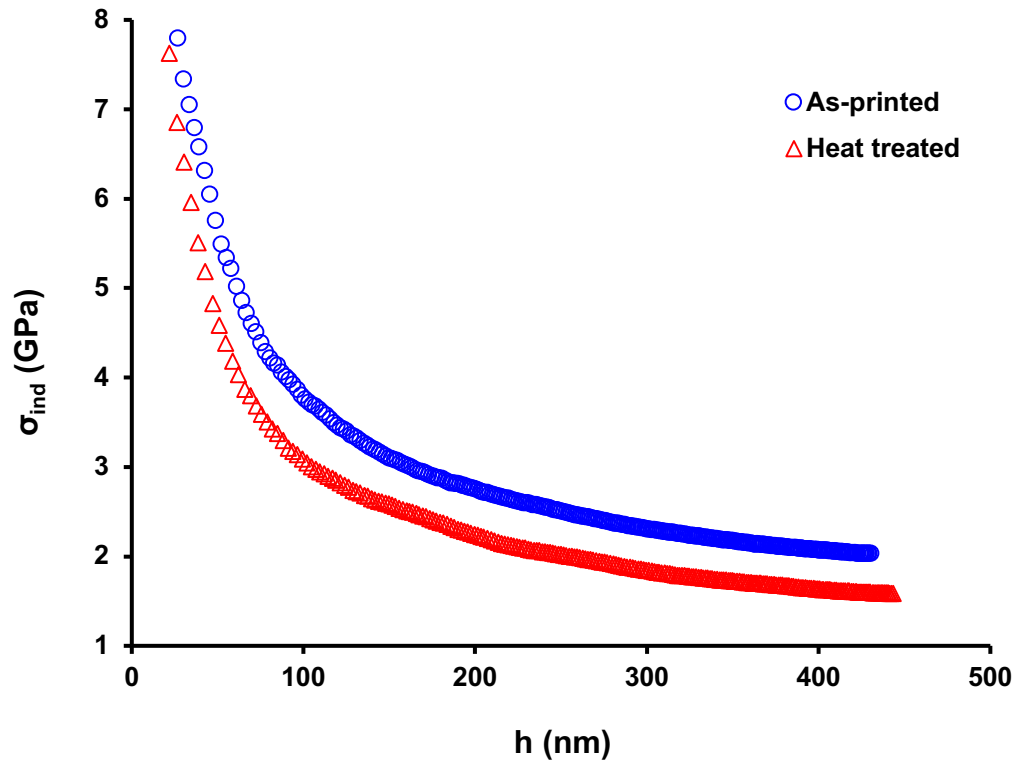


**Figure 54 Indentation size effect in the as-printed and heat treated samples [1]**

As observed in Fig 4.16, indentation stress is dependent upon depth where it increases with the decrease in the indentation depth. The shallow-depth indentation results in higher hardness as compared with large-depth ones, where it is attributed to dislocation starvation and strain gradient plasticity [12, 13].

When indenter tip is at few nanometer depths in contact with surface of the material, the material can be considered dislocation free “dislocation starved” where the strength of the material can be as big as the theoretical strength (see Fig. 4.17). As the indenter further drives within the material, an extra storage of dislocations “geometrically necessary dislocations” (GNDs) is introduced in the material in order to provide the necessary lattice rotation to accommodate the shape of the indenter, see Figs. 4.17 and 4.18 [12, 13]. As the indentation is shallow, the plastic deformation is to be happen over a very small volume of martial containing a limited number of



easy slip systems. Therefore, the GNDs may have different mobility and Burger's vector as compared with ordinary dislocations [1]. The density of GNDs is inversely related with indentation depth where at shallow depths larger number of GNDs is expected which results in the increasing strength near the surface of the sample.

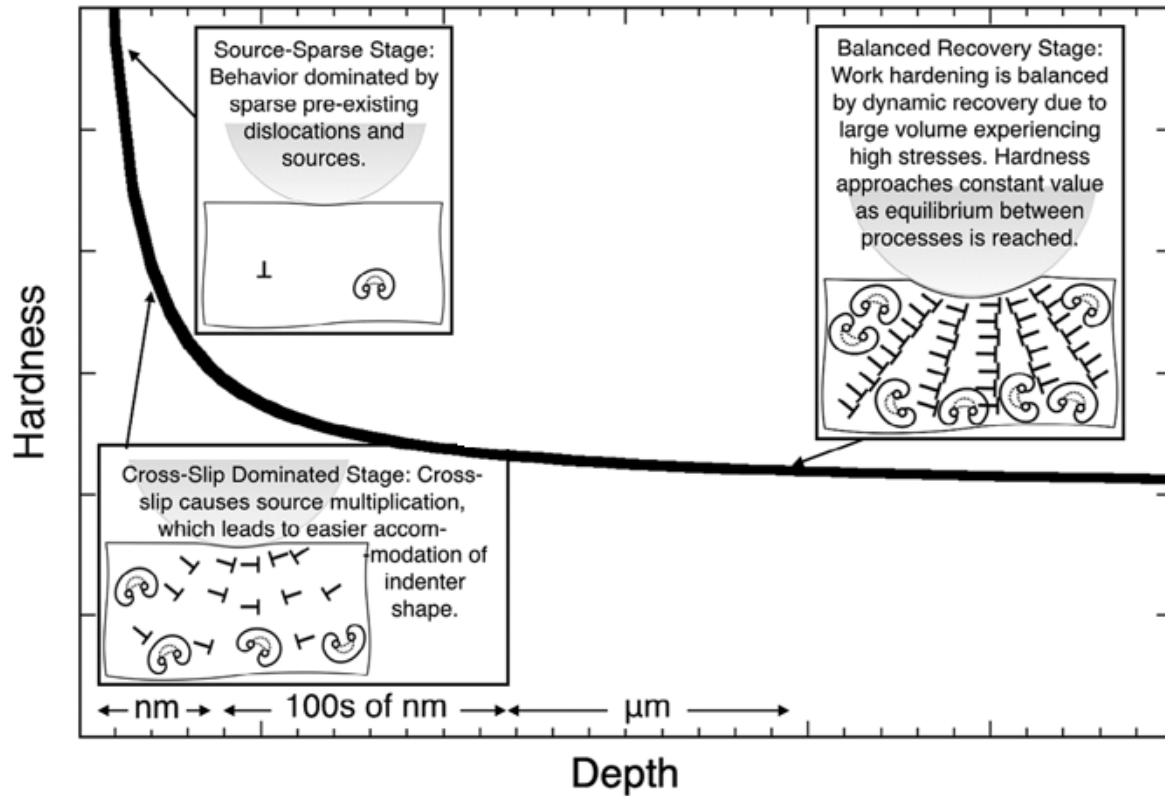
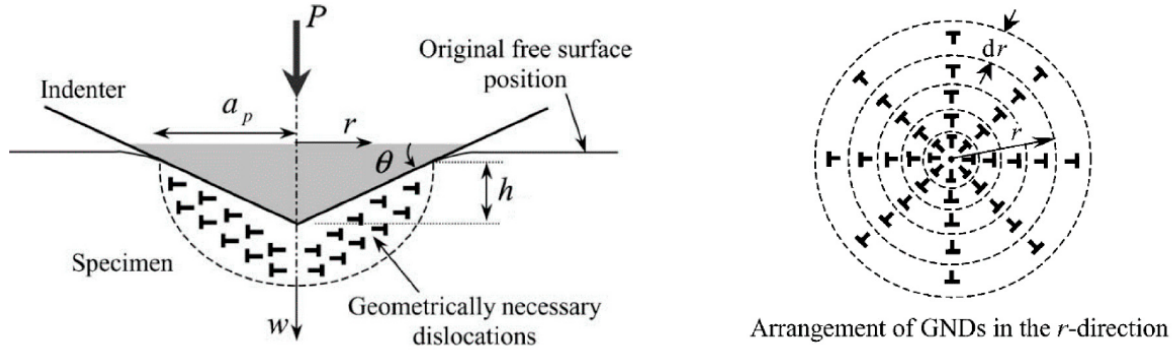


Figure 55 The ISE and the corresponding changes in the dislocation contributions [14].



**Figure 56 Schematic of geometrically dislocations (GNDs) created during the indentation process. The dislocation structure is idealized as circular dislocation loops [11].**

The density of GNDs [12, 13]:

$$\rho_{GNDs} = \frac{3}{2bh} \tan^2 \theta \quad (4.2)$$

where  $\theta$  is effective semi-angle of the conical indenter =  $70.32^\circ$ ,  $b$  is Burgers vector:  $2.86 \times 10^{-10}$  m, and  $h$  is the contact depth.

As observed in Fig. 4.19, the density of GNDs increases with decreasing in the indentation depth which is directly attributed to the strain gradient near the surface. The ISE is more noticeable in the as-built sample because of less strength in the heat-treated material. Studies on the assessment of the dependence of the geometrically necessary dislocation upon depth and strain rate on the polycrystalline fcc metals/alloys have suggested that GNDs density displayed the characteristic decrease with increasing  $h$ . Apparently, for the small indentation depths, GNDs are main contributing dislocations in order to accommodate for the lattice rotation imposed by indenter geometry. GNDs are, therefore, dependent upon  $h$  and the indenter geometry. However, for large indentation depths (macroscopic regime), statistically stored dislocations (SSD) are responsible for plastic deformation. The SSDs which are a function of plastic strain in the material are independent of  $h$ .

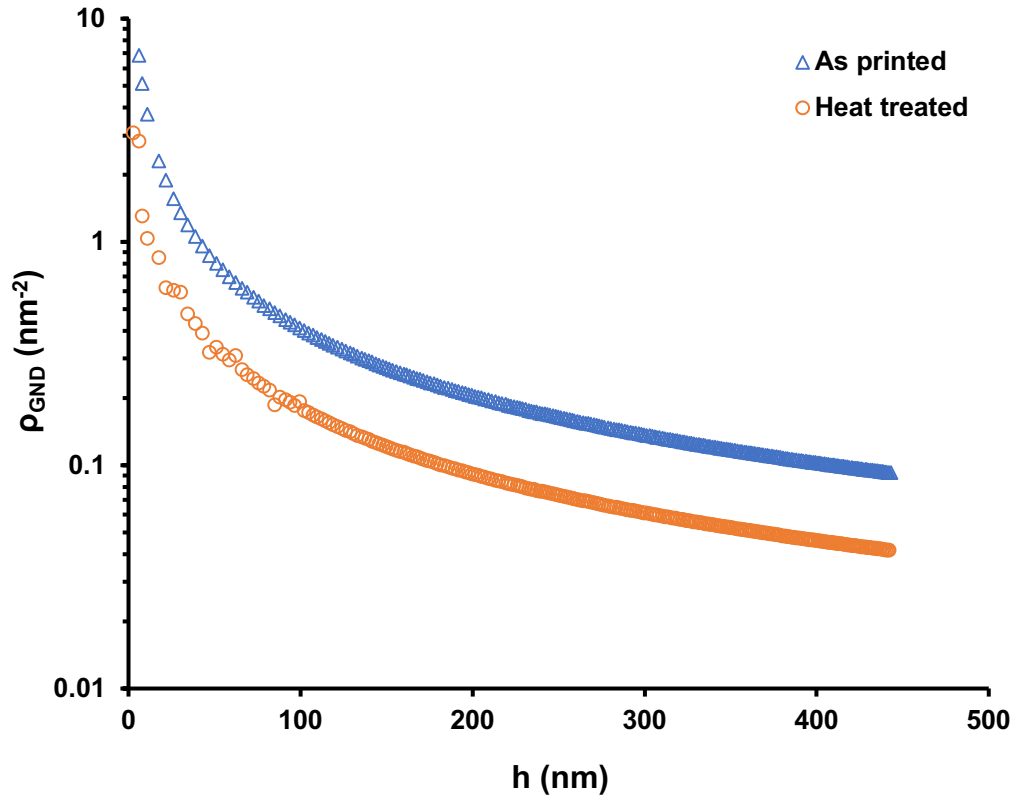


Figure 57 Density of GNDs versus depth in the as-printed material [1].

#### 4.4 References

- [1] Alghamdi, F. & Haghshenas, M. SN Appl. Sci. (2019) 1: 255.  
<https://doi.org/10.1007/s42452-019-0270-5>
- [2] Aboulkhair, Nesma T. Additive manufacture of an aluminum alloy: processing, microstructure, and mechanical properties. Nottingham, UK: University of Nottingham, 2015.
- [3] Li W, Li S, Li J, Zhang A, Zhou Y, We Q, Yan C, Shi Y (2016) Effect of heat treatment on AlSi10Mg alloy fabricated by selective laser melting: microstructure evolution, mechanical properties and fracture mechanism. Mater Sci Eng A 663:116–125
- [4] E Ogris (2002) Institute of Metallurgy, ETH Zürich Ph.D. Thesis
- [5] Wang RY, Lu WH, Metall S (2013) Spheroidization of eutectic silicon in direct-electrolytic Al-Si Alloy. Mater Trans A 44:2799–2809
- [6] Ogris E, Wahlen A, L uchinger H, Uggowitz P (2002) On the silicon spheroidization in Al-Si alloys. J Light 2:263–269
- [7] Keeffe ME, Umbach CC, Blakely JM (1994) Surface self-diffusion on Si from the evolution of periodic atomic step arrays. J Phys Chem Solids 55:965–973
- [8] Jordović B, Nedeljković B, Mitrović N, Živanić J, Maričić A (2014) Effect of heat treatment on structural changes in metastable AlSi10Mg alloy. J Min Metall Sect B Metall 50(2):133–137
- [9] Aboulkhair NT, Stephens A, Maskery I, Tuck C, Ashcroft I, Everitt NM (2015) Mechanical properties of selective laser melted AlSi10Mg: nano, micro, and macro properties. In: Solid freeform fabrication symposium 2015. Austin, Texas, pp 1026–1036 20.
- [10] Everitt NM, Aboulkhair NT, Maskery I, Tuck C, Ashcroft I (2016) Nanoindentation shows uniform local mechanical properties across melt pools and layers produced by selective laser melting of AlSi10Mg alloy.
- [11] Xianglong Yu, Wang L (2018) T6 heat-treated AlSi10Mg alloys additive-manufactured by selective laser melting. Procedia Manuf 15:1701–1707

- [12] Voyiadjis GZ, Yaghoobi M (2017) Review of nanoindentation size effect: experiments and atomistic simulation. *Crystals* 7(32):1. <https://doi.org/10.3390/cryst7100321>
- [13] Nix WD, Gao H (1998) Indentation size effects in crystalline materials: a law for strain gradient plasticity. *J Mech Phys Solids* 46:411–425.
- [14] Michael R. Maughan, Ariel A. Leonard, Douglas D. Stauffer & David F. Bahr (2017) The effects of intrinsic properties and defect structures on the indentation size effect in metals, *Philosophical Magazine*, 97:22, 1902-1920, DOI: 10.1080/14786435.2017.1322725

## 5. Conclusion

This study considered the various aspects of heat treatment cycles on selective laser melting of an aluminum-silicon alloy, AlSi10Mg. This project tried to uncover the variations in mechanical properties and then correlate them to the microstructural evolution in the as-printed and heat-treated alloys. Through Vickers and nanoindentation techniques, micromechanical responses of an additive manufactured AlSi10Mg in the as-built, heat treated “artificially aged”, WQ, AC and FC conditions were elaborated, along with microstructural assessments (OM and SEM) to provide evidence to establish microstructure/micromechanical correlations.

The findings in this investigation conclude the following

- The cellular-dendritic solidification resulted in the fine equiaxed grains at the melt pool core whereas elongated grains at the boundary with continuous segregations Si fiber.
- Upon heat treatment cycle of 1-h solution heat treatment at 520 °C, enough time and temperature are provided for the interconnected Si fibers to be transformed to the Si particles (spheroids).
- The artificial ageing at 170 °C for 4 h promotes the Si spheroidization which results in the softening of the alloy.
- After heat treatment, variation in nano-hardness was observed due to the presence of Si particles.
- The heat treatment resulted in softening the alloy. The hardness of the as-built sample was higher than the various heat-treated samples.
- The FC showed to the softest and the as-built showed the hardest conditions.
- The as-built material exhibited uniform nano-hardness due to the fine microstructure.

- The average hardness values are:
  - As-built sample:  $1.90 \pm 0.11$  GPa,
  - Artificially aged:  $1.55 \pm 0.05$  GPa,
  - WQ:  $1.13 \pm 0.04$  GPa,
  - AC:  $0.92 \pm 0.04$  GPa
  - FC:  $0.78 \pm 0.02$  GPa.
- Heat Treatment dissolved the formation of anisotropy in the microstructure caused by the layering process improve the ductility.
- Indentation size effect, increase in hardness with the decrease in the depth, is observed in both as-built and heat-treated materials.

## 6. Future Work

The following are recommended to develop the relationships between mechanical properties and microstructural features:

- Fabricate AlSi10Mg alloy with different tailored parameters, spend scan, scan strategy, hatching spacing, layers' thickness and laser power, to assess the effect of print parameters on the mechanical properties and microstructural evolution.
- Tailor the heat treatment cycle, e.g. by changing solutionization and/or ageing time and study the effects of different profiles on the microstructure and mechanical response of the AlSi10Mg and determine the tool which provides optimum result.
- Utilize the electron back-scattering diffraction (EBSD) to further assess the grain size and morphology of various AlSi10Mg alloy conditions and evaluate the texture in the microstructure of this alloy.
- Utilize Transmission electron microscopy (TEM) to study and investigate the correlation of mechanical properties and how it affects the strengthening mechanisms.